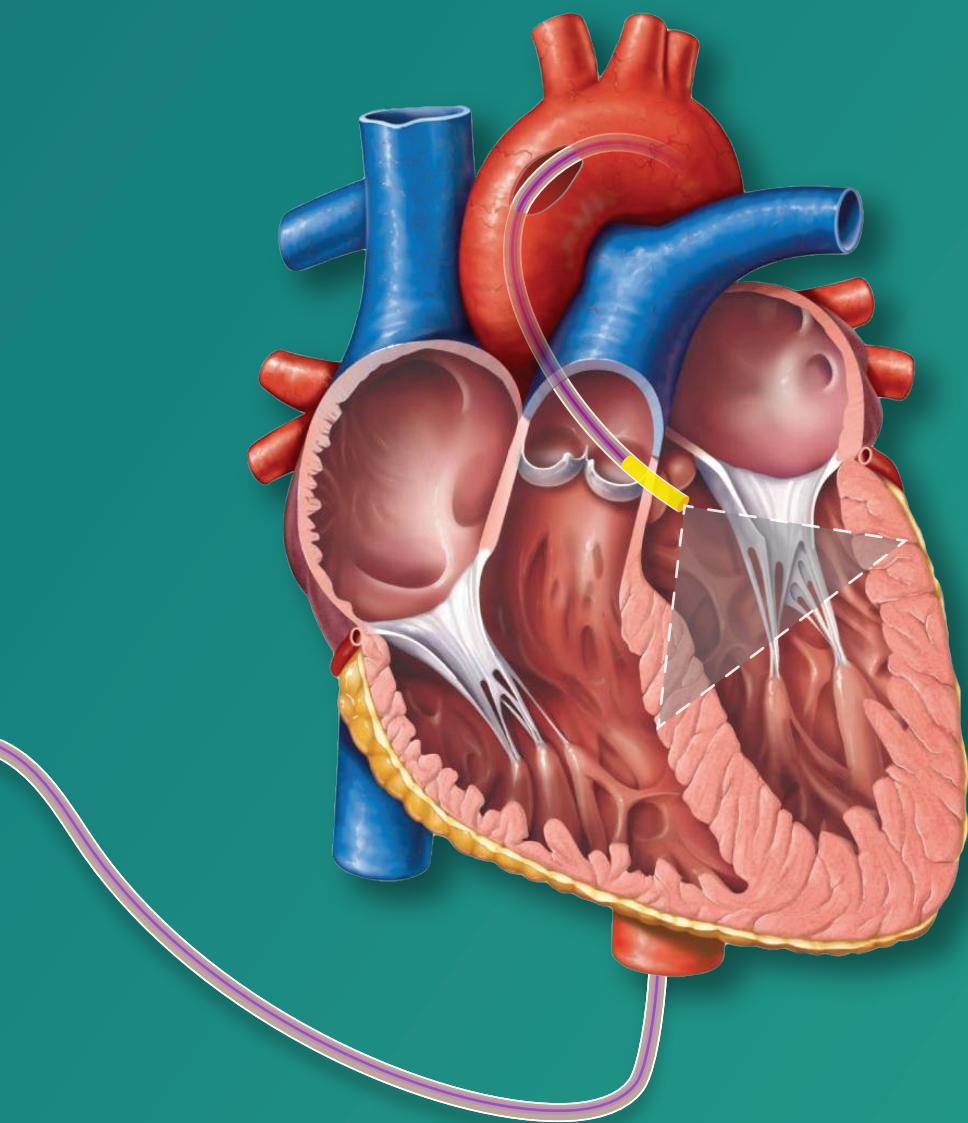


Agile and Bright Intracardiac Catheters



Martin Pekař

Agile and Bright Intracardiac Catheters

Flexibele en slimme hartkatheters

Martin Pekař

Typeset with L^AT_EX.
Font design by František Štorm.

Cover design by Martin Pekař.

Cover image courtesy:
www.clipart-library.com (frontside)
Patrick J. Lynch, medical illustrator (backside)
C. Carl Jaffe, MD, cardiologist (backside).

ISBN/EAN: 978-94-028-0720-2

Published by Ipskamp Drukkers.

A digital version of this thesis is available at
<http://repub.eur.nl/pub/>

Copyright © 2017 by Martin Pekař, Eindhoven, the Netherlands.

Agile and Bright Intracardiac Catheters

Flexibele en slimme hartkatheters

Proefschrift

ter verkrijging van de graad van doctor aan de
Erasmus Universiteit Rotterdam
op gezag van de rector magnificus

Prof.dr. H.A.P. Pols

en volgens het besluit van het College voor Promoties.

De openbare verdediging zal plaatsvinden op
woensdag 13 september 2017 om 9:30 uur

door

Martin Pekař

geboren te Praag, Tsjechië.

Promotiecommissie

Promotor: Prof.dr.ir. A. F. W. van der Steen

Overige leden: Prof.dr.ir. N. de Jong
Dr. T. Szili-Török
Prof.dr. F. L. Degertekin

Copromotoren: Dr. G. van Soest
Dr. M. B. van der Mark

Work presented in this thesis was carried out at Philips Research in Eindhoven, the Netherlands. Academic co-operation with Erasmus Medical Center in Rotterdam, the Netherlands is acknowledged.

This research received financial support from the Marie Curie Actions FP7 project „OILTEBIA“ (grant no. 317526) of the European Union and from the Philips Research.

Financial support by the Erasmus Medical Center and Dutch Heart Foundation for the publication of this thesis is gratefully acknowledged.

Preface

On 20th March in 1987, I saw the world around me, then exploring new entities became my passion ever since. I enjoy to explore new countries, people, and technologies. The first documented proof of this personal quality dates back to 1988. Yet in that time, and perhaps unknowingly inspired by the novel ideas of Albert Einstein, I tried to use glue as a microphone as shown in the photograph below. Quarter a century later, I exchanged the "microphone" with little underwater drums that can transmit and receive (ultra)sound and therefore provide a mean to play music, which can see the heart from inside through the blood. When dealing with a cumbersome signal power transmission, that large speed of light constant from Einstein's law came handy. Soon, an optical fiber link connected to an ultrasound transducer was born. The thesis that you now hold in your hands is about nothing else than the little ultrasound drums and an optical fiber-link connection.



Author of this thesis at the age of one year.

Contents

Chapter 1: Introduction	1
<u>Part I: Ultrasound Frequency Tuning</u>	
Chapter 2: Semi-analytic model of CMUT operated in collapse mode	13
Chapter 3: Frequency Tuning of Collapse-Mode CMUT	31
Chapter 4: Imaging Performance of Frequency-Tunable CMUT Array	49
Chapter 5: Preclinical Testing of Frequency-Tunable CMUT Probes	65
<u>Part II: Wiring Electronics with Light</u>	
Chapter 6: All-Optical Fiber Link for Catheters	77
Chapter 7: Electrifying Catheters with Light	93
Chapter 8: Overview and Conclusions	111
References	119
Summary	127
Nederlandse Samenvatting	129
Publications	133
Acknowledgements – Dankwoord – Poděkování	135
Curriculum Vitae	139
PhD Portfolio	141

Introduction

1.1 Motivation

Cardiovascular disease is the leading global cause of death, accounting for more than 17.3 million deaths per year, which is expected to grow to more than 23.6 million by 2030. Heart-related problems accounted for 31 % of all global deaths in the past few years, claiming more lives than all forms of cancer together. The costs of cardiovascular diseases including expenditures and lost productivity total more than \$316.6 billion¹. The general goal of this thesis is to develop new devices and techniques that would help the clinician in diagnosis and treatment of cardiovascular diseases.

1.2 Cardiac rhythm disorders

Advancing age, high blood pressure, obesity or heavy alcohol consumption can result in chemical or hormonal imbalances within the heart muscles. These changes often cause arrhythmia – a heart rhythm disorder, during which the heart beats too slowly, too fast, or irregularly². While the heart rate can be brought to normal by medications, the irregular beating pattern is more difficult to treat². It hampers blood pumping effectiveness of the heart, which may cause the lungs, brain and all other organs to be damaged or shut down. An irregular beating pattern promotes spots of stagnating blood which are prone to blood thrombus formation. In arrhythmia patients, the tortuous anatomy of the left atrial appendage (LAA) is at the highest risk to source a thrombus, which can then be pumped out to the brain causing a stroke^{3,4}. Anti-clotting medications are therefore typically prescribed to dilute the blood and prevent thrombus formation⁵. While these medications reduce the risk of stroke, they increase rates of major bleeding⁶.

Arrhythmias can develop in any part of the heart and can propagate by two different mechanisms². The first one is called re-entry circular propagation of the electric impulse around a particular barrier in the heart muscle. The second one is called focal arrhythmia, in which case the pathological electric impulse is generated at a particular point and spreads to other parts of the myocardium. Atrial fibrillation (AF) is one of the most common arrhythmias, affecting an estimate of 2.7 million to 6.1 million adults in the United States⁷.

Patients, who resist the medication-based treatment or are at a high bleeding risk, are referred to an electrophysiology intervention. Using electrodes inserted in the heart, the electric pathways are first mapped to identify the origins of arrhythmias. Next, a radiofrequency or cryo ablation are performed to isolate the sources or pathological stimuli as illustrated in Figs. 1.1(a) and 1.1(b), respectively⁷. If the LAA is too deep or exhibits high tortuosity, electrophysiologist may decide to close it to prevent any blood stagnation. This can be done either surgically or by using an occluding or a suture device⁸.

Both the ablation and LAA closure can be carried out in an open heart setting or percutaneously via blood vessels. The latter approach supports less damage to the patient and faster recovery times. It requires, however, a supporting imaging device for in-heart navigation, instrument positioning, and

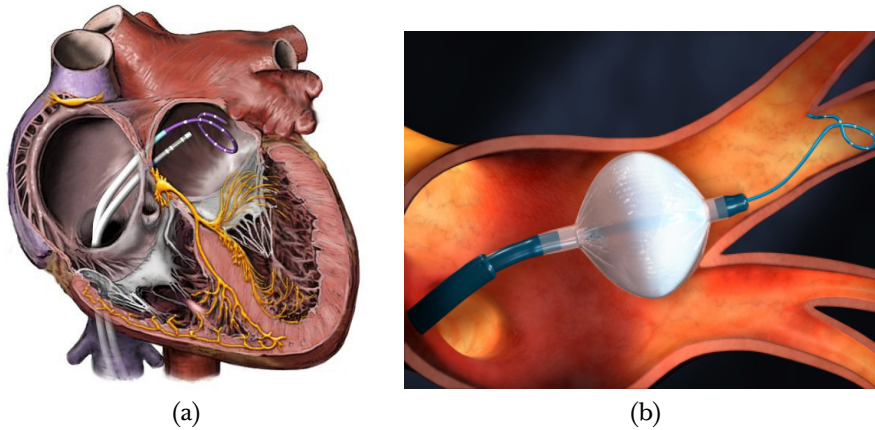


Figure 1.1: An illustration of two different ablation methods. Radiofrequency ablation (a) using an ablation catheter (white) and a mapping catheter (purple) to monitor for electric pathways. Cryo ablation (b) achieved by filling an elastic balloon with an extremely cold substance. Image (a) and (b) have been reproduced from www.blaufuss.org and www.heartrhythmdoc.com, respectively.

for early diagnosis and monitoring of complications, e.g. damage to cardiac structures, thrombus formation, esophageal injury, or pericardial effusion⁹.

1.3 Structural heart diseases

The other category of heart disorders is called structural heart diseases (SHD)¹⁰. Some of the SHD are congenital, while others develop because of another condition – such as high blood pressure, obesity, alcoholism, or an infection. As an untreated heart disease advances, the heart becomes progressively weaker, often resulting in a sudden cardiac arrest.

Examples of a SHD are atrial septal defect (ASD) and patent foramen ovale (PFO). Although both are basically holes in the wall of the atrial septum, their causes are different. An ASD originates in a failure of the septal tissue to form between the atria, a defect that a fetus is born with. A PFO, on the other hand, can only occur after birth when the foramen ovale (a shunt between atria to bypass the fetal lungs) fails to close after a newborn starts breathing. In Europe, about 7 per 1000 children are born with a structural heart problem that arises from abnormal formation of the heart during its prenatal development¹¹. Common malformations include a persisting hole in the septum of the heart or a defective heart valve, some of which may require a surgical correction. These can be, similarly to the aforementioned alternatives in electrophysiology, treated surgically or percutaneously. Although the latter one is the preferred option, it requires a real-time imaging device to monitor patient anatomy, location of intracardiac instruments, and surveillance of intraprocedural complications¹².

Number of other heart diseases can arise from heart infections and inflammations caused by bacteria viruses¹³. These parasites can attack heart valves, inner lining of the heart, myocardium or cause inflammation of the membrane surrounding the heart. Proper diagnosis of such diseases demands a high resolution close-up imaging of the attacked cardiac structure¹⁴.

1.4 Minimally invasive procedures

Traditionally, heart diseases have been treated in an open heart surgery, where the chest is cut open and surgery is performed on the muscles, valves, or arteries of the heart, as illustrated schematically in Fig. 1.2(a). Advances of medical technology, however, enabled minimally invasive procedures to be performed on the heart. These procedures are carried out by entering the body through the skin or a natural body cavity or anatomical opening with the smallest damage possible to these structures. Cardiology is the first medical specialty to apply minimally invasive technology on a large scale (intracoronary thrombolysis, later balloon angioplasty and stenting). The minimally-invasive instruments used in cardiology are long, thin, flexible tubes called catheters that are threaded into the heart through a blood vessel as illustrated in Fig. 1.2(b). These catheters allow injecting fluoroscopic contrast media, which is used mainly in the diagnosis and evaluation of congenital diseases, coronary artery lesions and to evaluate systolic and diastolic cardiac function. In recent years, intracardiac catheters have been equipped with integrated sensors for anatomical and functional assessment of the heart such as blood pressure and flow measurement or ultrasound intracardiac echocardiography (ICE) imaging. The latter one utilizes ultrasound as a visual substitute capable of seeing through blood, viewing anatomic and physiologic characteristics, monitoring remote events and navigating other devices, such as ablation catheters, balloons and heart valves during complex diagnostic or therapeutic interventions.

1.5 Brief history of intracardiac echocardiography catheters

It may sound anciently remote to find out that the potential of imaging heart structures with catheter-based devices dates back to 1960¹⁵, when the movement of the heart chambers was observed intracardially *in vivo* using ultrasound in dogs. The initial prototypes used a single-element transducer, which was rotated to achieve cardiac imaging¹⁶. In 1972, the first multi-element circular phased-array ICE catheter was developed by Bom et al. in Rotterdam¹⁷. Two decades later, a dedicated side-looking phased-array device for ICE imaging was introduced and tested *in vivo* in dogs¹⁸. The first commercial ICE (AcuNav ultrasound catheter, Siemens, Mountain View, CA, USA) was introduced in 1999¹⁹.

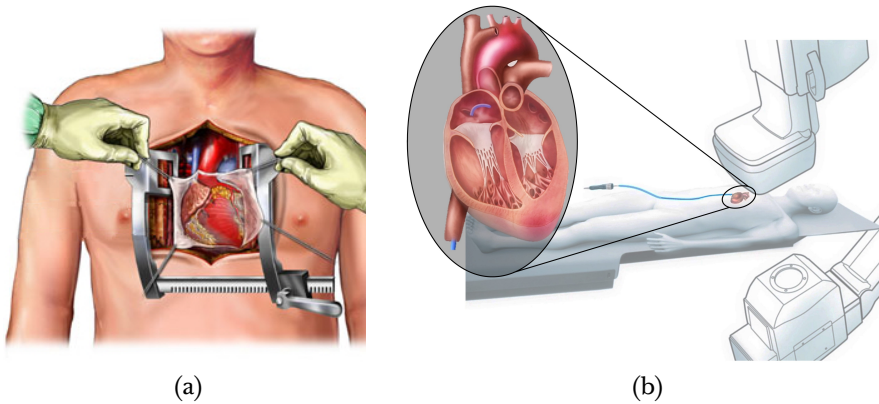


Figure 1.2: A schematic drawing of a traditional open heart surgery (a) and a modern catheter-based minimally invasive procedure (b). Image (a) has been reproduced from www.medgurus.org, image (b) is a courtesy of Philips Research.

1.6 Present intracardiac echocardiography imaging

Nowadays, ICE is an essential non-fluoroscopic imaging modality used during treatment of structural heart diseases (SHD), in particular closures of complex patent foramen ovale and atrial septal defects²⁰. These procedures utilize ICE to confirm adequate guidewire position, assist with balloon sizing, sheath placement, device release and disconnection. Compared with transoesophageal echocardiography (TEE), ICE exhibits the same global hospital and physician costs, but is associated with much less procedural stress to the patient, shorter procedural and fluoroscopic times¹². A state-of-the-art ICE image acquired with the commercially available AcuNav ICE catheter is shown in Fig. 1.3.

The most important advantage of ICE is, however, its compatibility with monitored anaesthesia care or local anaesthesia which motivates the supplementary or investigational use of ICE for other SHD interventions. ICE is currently being explored for guiding transcatheter aortic valve implantations (TAVI)²², it is used to assist with guidewire passage through the native valve, positioning of the valve-carrying catheter system, monitoring of prosthetic valve deployment and verification of its adequate function. The advantage of ICE for TAVI as compared to the conventional fluoroscopy guidance lies in monitoring with low doses of contrast agent, which is desired for preserving renal and kidney function.

ICE has been demonstrated to facilitate closure of a patent ductus arteriosus¹². During this procedure, the ICE catheter is positioned inside the ascending aorta and used to monitor vessel anatomy and aortic dissections.

Although the ICE catheter can be placed very close to the aortic valve, its imaging capability for diagnosis of stenosis or infective endocarditis is difficult due to the side-looking catheter design and the low imaging frequency (typically 7 MHz).

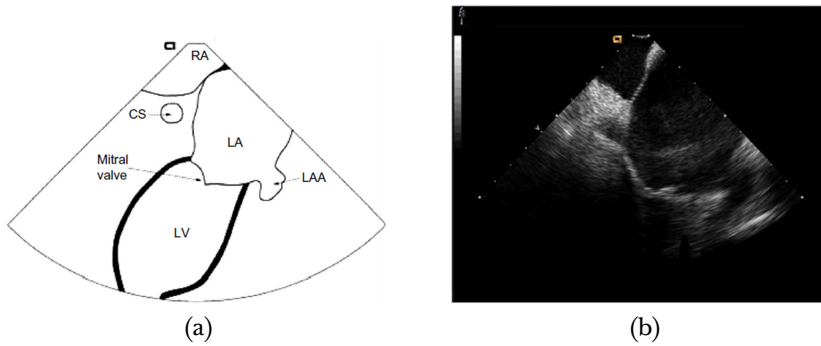


Figure 1.3: A schematic view of cardiac chambers from intracardiac echocardiography catheter placed in right atrium (a) and a real-time acquisition by intracardiac echocardiography (b). RA indicates right atrium; CS, coronary sinus; LA, left atrium; LAA, left atrial appendage; LV, left ventricle. Both (a) and (b) images are reproduced from an earlier publication²¹.

In electrophysiology, ICE is used to guide transeptal puncture, to provide real-time navigation, catheter placement and surveillance of intraprocedural complications, e.g. pericardial effusion or thrombus formation²³. Although ICE has been investigated for guiding closure of the LAA to prevent a thrombus formation, it does not have the needed performance to visualize the complex anatomy of the LAA when imaging from the right heart due to the low resolution in the far field of view as can be seen in Fig. 1.3(b)²¹. A high frequency ICE catheter that would be steerable to the close proximity of LAA via a transeptal puncture is desired²⁴.

1.7 New transducer technology for intracardiac echocardiography imaging

The clinical review reports^{12,14,20,21,24,25} demonstrate that the unmet need of having the possibility of high penetration or close-up high resolution imaging in a single device could be answered by a frequency-tunable ultrasound imaging. The need of obtaining new intracardiac views, that are not possible to achieve with a side-looking ICE design, could be addressed by integrating the frequency-tunable transducer into a steerable forward-looking catheter sheath^{12,24,25}. There is, however, no such device commercially available to cardiologists. Its absence is related to its design and manufacturing difficulties, and physical limitations of the established and commercially only adapted piezoelectric transducer technology²⁶⁻²⁸. Although the behaviour and fabrication of piezoelectric transducers are well understood, it has proven to be challenging and costly to built and integrate this transducer technology into a forward-looking intracardiac catheters²⁷.

In the past two decades a new transducer technology based on capacitive mi-

cromachined ultrasonic transducer (CMUT) has evolved²⁷, which is expected to advance the ICE imaging²⁵. The CMUT technology is complementary to conventional piezoelectric transducers offering several performance and fabrication advantages. Distinct to a piezoelectric transducer, which vibrates in its thickness mode to generate ultrasound, a CMUT consists of many tiny capacitors (typically tens to hundreds of micrometres in diameter) with movable top plates (commonly referred to as „membrane“) connected electrically in parallel. The CMUT generates ultrasound as a result of these membrane vibrations in response to an electric actuation. These membranes are a few micrometres thin and have an acoustic impedance close to that of water (1.5 MRayl). They hence offer inherent wideband operation and eliminate the challenge of manufacturing thin quarter-wavelength matching layers²⁹. The frequency of operation for a CMUT is determined by the capacitor dimensions, mechanical properties of the vibrating membrane and the static DC (bias) voltage used to pre-bend the vibrating plate. In a so-called collapse-mode operation of CMUT, the membrane is biased at a voltage high enough to collapse the center area of the membrane onto the bottom of the cavity (collapse voltage) as shown in Fig. 1.4. Then AC voltage is applied to excite the free part of the membrane without releasing the center of the membrane from the bottom of the cavity. In the collapse mode, the resonance frequency increases for a high magnitude of the polarity independent bias voltage, because the membrane stiffness and the contact radius of the collapsed portion of the membrane increases with larger deflection.

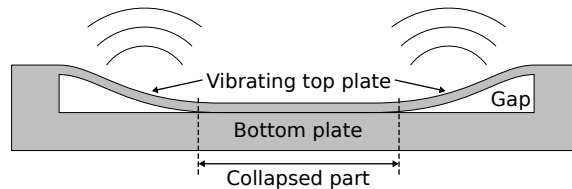


Figure 1.4: Schematic drawing of a CMUT operated in collapse mode.

In addition to the frequency tunability, CMUTs take advantage of silicon integrated circuit fabrication techniques, which makes it possible to fabricate CMUTs of arbitrary geometry and size in a batch manufacturing process, reducing the costs and offering seamless monolithic integration with front-end electronics making it a competitive option for intracardiac echocardiography imaging and for other ultrasound modalities^{30,31}. The first commercial application is a relatively conventional array probe³².

The primary objective of this thesis is to investigate the usability of CMUT for frequency-tunable forward-looking intracardiac imaging. To this aim, a CMUT device operated in the collapse mode has been modelled, characterized and tested in a phantom study. A rigid imaging probe prototype has been built and tested *ex vivo*. Ultimately, frequency-tunable, forward-looking, intracardiac imaging with a deflectable ICE catheter has been demonstrated *in vivo* in an animal model.

1.8 Wiring electronics with light

Even though the connection of the transducer to front-end electronics can be solved by the monolithic integration, designers of ICE imaging catheters face a challenge of interconnecting the proximal front-end electronics with a distal ultrasound system. Present intracardiac ultrasound evolves towards multi-dimensional high frame-rate imaging. 3-D ultrasound imaging proves to be more intuitive as compared to 2-D, decreasing the learning curve and simplifying interpretation of the ultrasound images^{33–35}. High frame-rate imaging allows capturing the fast dynamics of moving anatomies (e.g. heart valves³⁶) and allows extracting additional information about the tissue mechanical properties (e.g. elastography³⁷) and its response to electrical stimulation (electromechanical wave imaging³⁸). Both trends will help improving the patient outcome but at the same time they challenge the design of signal transmission over the long and narrow ICE probes due to the enormous increase in the data rates and the number of signal channels. These challenges directly limit the achievable frame-rate, which is the key parameter for imaging the fast dynamics of the heart.

The maximum data rate for an ultrasound imaging system can be calculated as

$$\Phi = N \cdot n_{\text{bits}} \cdot n_{\text{samples}} \cdot f, \quad (1.1)$$

where N is the number of signal channels, n_{bits} is the number of bits in analog-to-digital (A/D) conversion, n_{samples} is the number of samples per acoustic wavelength, and f is the acoustic frequency.

Considering a 256-channel 10-MHz ultrasound imaging system equipped with a 16-bit A/D convertor and a minimum of 4 samples per wave, data rate up to 164 Gbit s⁻¹ can be attained. The best experimental electrical transmission results so far have demonstrated 14 Gbit s⁻¹ over a 85-cm long flexible interconnect³⁹, which is close to the typical length of an ICE catheter. The narrow diameter of the ICE device, however, requires further scaling and compromises on shielding of the electrical interconnects, resulting in a lower data rate, thus frame-rate.

On the other hand, data rate of a few micrometers large vertical-cavity surface-emitting lasers, conventionally used for Ethernet communication⁴⁰ P. 319, starts at 10 Gbit s⁻¹. Photonic integrated circuits have demonstrated data rates up to 1.6 Tbit s⁻¹ in a recent telecom system (Infinera, Sunnyvale, CA, USA), where 40 wavelengths each operating at 40 Gbit s⁻¹ were integrated onto a single chip⁴¹. Optical interconnects show great promise at high data speeds because of the loss, which is about six orders of magnitude lower as compared to conventional electrical wires⁴¹. As the data rates continue to rise, it is probable that optical links will ultimately take over the conventional copper wires traditionally used in catheters.

The calculated data rate of 164 Gbit s⁻¹ would allow plane-wave imaging up to 10 cm at a frame-rate of 7.7 kHz. For cardiac imaging, very high frame-rate up to 4 kHz is typically needed to visualize shear-waves and accurately measure

their propagation velocity³⁶. Replacing the electrical wires with an optical data link, would therefore enable very high frame-rate imaging and would still allow for frame-averaging to increase the signal-to-noise ratio, which is essential for high penetration depth of the plane-wave imaging⁴².

In addition to the increased data rates, glass or plastic optical fibers show low magnetic susceptibility and are immune to radiofrequency (RF) interference, which is being picked-up mainly by the long metallic components⁴³. Fiber optics have been therefore proposed to replace metal wires inside a position-tracking system to achieve compatibility with a magnetic resonance imaging⁴⁴.

The secondary objective of this thesis is to explore and demonstrate the potential of fiber-optics for optical signal and power transmission in catheters. A simple all-optical pressure-sensing catheter has been built to demonstrate this concept. Next, a functional bench-top catheter demonstrator has been constructed to show all-optical signal and power transfer for synthetic aperture ultrasound imaging.

1.9 Thesis outline

The ultimate objective of this thesis is to develop new ultrasound and optical components and techniques for minimally invasive intracardiac echocardiography to characterize tissue and to improve the feedback to the physician.

Within the scope of this challenging task, **Chapter 2** introduces the CMUT, a state-of-the-art transducer technology. In this chapter it is described how a semi-analytical model of a fluid-loaded CMUT array operated in collapse mode is developed and experimentally validated to understand the underlying principles of this new transducer technology.

A new imaging concept utilizing a frequency-tunable ultrasound transducer is introduced in **Chapter 3**. The feasibility of frequency tuning of a fabricated CMUT operated in collapse-mode is demonstrated experimentally in a preliminary phantom study.

The hardware integration has been advanced and a 1-D CMUT array has been integrated in a rigid probe prototype. 2-D imaging performance of the developed probe at a frequency-tunable range has been quantified on a phantom in **Chapter 4** and demonstrated *ex vivo* on a passive beating heart platform in **Chapter 5**.

The ultrasound probe prototype was further miniaturized into a deflectable forward-looking ICE catheter prototype having a diameter of 4 mm. In **Chapter 5**, the frequency tunability is investigated in a porcine animal model for forward-looking ICE imaging, addressing the requirement of having the possibility of high penetration (zoom-out) or high resolution (zoom-in).

For a preclinical testing, the diameter of the catheter prototype needs to be further reduced to a maximum of 3 mm. Catheter miniaturization was however limited by the interconnects and the number of signal and power transmission wires, which connect the CMUT (integrated in the catheter tip) with the outside

world. Adjacent research has been therefore carried out in the second part of this thesis to find out a new way of transmitting signals and power in a catheter.

A novel idea of utilizing a light-emitting diode for both the signal and power transmission in catheters has been proposed in **Chapter 6**. A simple, pressure-sensing catheter prototype has been constructed to demonstrate this new concept. The built catheter features only a single optical fiber for both optical signal transmission and optical power delivery to the sensor electronics integrated in the catheter tip. This novel all-optical interconnect solution has been proposed for ultrasound imaging catheters to increase the level of integration, to enable magnetic resonance compatible and radiofrequency interference-free imaging, and to eventually lower the costs of these limited-use devices.

A bench-top catheter demonstrator presented in **Chapter 7** has been built to demonstrate the performance of the all-optical signal and power transmission for ultrasound imaging.

The final section, **Chapter 8**, examines the developed frequency-tunability and zoom-in / zoom-out imaging technique and prospects of the all-optical interconnect solution for intracardiac catheters. The chapter completes with an overview of conclusions drawn from the research results published in the individual chapters of this thesis.

Part I

Ultrasound Frequency Tuning

Semi-analytic model of CMUT operated in collapse mode

This chapter has been submitted for publication as:

Martin Pekař, Stephan H. M. van Nispen, Rob H. B. Fey, Sergei Shulepov, Nenad Mihajlović, and Henk Nijmeijer, A Fluid-Coupled Transmitting CMUT Operated in Collapse Mode: Semi-Analytic Modelling and Experiments, *Sensors and Actuators A: Physical*.

Abstract

An electro-mechanical, semi-analytic, reduced-order (RO) model of a fluid-loaded transmitting capacitive-micromachined ultrasound transducer (CMUT) operated in collapse mode is developed. Simulation of static deflections, approximated by a linear combination of six mode shapes, are benchmarked towards state-of-the-art models and validated with digital holography microscope measurements of a fabricated CMUT device. The dynamic response of a detached single CMUT cell and an array of CMUT cells is predicted and analyzed for the effect of mutual radiation. The step-wise validation shows that our model predicts the static response including hysteresis behaviour of a collapse-mode CMUT with a high accuracy. The dynamic response and frequency-tunability are modelled with a satisfactory accuracy. The developed RO model is computationally efficient and in general faster than finite element methods. It is concluded that the presented RO model allows fast parameter analysis and is a powerful tool for CMUT pre-design.

2.1 Introduction

The development of capacitive micromachined ultrasonic transducers (CMUTs) has progressed significantly in the past years^{45–47}. Especially the collapse mode operation of CMUTs has shown a potential for high performance medical imaging⁴⁸. Accurate and fast simulation methods are necessary to guide the CMUT pre-design for a given application prior to the CMUT fabrication and to understand the device behaviour afterwards. Simulation and subsequent model validation of a collapse-mode CMUT encompass a multi-scale, multi-physics, nonlinear problem^{49,50}. A few hundred nanometer displacement of thousands of CMUT cells results in a pressure propagation up to tens of centimeters⁵¹. Nonlinearity of the electrostatic actuation force introduces amplitude distortion of the time-domain response, and pull-in (collapse) and pull-out (snap-back) events, all of which should be accurately captured by the model⁵².

The collapse-mode CMUT has been successfully modeled with a finite element method (FEM)^{53–55}. However, the multi-scale problem definition requires fine meshing and the nonlinearity results in pull-in and pull-out hysteresis loops, which challenge the FEM model convergence. This results in time consuming FEM simulations that can take up to 4 hours to calculate collapse voltage of a CMUT⁵⁶. They are therefore impractical for rapid collapse-mode CMUT prototyping.

State-of-the-art analytic models typically utilize a two-step approach for modelling collapse-mode CMUT behaviour. First, a static deflection profile is predicted for a given DC (bias) voltage. The dynamic behaviour is then studied using a equivalent circuit model⁵⁷. Analytic resolution of a circular plate equation has been done utilizing Timoshenko's uniform force solution to obtain the static deflection profile under the electro-static actuation⁵⁵. The advantage of this approach is that no simplifying assumption on the shape of the plate for the collapsed state has to be made. The disadvantages are suitability only for the circular CMUT plates and a low accuracy due to the uniformity approximation of the highly non-uniform electro-static actuation force. This uniform electro-static force assumption has been later removed by discretizing the CMUT plate and introducing a spatially-dependent electro-static model force⁵⁸. The resulting model was solved numerically under the assumption that the static displacement profile can be approximated by a 14-degree polynomial function. The dynamic behaviour of the top plate has been modeled using an equivalent circuit model. These lumped element models, however, introduce sporadic average displacements, negative capacitance or assumptions on loading effects of the fluid. Such simplifications hinder understanding of the underlying mechanics, e.g. the displacement of a single point on the CMUT top plate can not be modelled^{58,59}.

Recently, an electro-mechanical fast time-domain model of a rectangular CMUT has been developed⁶⁰. The model utilizes a numerical method to solve the dynamic plate equation. Although it has been developed for a CMUT operated in conventional mode, a simple penalty function has been introduced to

accommodate for snap-back behaviour. The static and dynamic mechanical displacement of the top plate has been compared to experimental measurements with a digital holographic microscope (DHM). The model is also capable of simulating the fluid loading by introducing self and mutual acoustic coupling between the CMUT cells, which was validated by measurements of an impulse pressure response.

While the state-of-the-art collapse-mode CMUT models utilize intrinsically slow FEM^{53,54,56,61}, or equivalent circuit simulations of limited physical insight⁵⁸, our goal is to develop an insightful, electro-mechanical, semi-analytic model that allows fast parameter analysis to guide pre-design of the promising collapse-mode operation of CMUT⁴⁸. We utilize a reduced-order (RO) model for electro-statically actuated clamped circular plates^{62,63}, which we extend for the collapse-mode operation. The governing partial differential equation is discretized using the Galerkin method^{64 p.529–533}. The discretized model is analyzed to obtain both static displacement profiles and dynamic mechanical responses of an arbitrary point on the CMUT plate using time integration. Self and mutual radiations are then introduced to calculate the pressure field from distributed CMUT cells at an arbitrary location. We compare our model in terms of static simulations with state-of-the-art models and DHM measurements of a fabricated CMUT. The modelled dynamic behaviour of the fluid-loaded top plate is validated by acoustic field measurements in water. Using the developed model, frequency-tunability⁶⁵ achieved by adjusting the bias voltage of a collapse-mode CMUT is demonstrated and compared to acoustic measurements of the fabricated frequency-tunable CMUT.

Outline

The following section provides a dimensionless formal description of the dynamic behaviour of an electro-statically actuated circular plate. The shape of the actuated CMUT plate is approximated by a linear combination of a several undamped axisymmetric mode shapes and a Galerkin-discretized version of the equation of motion is introduced including the fluid loading and atmospheric pressure terms. Next, a classical relationship of pressure wave propagation theory is used to translate the CMUT plate acceleration to the pressure at an arbitrary point in the fluid. Section 2.3 describes the fabricated transducer and the experimental digital holographic and acoustic methods used to validate the developed CMUT model. The static and dynamic response of the modelled and measured CMUT are presented in section 2.4 including an indication of the simulation time. The achieved results are discussed in section 2.5. Finally, conclusions are drawn in section 2.6.

2.2 Semi-analytic modelling

Formulation

A schematic overview of the geometrical parameters of a CMUT in collapsed state is shown in Fig. 2.1. The circular plate comprising a top electrode has

a radius a and thickness t_m . It is separated from the bottom electrode by an insulation layer having a total thickness t_i , and a vacuum gap of height t_g . Applying a static (DC) bias voltage V_{bias} to the electrodes causes the movable top plate to deflect towards the bottom electrode, eventually collapsing the center area of the flexible top plate onto the bottom of the cavity. Then AC voltage $V_{\text{AC}}(t)$ is applied to excite the free part of the top plate, marginally relaxing the contact area from the bottom of the cavity (sweeping boundary condition). The CMUT transduces voltage and ultrasound as a result of these plate vibrations.

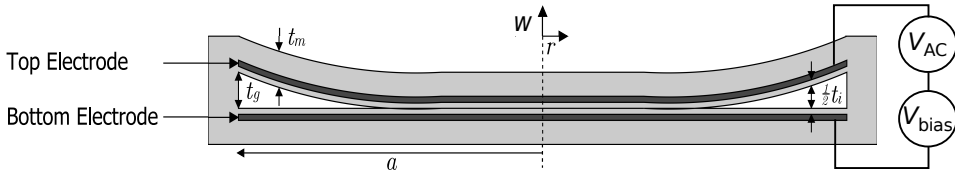


Figure 2.1: A schematic overview of the geometrical parameters of a CMUT in collapsed state.

A CMUT operated in a conventional (non-contact) mode has been modelled previously by a nondimensional equation of motion governing the axisymmetric motion of a thin, isotropic, electro-statically actuated, clamped, circular plate⁶² Eqs. (6)–(7). We adapt and extend this state-of-the-art model for collapse mode operation,

$$\frac{\partial^2 \hat{w}(\hat{r}, \hat{t})}{\partial \hat{t}^2} + \nabla_{\hat{r}}^4 \hat{w}(\hat{r}, \hat{t}) = -\frac{\hat{V}(\hat{t})^2}{2(1 + \hat{w}(\hat{r}, \hat{t}))^2} + \hat{H}_{\text{ab}} \text{erfc}\left(\frac{\hat{t}_g + \hat{w}(\hat{r}, \hat{t})}{\hat{\sigma}}\right) + \frac{\hat{\tau}}{\hat{r}} \frac{\partial}{\partial \hat{r}} \left(\hat{r} \frac{\partial \hat{w}(\hat{r}, \hat{t})}{\partial \hat{r}} \right), \quad 0 \leq \hat{r} \leq 1 \quad (2.1)$$

where the left-hand side is the classical equation describing flexural deformations of a vibrating circular plate. The right-hand side terms model the electrostatic pressure, the contact pressure of the collapsed portion of the CMUT plate⁶⁶ (which is added to the original equation), and the biaxial residual stress⁶⁷, respectively. It is assumed that the plate's transversal displacement is small as compared to its thickness (the ratio typically being smaller than 0.15) and that all stress components can be expressed in terms of a transverse deflection \hat{w} of the plate. Further, it is assumed that no in-plane deformation occurs in the middle plane of the plate and that points lying initially on a normal-to-the-middle plane of the deformed plate remain on its normal in the deformed state. $\hat{V}(\hat{t})$ is the total voltage applied to the electrodes (e.g. $V_{\text{bias}} + V_{\text{AC}}(t)$), erfc is the complementary error function, \hat{H}_{ab} is the effective indentation hardness, $\hat{\sigma}$ is the standard deviation of the combined surface roughness, and $\hat{\tau}$ is the residual stress parameter. For convenience, the model parameters in Fig. 2.1 and Eq. (2.1) are nondimensionalized according to Eq. (2.7) in Appendix A.

The nondimensional boundary conditions for the clamped circular plate in Fig. 2.1 are given by

$$\hat{w}(1, \hat{t}) = \frac{\partial \hat{w}(1, \hat{t})}{\partial \hat{r}} = \frac{\partial \hat{w}(0, \hat{t})}{\partial \hat{r}} = \frac{\partial^3 \hat{w}(0, \hat{t})}{\partial \hat{r}^3} = 0. \quad (2.2)$$

These boundary conditions state that transversal displacements and rotations at radius a ($\hat{r} = 1$) are suppressed, and that rotation and shear force are zero in the middle of the plate ($\hat{r} = 0$).

Model Order Reduction

The partial differential equation (2.1) is approximated by a finite set of coupled ordinary differential equations using Galerkin discretization^{64 p. 529–533}, an efficient and accurate technique commonly used in modelling of electromechanical systems^{62,68}. This technique eliminates the spatial dependence by discretizing the partial differential equation with respect to the spatial coordinates.

The transverse displacement $\hat{w}(\hat{r}, \hat{t})$ is approximated as a linear combination of n linearly independent functions $\phi_i(\hat{r})$

$$\hat{w}(\hat{r}, \hat{t}) \approx \sum_{i=1}^n q_i(\hat{t}) \phi_i(\hat{r}), \quad (2.3)$$

where $q_i(\hat{t})$ is the generalized coordinate associated with the basis function $\phi_i(\hat{r})$.

The basis functions $\phi_i(\hat{r})$ are chosen to be the undamped axisymmetric eigenmodes of a circular plate without residual stress, electrostatic forcing, and contact⁶²,

$$\phi_i(\hat{r}) = \frac{J_0(\hat{r}\sqrt{\Omega_i})}{J_0(\sqrt{\Omega_i})} - \frac{I_0(\hat{r}\sqrt{\Omega_i})}{I_0(\sqrt{\Omega_i})}, \quad (2.4)$$

where J_0 is the Bessel function of the first kind, I_0 the modified Bessel function of the first kind, and Ω_i is the i th nondimensional natural angular frequency. The nondimensional natural frequencies are calculated using the method described in^{69 p. 7}. The number of mode shapes n will be chosen based on a trade-off between simulation accuracy and computational cost. A convergence study has shown that six mode shapes provide a transverse displacement accuracy of less than 2 nm, which is at the order of the expected surface roughness within the CMUT cavity⁵¹.

Fluid Loading

When there are multiple CMUT cells which generate ultrasound to the surrounding medium (which is in contact with the top plates), the acoustic pressure radiation of one cell is affected by other cells in the array⁷⁰. This interaction between cells is commonly referred to as mutual radiation⁶⁰. Similarly, on

a smaller scale, pressure emitted from a point of the plate of one cell influences the top-plate motion of the cell itself, which is referred to as self radiation. Both radiation effects are modelled in the time-domain by meshing the vibrating cell surface into N elements and using the fluid loading term of equation (3) in⁷¹ to calculate the resulting radiation pressure P from all the interacting elements,

$$P(\mathbf{r}, t) = \frac{\rho_{\text{fl}} A \frac{d^2 w(\mathbf{r}, t)}{dt^2} \delta\left(t - \frac{d}{c_{\text{fl}}}\right)}{2\pi d}, \quad (2.5)$$

where ρ_{fl} is the mass density of the surrounding medium, A is the surface of the small mesh element, $\frac{d^2 w(\mathbf{r}, t)}{dt^2}$ is the acceleration of the emitting mesh element, d is the Euclidean distance from one center of an element to another, δ is the Dirac function, and c_{fl} is the speed of sound in the surrounding medium.

The developed model uses a discretized version of Eq. (2.5) with the total number of mesh elements (N) chosen such that every element can be considered to exhibit a piston like motion. A convergence study has shown that a minimum of 6000 mesh elements and six mode shapes is sufficient for the dynamic response prediction by the model.

Reduced-Order Semi-Analytic Model

Adding the dimensionless self and mutual radiation fluid loading terms, \hat{P}_{self} and \hat{P}_{mut} , respectively, and a dimensionless atmospheric pressure term, \hat{P}_{atmos} , to Eq. (2.1) and subsequently applying the Galerkin discretization method results in an extended set of discretized equations of motion,

$$\begin{aligned} \frac{d^2 \mathbf{q}_j(\hat{t})}{d\hat{t}^2} + 2\zeta_j \Omega_j \frac{d\mathbf{q}_j(\hat{t})}{d\hat{t}} + \Omega_j^2 \mathbf{q}_j(\hat{t}) = & - \int_0^1 \frac{\hat{V}(\hat{t})^2}{\left(1 + \sum_{i=1}^n \mathbf{q}_i(\hat{t}) \phi_i(\hat{r})\right)^2} \phi_j(\hat{r}) \hat{r} d\hat{r} + \\ & \int_0^1 \hat{H}_{\text{ab}} \text{erfc} \left(\frac{\hat{t}_g + \sum_{i=1}^n \mathbf{q}_i(\hat{t}) \phi_i(\hat{r})}{\hat{\sigma}} \right) \phi_j(\hat{r}) \hat{r} d\hat{r} + \hat{\tau} \int_0^1 \frac{d}{d\hat{r}} \left(\frac{d \sum_{i=1}^n \mathbf{q}_i(\hat{t}) \phi_i(\hat{r})}{d\hat{r}} \right) \phi_j(\hat{r}) d\hat{r} - \\ & \int_0^1 \hat{P}_{\text{self}}(\hat{r}, \hat{t}) \phi_j(\hat{r}) \hat{r} d\hat{r} - \int_0^1 \hat{P}_{\text{mut}}(\hat{r}, \hat{t}) \phi_j(\hat{r}) \hat{r} d\hat{r} - \int_0^1 \hat{P}_{\text{atmos}} \phi_j(\hat{r}) \hat{r} d\hat{r}, \end{aligned} \quad (2.6)$$

for $j = 1, 2, \dots, n$. Note that on the left-hand side of Eq. (2.6) a viscous modal damping term has been added. For each mode, the dimensionless modal damping coefficient ζ_j may be tuned to account for (secondary) dissipation mechanisms such as material damping, anchor loss, thermoelastic damping, squeeze film damping etc. The self (\hat{P}_{self}) and mutual (\hat{P}_{mut}) radiation pressure terms are calculated from the discretized version of Eq. (2.5) and are, together with the atmospheric pressure term (\hat{P}_{atmos}), nondimensionalized according to the expression Eq. (2.7) in Appendix A.

The generalized coordinates $q_i(\hat{t})$ are found with Eq. (2.6) and thus the transverse displacement $w(\hat{r}, \hat{t})$ via Eqs. (2.3) and (2.4). Static deflection profiles and dynamic responses based on the developed reduced-order model (ROM) described by Eq. (2.6) are determined numerically due to the absence of an analytic solution of Eq. (2.6). Table 2.2 in Appendix B summarizes the model parameter values that were derived from the CMUT design specifications, except for the values of τ and σ , which have been obtained by tuning the model to the experimentally measured static displacement profiles.

Pressure propagation

The dynamic response of a single CMUT cell in an infinite array of CMUT cells is calculated and, for the sake of reducing computational cost, it is assumed to be the response of all individual CMUT cells in the designed octagonal array. In other words, it is assumed that all cells move in-phase. Pressure at an arbitrary point from the CMUT array surface is calculated from all the cell surface accelerations predicted by the RO model using a discretized version of Eq. (2.5)⁷¹.

2.3 Prototype and Experimental Methods

Fabricated Transducer Prototype

The collapse-mode CMUT prototype device is fabricated in a professional cleanroom facility on a 6-inch thick silicon wafer utilizing the standard sacrificial release process, in which the cavity underneath the flexible top plate is created by deposition and subsequent selective etching of a sacrificial metal layer⁷². The complete layerstack of the prototype is provided in Fig. 2.7 in Appendix B.

The fabricated array consists of 932 30- μm -radius CMUT cells on a rectangular grid arranged in an octagonal shape as shown in Fig. 2.2. Each cell has a 3.6- μm spacing with the neighboring cells. All the top electrodes are short-circuited and the same holds for all the bottom electrodes. The whole array is driven as a single element transducer, which avoids extensive wire bonding and signal channel management at an early stage of development. More information on the CMUT design and its patented fabrication process can be found in earlier publications^{65,73}.

The CMUT device is mounted and wirebonded on a printed circuit board (PCB) for experimental characterization. The DC bias and the AC excitation voltage are applied to the CMUT electrodes via a bias-T which features a 5 nF coupling capacitor, a 1 M Ω resistor and a high-impedance probe connector to measure the excitation pulse directly at the PCB.

Digital Holographic Microscopy

A digital holography microscope (DHM; R2100, Lyncée Tec SA, Lausanne, Switzerland), commonly used for CMUT characterization⁵¹, is utilized to val-

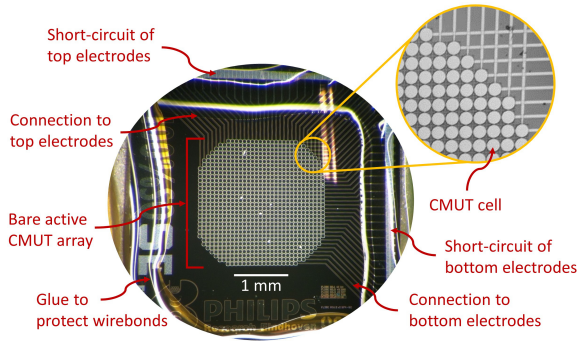


Figure 2.2: Photograph of the fabricated CMUT prototype used for the experimental model validation.

validate the static behaviour of a CMUT cell in air predicted by the RO model. The DHM uses two optical wavelengths of 666 nm and 794 nm to create an interference pattern and to record a digital hologram, which is then converted by the accompanying software into an image.

A single CMUT cell in the center of the array is positioned in a $10\times$ magnified field of view. Multiple 50-times averaged holograms are recorded at a range of bias voltages. A phase unwrapping algorithm calculates the static displacement profiles which are then compared to the RO model results. This configuration allows to measure a vertical displacement range of $2.1\ \mu\text{m}$ with an accuracy of $\pm 3\ \text{nm}$ and a lateral resolution of $1.15\ \mu\text{m}$.

Hydrophone Measurement Setup

A hydrophone measurement is utilized to validate the dynamic behaviour of the RO model. To protect the CMUT from the capacitive and conductive effect of water, it is immersed in a holder filled with olive oil ($c_{fl} = 1432\ \text{m s}^{-1}$), facing an acoustic window. The whole assembly is placed in a water tank. The CMUT is biased and driven with a half period of a 60-MHz 45-V sine. A needle hydrophone ($\varnothing 0.2\ \text{mm}$, Precision Acoustics, Dorchester, Dorset, UK) is placed at a distance of 10.8 mm from the center of the CMUT prototype and used to measure the acoustic output at a range of bias voltages. The recorded voltage traces are converted to pressure waveforms using the hydrophone calibration data and compared to the RO model dynamic response results.

2.4 Static and Dynamic Response Results

Static Behaviour

In Fig. 2.3(a), the static transverse deflection of a single cell CMUT top plate predicted by our RO model is compared to the state-of-the-art collapse-mode CMUT models for bias voltages of 100 V, 120 V, and 140 V. The RO model predicts larger transverse deflections in comparison to the model developed by the

Bilkent University group⁵⁵, which is expected due to uniform electrostatic force assumption in⁵⁵. In comparison to the parametric nonlinear lumped element model developed by the same group⁵⁸, in which the uniform force assumption was removed, the RO model shows a maximum deviation of 1 nm (0.4 % of the gap height).

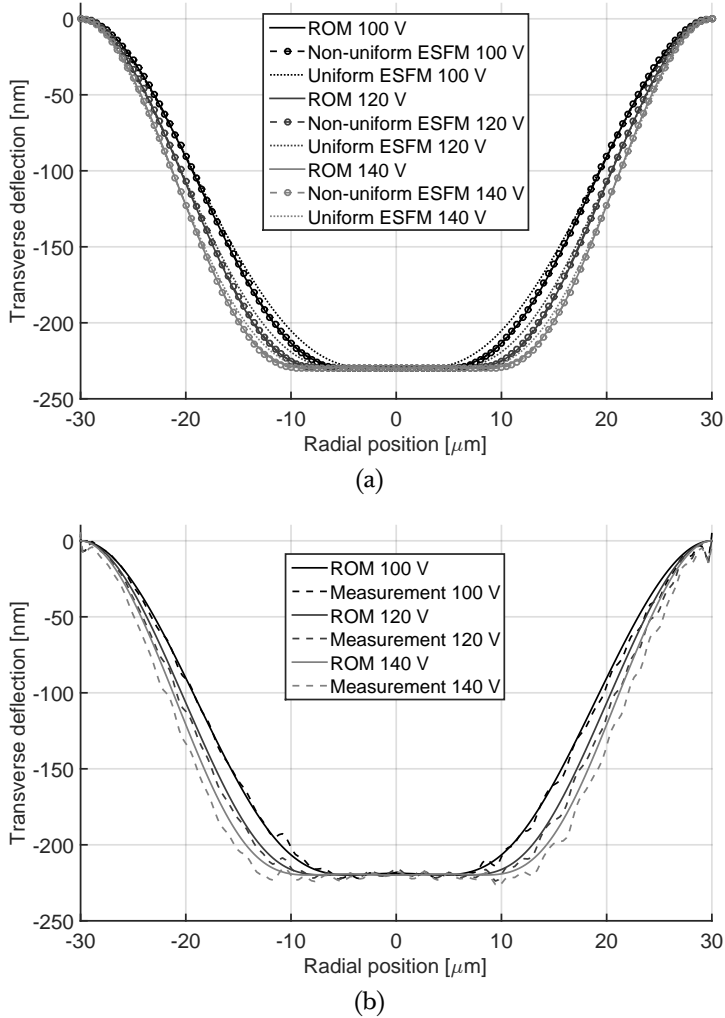


Figure 2.3: Static response of the reduced-order model (ROM) compared to state-of-the-art uniform⁵⁵ and non-uniform⁵⁸ electrostatic force model (ESFM) of a collapse-mode CMUT (a), and validated towards measurements with a digital holographic microscope (b).

The static behaviour predicted by the RO model is validated towards DHM displacement measurements of a fabricated CMUT cell. During the measurements dielectric charging effect has been observed⁷⁴, which resulted in a DC

bias offset of about 20 V. It was found that the amount of charge saturates after minimally three pulses have been applied to the device. The offset of the zero voltage point was therefore carefully monitored by measuring the positive and negative pull-in voltages. The measured bias voltage was corrected for the induced offset for a fair comparison to the RO model.

As shown in Fig. 2.3(b), the RO model accurately predicts the static response for the bias voltage of 100 V and 120 V. The model slightly underestimates the deflection profile at the higher bias voltage of 140 V. The maximum deviation of the model prediction from the measurement is about 10 nm (4 % of the gap height).

The hysteresis behaviour of the CMUT predicted by the RO model is in a good agreement with the DHM static measurements as shown in Fig. 2.4. The model predicts the plate pull-in and pull-out voltages of 55 V and 59 V, respectively, which match well the experimental observation.

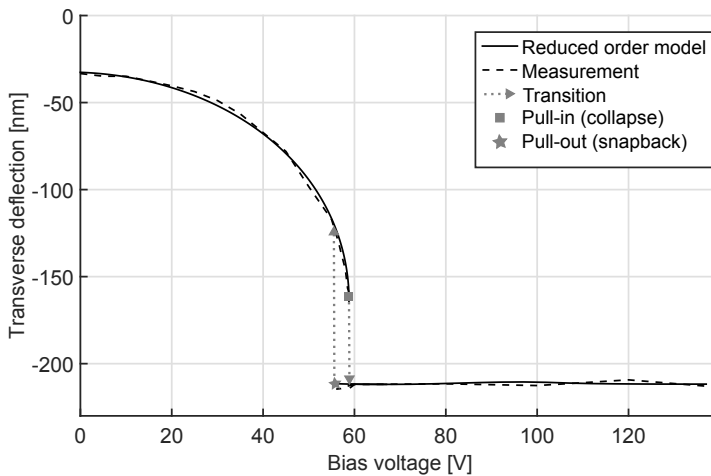


Figure 2.4: Static deflection of the middle point (at $r = 0$) on the CMUT plate in relation to the bias voltage.

Dynamic Behaviour

The static deflection profiles are used as initial conditions for the dynamic simulations under electrostatic actuation. The RO model is utilized to simulate the dynamic plate deflections of both a detached single CMUT cell and a CMUT cell in an infinite array, both immersed in water. Half a period of a 100-MHz 60-V squared sine ($V_{AC}(t) = 60 \sin^2(10^8 T t)$, where $0 \leq T \leq \pi$) is used as the dynamic excitation signal for the simulation. Figure 2.5(a) shows the time responses and Fig. 2.5(b) the corresponding frequency spectra of the transversal displacement at a radial position of 15 μm on the top plate of the CMUT cell. A shorter response and therefore broader bandwidth is obtained for the CMUT cell within an infinite array of CMUT cells as compared to the detached single

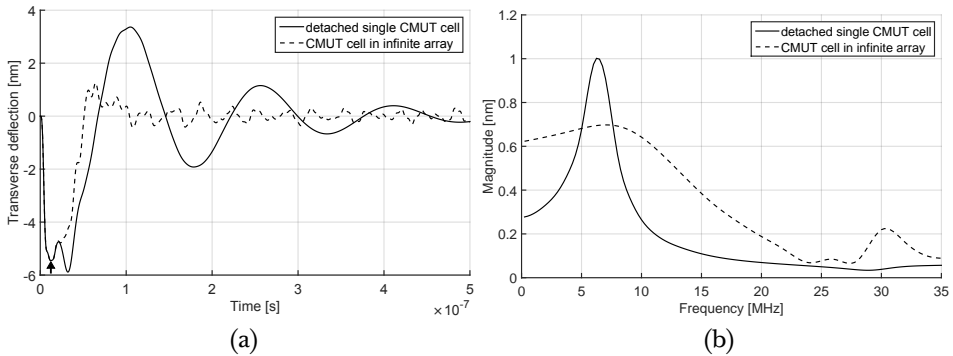


Figure 2.5: Simulated impulse (a) and frequency (b) response of a point at $15 \mu\text{m}$ radius on a CMUT cell plate biased at 120 V, excited with half a period of a 100-MHz 60-V squared sine, and immersed in water. The arrow in (a) indicates a time stamp at which the first mutual radiation forces reach the chosen radial position.

CMUT cell. This can be explained by the mutual radiation forces (that are obviously lacking in the case of the single cell) damping out the motion of the CMUT plate in the infinite array earlier. During the first few nanoseconds, only the self radiation is acting on the CMUT cell and thus the two responses are similar. The first mutual radiation forces reach the chosen radial position of the analysed cell after 12.5 ns, which is the minimum time needed for sound to travel from a neighbouring CMUT cell. For the cell in the infinite array of CMUT cells, a minor overshoot is observed after about 50 ns followed by negligible steady-state vibrations giving a second peak at 30-MHz in the corresponding spectrum shown in Fig. 2.5(b). The peak resonance frequency of the CMUT top plate is 6.5 MHz and 7.5 MHz for the detached and the infinite array configuration, respectively.

Capacitive and conductive effects of water make direct immersion of a CMUT into water for a subsequent validation infeasible. Typically, a non-conductive oil is used instead of water, which is however not compatible with the immersion objective of our DHM. Therefore, and in line with further investigation, the dynamic part of the model was validated towards hydrophone measurements.

The dynamic pressure measurements utilized half a period of a 60-MHz 45-V sine as an excitation signal to the CMUT. The excitation signal was experimentally measured at the PCB and used as an input to the RO model for a fair comparison of the modelled dynamic behaviour to the measurements.

Figs. 2.6(a) and 2.6(c) compare the RO model-predicted pressure waveform towards the acoustic measurement for bias voltages of 100 V and 160 V, respectively. The overall shape of the simulated waveforms is in a satisfactory agreement with the measurement, even though the absolute amplitude is significantly overestimated by the RO model. The subtle waves in the time signals between $7.0 \mu\text{s}$ and $7.3 \mu\text{s}$ in Figs. 2.6(a) and 2.6(c) are caused by a discontinuity

in the hydrophone calibration data curve below 1 MHz and above 30 MHz.

Frequency spectra corresponding to the pressure waveforms are shown in Figs. 2.6(b) and 2.6(d). At a bias voltage of 100 V (Fig. 2.6(b)), center frequencies of 12.9 MHz and 11.1 MHz are observed for the RO model-predicted and experimentally measured frequency spectra, respectively. Increasing the bias voltage to 160 V (Fig. 2.6(d)), shifts the center frequency of the RO model-predicted and measured responses to 16.6 MHz and 16.1 MHz, respectively. This effect has been experimentally observed and described as the frequency-tunability^{65,75}.

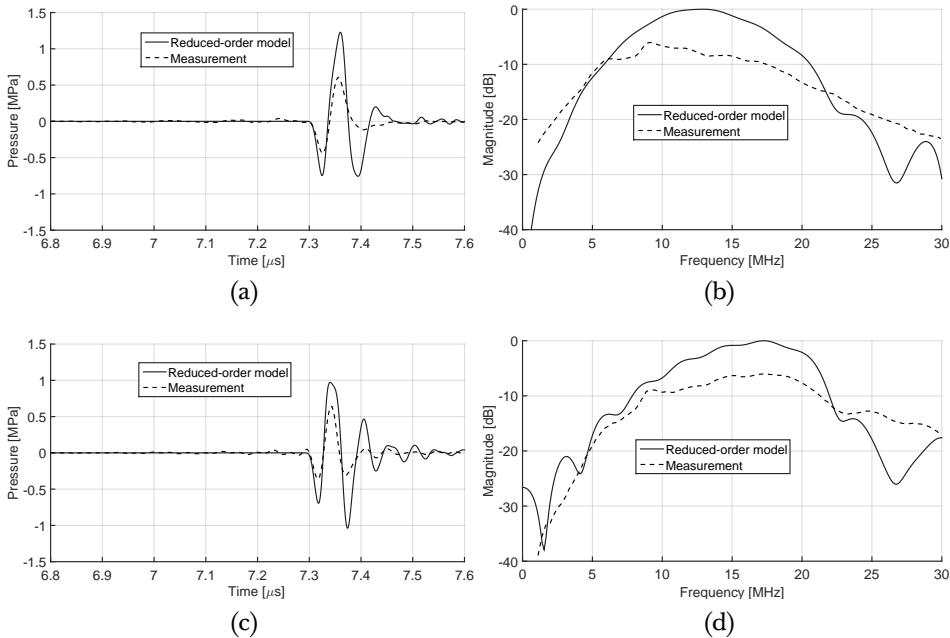


Figure 2.6: Acoustic impulse (a – c) and frequency (b – d) response of the simulated and fabricated CMUT array excited with half a period of a 60-MHz 45-V sine and biased at 100 V (a – b) and 160 V (c – d). The reference pressures corresponding to the 0 dB magnitudes equal to 13.6 kPa (b) and 13.1 kPa (d).

Simulation Time

The simulation time needed to generate the RO model deflection profiles shown in Fig. 2.3(a), was about 10 s on a laptop equipped with 2.3 GHz Intel Core i5 processor and 8 GB RAM. This is comparable to about 45 s needed for the lumped element model implementation published in⁷⁶, when the same zero-deflection initial guess is used. The dynamic behaviour is predicted by the RO model within 30 min for the detached single CMUT cell and it takes about 65 min for the CMUT cell in an infinite array (Fig. 2.5), which is in general faster as compared to a finite-element method (FEM) simulation.

2.5 Discussion

The developed semi-analytic electro-mechanical fluid-coupled RO model predicts both the static and dynamic behaviour of a collapse-mode CMUT. The static deflection profiles are predicted within an accuracy of 10 nm (4 %) for the worst case scenario, which is observed at a bias voltage of 140 V, as validated with the DHM measurements. The model captures the hysteresis behaviour of the CMUT and predicts pull-in and pull-out voltages, which are in a good agreement with the experimental observation.

The RO model has been utilized to simulate an impulse response of a detached single CMUT cell and a cell in an infinite array (Fig. 2.5). It has been found that mutual radiation forces significantly affect the CMUT's dynamic response in immersion. A CMUT cell in an infinite array exhibits larger bandwidth due to the increased damping caused by the mutual radiation as compared to a single detached cell. The geometrical distribution of the CMUT cells in an array will therefore influence the bandwidth of CMUT response. As an alternative for the current rectangular grid CMUT array, another array grid design might be considered to increase the CMUT's bandwidth.

The dynamic behaviour of the CMUT is captured with a satisfactory accuracy as validated towards the acoustic measurements (Fig. 2.6). The model demonstrates the center frequency-tunability in a range from 12.9 MHz (−3 dB fractional bandwidth of 63 %) to 16.6 MHz (bandwidth of 47 %) by changing the bias voltage from 100 V to 160 V. For the same voltage range, the acoustic measurements show tunability from 11.1 MHz (bandwidth of 82 %) to 16.1 MHz (bandwidth of 60 %). Both the simulations and experiments at the different bias voltages indicate that the frequency tuning comes at a cost of additional ringing observed after 7.4 μ s in Fig. 2.6(c). An increase in the bias voltage from 100 V to 160 V leads to a larger contact radius, which in turn results in a higher natural resonance frequency. However, at the same time the CMUT plate vibrates longer. This effect is observed by an (undesired) increased number of cycles in the high frequency pressure waveform simulated or measured at the bias voltage of 160 V (Fig. 2.6(c)).

The difference in amplitude of the simulated and measured waveforms shown in Figs. 2.6(a) and 2.6(c), may be explained by the simplifying assumption of identical response of all the CMUT cells, since it is known that the edge cells have a different response due to the different mutual radiation impedance^{70,77}. The developed model features a damping term, of which the coefficients ζ_j were set to zero for the fluid-loaded simulation. This is a commonly accepted approach, because the „damping“ is expected to be dominated by the fluid load (modelled by the self and mutual radiation) rather than by mechanical losses in the CMUT plate^{60,78}. The amplitude deviation between the simulation and measurement, especially of the second minima shown in Figs. 2.6(a) and 2.6(c), however, indicates that in the case of a collapse-mode CMUT secondary damping mechanisms may play an important role, e.g. contact damping, anchor loss, thermoelastic damping, squeeze film damping etc.

In the presented model, the shape of the deflected plate is modeled as a lin-

ear combination of six free vibrational mode shapes and, for the purpose of radiation modelling, meshed by a limited number of (piston) elements. The number of mode shapes and meshing elements is chosen based on a trade-off between model accuracy and computational cost. Advanced symmetry configurations could be considered to increase the speed of the model and therefore to allow for a larger number of mode shapes and mesh elements. Although the model was developed for a circular plate design, it can be used for any other simple geometry, e.g. a square or rectangular design, that can be approximated by analytic mode shapes.

In the current situation, the RO model features two tuning parameters, the uniform residual biaxial plane stress ($\hat{\tau}$) and the combined surface roughness ($\hat{\sigma}$). In future work, fabrication of multiple CMUTs of at least two different plate radii could be utilized to estimate the initial plane stress using the procedure described in⁵¹. To measure the surface roughness, a sample would have to be cut through and measured with a stylus profiler.

Finally, it is recommended to couple the developed model to an ultrasound image simulator. For instance, a Field II ultrasound simulation program⁷⁹ requires transducer's surface acceleration to excitation voltage response as an input for the transducer definition⁸⁰. Such a response prediction is readily available in our model and can be therefore utilized directly in the Field II to predict the imaging performance of a given collapse-mode CMUT design.

2.6 Conclusions

We have developed and validated an electro-mechanical, semi-analytic, reduced-order model of a CMUT operated in collapse mode. The step-wise validation shows that our model, based on six vibrational mode shapes, predicts the static response including hysteresis behaviour of a collapse-mode CMUT with a high accuracy, which is computed within 10 s. The dynamic response and frequency-tunability are modelled with a satisfactory accuracy and computed within 65 min. Compared to FEM-based simulation methods, our model allows fast parameter analysis for larger penetration depths and is an accurate tool for CMUT pre-design. In future work, it is recommended to interface the developed model with an ultrasound image simulator to obtain a powerful tool that would link the CMUT design parameters with imaging performance.

Acknowledgments

The authors would like to thank Michel van Bruggen and Chris van Heesch for their effort and support in this study. This research is in part funded by Seventh Framework Programme project „OILTEBIA“, grant no. 317526.

Appendices

The appendices introduce dimensionless parameters used in the equation of motion and provide an overview of the parameter values.

Appendix A: Dimensionless model parameters

The model parameters and variables in Fig. 2.1, and mentioned in Eq. (2.1) and Tab. 2.2 are nondimensionalized according to the following expressions, partly given in an earlier publication⁶² Eq.(6),

$$\begin{aligned}
 \hat{r} &= \frac{1}{a}r & \hat{t} &= \frac{1}{a^2} \sqrt{\frac{D}{\rho_{tp} t_m}} t \\
 \hat{w}(\hat{r}, \hat{t}) &= \frac{1}{t_{\text{eff}}} w(r, t) & \hat{\tau} &= \frac{a^2 t_m}{D} \tau \\
 \hat{H}_{ab} &= \frac{a^4}{2Dt_{\text{eff}}} H_{ab} = \frac{a^4 H_a H_b}{2Dt_{\text{eff}}(H_a + H_b)} & \hat{\sigma} &= \frac{\sqrt{\pi}}{t_{\text{eff}}} \sigma \\
 \hat{t}_g &= \frac{1}{t_{\text{eff}}} t_g & \hat{V}^2 &= \frac{\varepsilon_0 a^4}{2Dt_{\text{eff}}^3} V^2 \\
 \hat{P}_{\text{self}}(\hat{r}, \hat{t}) &= \frac{a^4}{Dt_{\text{eff}}} P_{\text{self}}(r, t) & \hat{P}_{\text{mut}}(\hat{r}, \hat{t}) &= \frac{a^4}{Dt_{\text{eff}}} P_{\text{mut}}(r, t) \\
 \hat{P}_{\text{atmos}} &= \frac{a^4}{Dt_{\text{eff}}} P_{\text{atmos}} & & (2.7)
 \end{aligned}$$

Appendix B: Transducer and model parameters

Figure 2.7 shows the layerstack of the fabricated and modelled CMUT device, of which the geometrical and mechanical properties are summarized in Tab. 2.1.

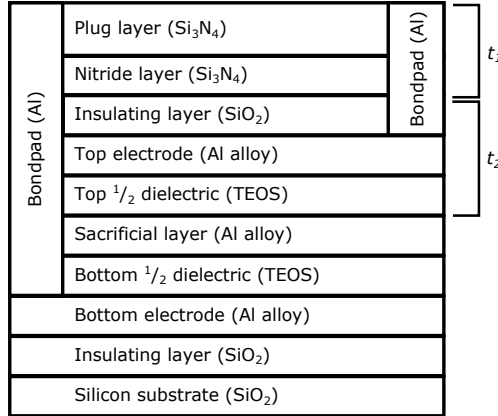


Figure 2.7: Material layers of the fabricated CMUT stack reproduced from an earlier publication⁶⁵. t_1 and t_2 represent the first and second effective layers, respectively.

In a good approximation, the top layer is assumed to consist of a double-layered plate having an effective flexural rigidity D calculated as⁸¹

Table 2.1: Thickness and mechanical Properties of the CMUT layers indicated in Fig. 2.7.

Layer material	Thickness [nm]	E [GPa]	ν [-]	Effective parameter		
				Layer	E [GPa]	ν [-]
Plug layer	900	200	0.27	t_1	200	0.28
Nitride layer	150	200	0.27			
Insulating layer	50	70	0.3	t_2	70	
Top electrode	240	70	0.3			
Top 1/2 dielectric	225	70	0.3			

$$D = \frac{E_1^2 t_1^4 + E_2^2 t_2^4 + 2E_1 E_2 t_1 t_2 (2t_1^2 + 2t_2^2 + 3t_1 t_2)}{12(E_1 t_1 + E_2 t_2)(1 - \nu^2)}, \quad (2.8)$$

where t_1 and E_1 are the total thickness and average Young's modulus of the plug and nitride layers, respectively; t_2 and E_2 are the total thickness and average Young's modulus of the insulating layer, top electrode, and top-half dielectric, respectively; ν is the Poisson's ratio of the complete top plate.

The insulating dielectric layer inside the CMUT cavity can be modelled as an increased distance (effective gap height) between the two electrodes placed in vacuum

$$t_{\text{eff}} = t_g + \frac{t_i}{\epsilon_r}, \quad (2.9)$$

where ϵ_r is the relative permittivity of the dielectric material, t_g is the gap height, and t_i is the total dielectric layer thickness.

The RO model parameter values are summarized in Tab. 2.2. The values of τ and σ are obtained by fitting the RO model to experimentally measured static displacement profiles.

Table 2.2: Parameters of the reduced-order model.

Parameter	Value	Unit	Description
a	$30 \cdot 10^{-6}$	m	Plate radius
ϵ_0	$8.85 \cdot 10^{-12}$	F m ⁻¹	Dielectric permittivity of vacuum
ϵ_r	4.3	–	Relative dielectric permittivity of insulator
t_g	$230 \cdot 10^{-9}$	m	Gap height
t_i	$450 \cdot 10^{-9}$	m	Insulator thickness
t_{eff}	$3.347 \cdot 10^{-7}$	m	Effective gap height
t_m	$1.565 \cdot 10^{-6}$	m	Plate thickness
D	$4.092 \cdot 10^{-8}$	N m	Flexural rigidity of plate
P_{atmos}	$101.325 \cdot 10^6$	Pa	Atmospheric pressure
τ	$-100 \cdot 10^6$	Pa	Uniform residual biaxial plane stress
σ	$4 \cdot 10^{-9}$	m	Combined surface roughness standard deviation
$H_n, n = a, b$	$2 \cdot 10^9$	Pa	Effective indentation hardness ⁸²
ρ_{tp}	3290	kg m ⁻³	Combined mass density of the top plate
c_{fl}	1483	m s ⁻¹	Speed of sound in water
ρ	100	kg m ⁻³	Mass density of water
$\zeta_j, j = 1, 2, \dots, 6$	0	–	Modal damping coefficients

Frequency Tuning of Collapse-Mode CMUT

This chapter has been published as:
Martin Pekař, Nenad Mihajlović, Gijs van Soest, and Nico de Jong, Frequency Tuning of Collapse-Mode Capacitive Micromachined Ultrasonic Transducer, *Ultrasonics* 74, pp. 144-152 (2017).

Abstract

The information in an ultrasound image depends on the frequency that is used. In a clinical examination it may therefore be beneficial to generate ultrasound images acquired at multiple frequencies, which is difficult to achieve with conventional transducers. Capacitive micromachined ultrasonic transducers (CMUTs) offer a frequency response that is tunable by the bias voltage. In this study we investigate this frequency tunability for ultrasonic imaging. We characterized a CMUT array operated at bias voltages up to three times higher than the collapse-voltage. All elements of the array were connected to a single transmit and receive channel through a bias circuit. We quantified the transmit-receive and transmit sensitivity as a function of frequency for a range of bias voltages. Impulse response measurements show that the center frequency is modifiable between 8.7 MHz and 15.3 MHz with an applied bias voltage of -50 V to -170 V. The maximum transmit sensitivity is 52 kPa V^{-1} at a center frequency of 9.0 MHz with an applied bias voltage of -105 V. The -3 dB transmit range in center frequency accessible with the variable bias voltage is 6.7 MHz to 15.5 MHz. This study shows that a collapse-mode CMUT can operate efficiently at multiple center frequencies when the driving pulse and the bias voltage are optimized. We demonstrate the usefulness of frequency tuning by comparing images at different optimal combinations of driving frequency and bias voltage, acquired by linearly moving the transducer across a tissue mimicking phantom.

3.1 Introduction

Medical imaging typically uses a portion of the ultrasound spectrum from 1 MHz to 40 MHz, optimizing a tradeoff between good resolution and good penetration ability. The lower frequency portion up to 5 MHz is typically used for abdominal and cardiac imaging; carotid scans require frequencies of 7 MHz – 10 MHz. Intracardiac echo (ICE) utilizes frequencies between 5 MHz and 8 MHz, which still allow seeing a whole adult heart in a four chamber view. Frequencies higher than 15 MHz are typically used in intra-vascular imaging applications where the transducer is in the proximity of a structure to be visualized.

In conventional grayscale B-mode imaging, it is usually easy to swap out low- and high-frequency probes during an examination. In situations where access is complicated (minimally-invasive imaging), or when precise coregistration of data at different frequencies is vital (harmonic imaging), use of multiple transducers is impractical at best, and often impossible. Here, we study a device that was designed for ICE, in which the imaging frequency range from 5 MHz to 25 MHz would allow both orientation and navigation of instruments (e.g. transseptal puncture needle) inside the heart as well as close and detailed look-up at heart pathologies (e.g. structural heart diseases, lesions, thrombi). This is difficult to achieve with conventional piezoelectric transducers, e.g. commercial ICE catheters are based on piezoelectric materials and their –6 dB bandwidth does not exceed 60 %⁸³. We fabricated a collapse-mode capacitive micromachined ultrasonic transducer (CMUT) that offers a frequency response that is tunable by the bias voltage. The goal of this study is to investigate its frequency tunability, quantified as the maximum bandwidth accessible with variable bias voltage, within the range of 5 MHz – 25 MHz.

In conventional resonant transducer design the material, volume, and shape determine the resonance frequency. In general, a thicker element has a lower resonance frequency than a thinner element of the same shape. It is well known that the use of a matched lossy backing material improves the bandwidth at the expense of transducer sensitivity. The large difference in acoustic impedance of piezoelectric transducers ($Z = 30 \text{ MRayl}$) and water ($Z = 1.5 \text{ MRayl}$) requires fabrication of a wavelength-specific matching layer, which is challenging to achieve for a broad range of high frequencies (5 MHz – 25 MHz). Non-resonant transducer technology exhibiting large bandwidth and acoustic impedance close to water has been proposed in literature⁸⁴. Although bandwidths of over 100 % are routinely achieved with polymer transducers, the low coupling efficiencies (< 0.2) compromised performance in the clinical frequency range⁸⁵. For more than two decades, CMUT have been investigated as another ultrasound transducer technology²⁷ relying on a different physical operational mechanism and achieving large bandwidth (100 %)⁸⁶, low acoustic impedance ($< 1.5 \text{ MRayl}$)²⁹, and high coupling efficiency (≈ 1)⁵³. The manufacturing process of CMUT enables batch fabrication of small kerf arrays having elements of arbitrary shape and size, and allows monolithical integration of front-end electronics²⁸.

A CMUT consists of an insulated plate with a thickness of a few microns

(commonly referred to as „membrane“) positioned over a cavity crafted in a silicon support. An applied DC (bias) voltage causes the plate to bend. A further increase in the bias voltage brings the plate in contact with the few hundred nanometer-thin dielectric layer which is on top of the ground electrode at the bottom of the cavity; the plate is in a collapsed state. The collapse voltage is determined by the geometrical and electro-mechanical plate properties⁵⁸; a typical value is around 60 V for a 30- μm -radius CMUT plate.

„Collapse mode“ refers to the dynamic use of CMUT plates in the collapsed state. Application of a dynamic AC voltage causes the bent plate to vibrate as a thin annular plate clamped on both the outside and inside. An additional bias voltage increase beyond the collapse value brings the plate deeper in collapse, in which the contact radius increases, typically from 20 % to 50 % of the plate radius, together with resonance frequency of the CMUT⁵⁵. Its performance can be therefore optimized by setting the appropriate bias voltage for every driving pulse frequency.

The lower bound of the tuning range of the resonance frequency of a collapse-mode CMUT is limited by the minimum voltage that can be applied to the plate without releasing it from the cavity. Such a voltage is determined by the material properties and the geometry, and is typically 30 V – 60 V⁸⁷. The upper bound is given by a maximum voltage that can be applied, which is determined by a breakdown voltage of the insulating layer, typically around 220 V for a 500-nm thick dielectric layer⁸⁸. In general, at any time the sum of the bias and AC voltages applied to a CMUT operated in collapse-mode must be higher than the so called snapback voltage and lower than the dielectric breakdown voltage.

Figure 3.1 gives an overview of the state-of-the-art research on different modes of operation of CMUT. In 2006 Oralkan et. al.⁸⁹ demonstrated a single CMUT of which the center frequency can vary from 10 MHz to 12 MHz in conventional mode and the same transducer operates in the frequency range from 20 MHz to 28 MHz in pre-snapback and collapse mode; however no work on frequency tuning and imaging with a (deep-)collapse-mode CMUT is shown. Nevertheless, this dual-frequency operation was utilized by Yeh et al.⁹⁰ to generate ultrasound images with a single CMUT operated in the conventional and collapse mode. The collapse mode received a lot of attention due to its three-fold increased output pressure as shown by Park et al.⁸⁶ and Olcum et al.⁵⁵, and due to a 15 dB lower element to element cross-talk as demonstrated by Bayram et al.⁵⁴. Although Park et al.⁸⁶ aim at comparing conventional and collapse-mode CMUT designs in terms of pressure output, no frequency responses at various bias voltages are investigated. Recently, the ability of CMUT to tune its resonance frequency in conventional (1 MHz – 3 MHz), collapse (3.8 MHz – 5 MHz) and deep-collapse (5 MHz – 16 MHz) mode was modelled by Aydođdu et al.⁵⁸. In this work, we aim to explore the latter observation experimentally, demonstrating an accessible frequency band for imaging that is wider than the instantaneous response at a single bias voltage.

The frequency response of a CMUT biased at different voltages is schematically illustrated in Fig. 3.2 and compared to the fixed frequency response of

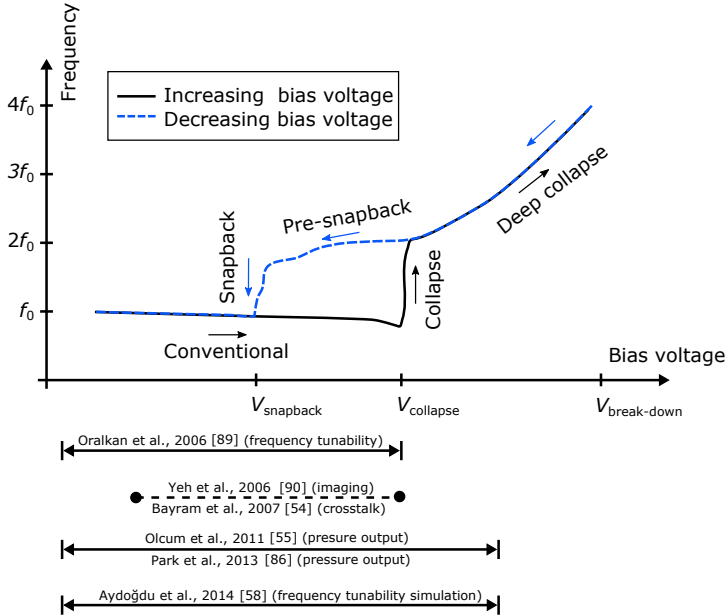


Figure 3.1: Overview of the state-of-the-art research on different modes of operation of CMUT (schematic drawing not representing any particular CMUT design, based on^{58,89}). Typical collapse voltage is around 60 V, snapback voltage ranges 30 V – 60 V and the typical breakdown voltage is about 220 V, depending on the insulation layer thickness.

a piezoelectric transducer. Although the bias voltage tuning of the CMUT’s frequency response is known⁸⁹, no multi-frequency ultrasound images acquired over a continuous range of frequencies with CMUT have been shown in literature yet. This may be related to manufacturing difficulties⁹¹ or limitations in life-time and reliability⁹².

The new contribution of our work is in characterization of the CMUT’s ability to tune its operating frequency continuously while in collapse mode (as opposed to discretely, between conventional and collapse). This behavior is referred to as „frequency tunability“, which we define as the maximum bandwidth accessible with variable bias voltage. Our design aims to utilize the frequency tunability for intracardiac imaging. We provide a rudimentary proof of principle for multi-frequency imaging with CMUT operated solely in the collapse-mode at voltages up to three time higher than the collapse voltage and we investigate the reciprocity of the CMUT.

The paper is organized as follows. The first part briefly describes fabrication and assembly of the CMUT. Then the impulse response of the CMUT is measured at a range of bias voltages in transmit-receive and compared to the transmit-only impulse response to qualitatively evaluate reciprocity of the device. Next, the CMUT transmit sensitivity is quantified as a function of frequency for a range of bias voltages and CMUT’s reliability is tested. The trans-

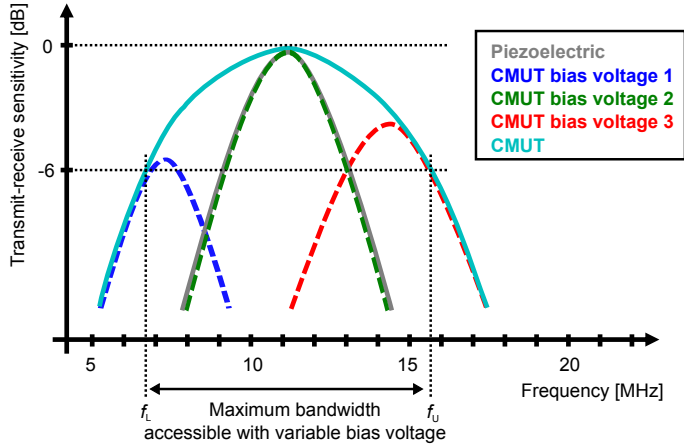


Figure 3.2: Schematic comparison of a frequency response of a piezoelectric transducer and a CMUT.

mit sensitivity curve is used as an input for imaging, where the frequency of the driving pulse is matched with the bias voltage to obtain the maximum transmit sensitivity. The last part presents typical images at three different combinations of driving frequency and bias voltage.

3.2 Materials and Methods

Fabrication and assembly

We fabricate the CMUT in a professional cleanroom facility on a 6-inch 670- μm thick silicon wafer utilizing the standard sacrificial release process, in which the cavity underneath the membrane is created by deposition and subsequent selective etching of a sacrificial metal layer⁷². Common micro-electro-mechanical systems (MEMS) processing steps are used to manufacture the transducer stack: metal sputtering, primer deposition, spinning of a photoresistive layer, patterning by means of light exposure over a photolithographic mask, photoresistive layer development, wet and dry etching, photoresistive layer stripping with acetone or oxygen plasma and plasma enhanced chemical vapour deposition of the insulating layer. The final transducer stack consists of a silicon wafer covered with silicon dioxide for passivation, an bottom electrode insulated with TEOS (tetraethoxysilane), vacuum cavity created using the sacrificial release process, a TEOS insulated top metal electrode covered with silicon oxide and a nitride plug layer on the top. Apart from the plates, aluminium bond pads providing contact to the top or bottom electrodes are created on the side of the array to allow for wire bonding. More information on the patented fabrication of the CMUT can be found in⁷³. The complete layer stack including the layer materials and thicknesses is shown in Fig. 3.3.

The fabricated array consists of 30- μm -radius CMUT cells arranged in an oc-

Bondpad (Al)	Plug layer (Si_3N_4), 790 nm	Bondpad (Al)
	Nitride layer (Si_3N_4), 150 nm	
	Insulating layer (SiO_2), 50 nm	
	Top electrode (Al alloy), 240 nm	
	Top $\frac{1}{2}$ dielectric (TEOS), 250 nm	
	Sacrificial layer (Al alloy), 230 nm	
	Bottom $\frac{1}{2}$ dielectric (TEOS), 250 nm	
	Bottom electrode (Al alloy), 240 nm	
Insulating layer (SiO_2), 2000 nm		
Silicon substrate (SiO_2), 670 μm		

Figure 3.3: Layer stack of the fabricated CMUT.

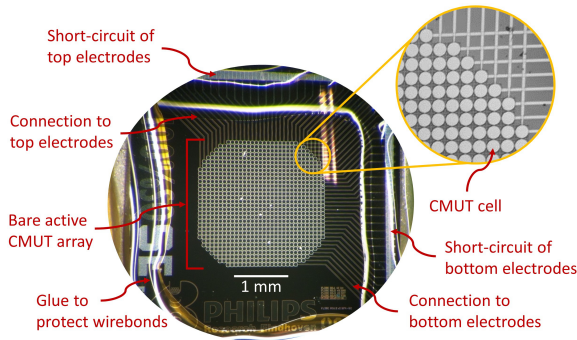


Figure 3.4: Photograph of the CMUT wire-bonded to a PCB.

tagonal shape to fit a 9 F aperture. Each cell has a $3.6 \mu\text{m}$ spacing with the neighboring cells resulting in a pitch of $63.6 \mu\text{m}$ ($< \frac{\lambda}{2}$ at 12 MHz). Both the top and bottom electrodes are short-circuited so that the whole device can be driven as a single element transducer. This avoids extensive wire bonding and signal channel management at an early stage of development.

The collapse voltage is measured on wafer level by measuring the CMUT's capacitance in air as a function of bias voltage. The bias voltage is decreased from 0 V to -128 V in 160 steps. The collapse voltage is defined as the minimum of the first derivative of the measured capacitance curve. The fabricated CMUT collapses when a bias voltage of -59 V is applied. The snapback voltage is measured in a similar way, except with the bias voltage being reversed, and is defined as the maximum of the first derivative of the measured capacitance curve. The fabricated CMUT snaps back at -56 V .

The fabricated CMUT devices are diced from a wafer, glued and wirebonded to a PCB (printed circuit board). Due to the single element design described above only a single channel is needed to operate the CMUT. The sample is coated with a thin layer (about $40 \mu\text{m}$) of a silicone-like material for electrical

insulation of the bondpads and passivation of the CMUT cells. There is no lens provided with the CMUT. A photograph of the fabricated CMUT glued to a PCB is shown in Fig. 3.4.

Impulse response

The transmit-receive response of the CMUT is measured in a pulse-echo setup. The CMUT is connected as a single element to one transmit-receive channel of a custom ultrasound imaging system (Philips Research, Eindhoven, the Netherlands) having a -6 dB bandwidth of 4.8 MHz $- 50.3$ MHz. The CMUT is immersed in water and positioned in the far field at a distance of 9 mm from a metal ball reflector (diameter of 5 mm), which allows more robust alignment compared to a flat reflector⁸³. The CMUT is biased at different voltages (E 0300-0.1; Delta Elektronika, Zierikzee, the Netherlands) ranging from -70 V down to -170 V in steps of -10 V, and driven with a 20 -ns 19 -V unipolar negative impulse generated by the ultrasound system.

The transmit impulse response is measured with a hydrophone. The CMUT immersed in a water tank is biased with a DC voltage source (Keithley 237; Keithley, Cleveland, Ohio, USA) at -70 V to -170 V in steps of -5 V, and excited with unipolar negative 20 -ns 20 -V impulse generated by an arbitrary wave generator (Agilent 33250A; Agilent, Santa Clara, California, USA) and an amplifier (ENI 350L RF; Electronic Navigation Industries, Rochester, New York, USA) as schematically shown in Fig. 3.5. The acoustic output is measured with a calibrated needle hydrophone of 0.2 mm in diameter (Precision Acoustics, Dorchester, Dorset, UK). The needle hydrophone is located at a distance of 9 mm on the central axis of the CMUT array. The voltage signal received on the hydrophone is digitized (NI-6545; National Instruments, Austin, TX, USA) and converted into output pressure using the hydrophone calibration data which are available up to 30 MHz.

The spectra of the received signals are analysed and plotted as the frequency response of the CMUT at different bias voltages. The center frequency, fractional bandwidth, pulse length (maximum pulse length at -20 dB of the maximum amplitude), and sensitivity are calculated as a function of the bias voltage. The transmit-receive sensitivity is defined as the ratio of the peak-to-peak received voltage signal to peak-to-peak voltage of the excitation pulse. In addition to this conventional parametrization of transducer frequency response at a fixed bias voltage, we quantify the frequency tunability Δ_F as the maximum bandwidth achievable with variable bias voltage:

$$\Delta_F = F_U - F_L, \quad (3.1)$$

where F_L and F_U are the lower and upper band edges, respectively at either 6 dB for transmit-receive or -3 dB for transmit-only. The band edges are evaluated in the frequency spectra at variable bias voltage. The term „variable bias voltage“ refers to the bias voltage setting which gives the highest sensitivity at the given frequency.

To evaluate the reciprocity of the CMUT's transmit and receive response, the spectra of the one-way impulse responses measured by the hydrophone at

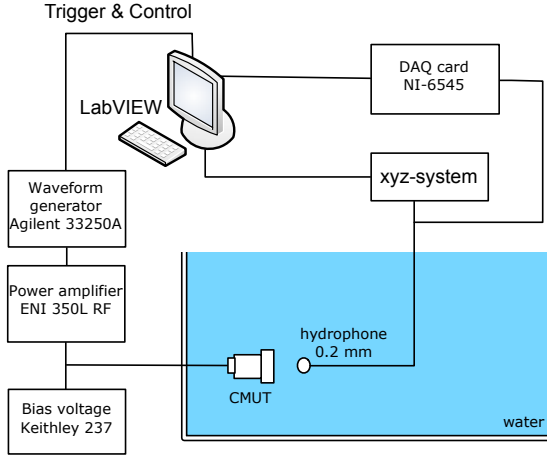


Figure 3.5: Schematic of the hydrophone set-up.

different bias voltages are squared and compared to the two-way impulse responses measured in the pulse-echo set-up. The two sets of spectra are normalized to their respective maximums. The comparison of the CMUT transmit and receive frequency responses allows validation of the assumed reciprocity according to the convolution theorem:

$$H_{\text{tx-rx}}(\omega) = |H_{\text{tx}}(\omega)|^2 = \mathfrak{F}\{h_{\text{tx}}(t)\}^* \cdot \mathfrak{F}\{h_{\text{tx}}(t)\}, \quad (3.2)$$

where $H_{\text{tx-rx}}(\omega)$ is the transmit-receive frequency response, $H_{\text{tx}}(\omega)$ denotes the transmit frequency response, $h_{\text{tx}}(t)$ is the time-domain transmit impulse response, and $\mathfrak{F}\{\cdot\}$ denotes the Fourier transform.

Transmit sensitivity

In order to fully characterize the CMUT, the transmit sensitivity is measured in the hydrophone set-up for various values of the sine burst frequency and bias voltages. The sine burst frequency is swept from 5 MHz to 25 MHz in steps of 0.5 MHz, the bias voltage ranges from -170 V to 0 V in steps of 5 V, and the peak-to-peak driving AC voltage is kept constant at 58 V. The acoustical characterization is performed in one measurement block with a 2.1 s delay between each measurement. The acoustic output is measured with the calibrated needle hydrophone located at a distance of 9 mm on the central axis of the CMUT array. The voltage signal received on the hydrophone is converted into output pressure, and corrected for the diffraction loss for the described geometry and excitation sine burst frequency using the Field II simulation program^{79,93} and neglecting any nonlinear propagation effects. The correction factor is calculated from the simulation as a ratio of the average peak-to-peak pressure across the transducer's surface to the average peak-to-peak pressure across the hydrophones's surface at the given location. The transmit sensitivity is calculated

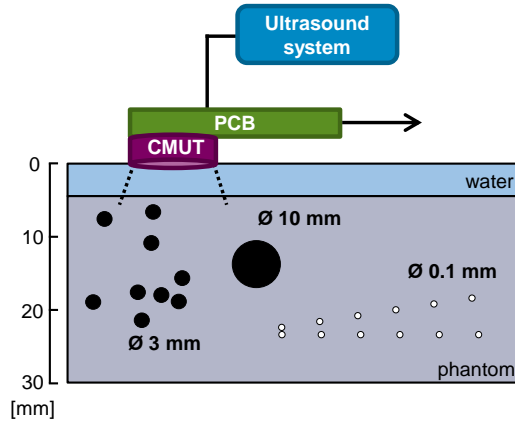


Figure 3.6: Schematic of the imaging set-up.

as the peak-to-peak pressure output divided by the peak-to-peak amplitude of the excitation AC voltage.

Reliability

High electric field up to $8 \cdot 10^6$ V/cm inside the collapse-mode CMUT and the charging effects of the dielectric materials can adversely affect CMUT reliability. To measure the reliability the CMUT is biased at -110 V and excited with 2 cycles of a unipolar 10 MHz pulse with an edge time of 20 ns and a driving voltage of -60 V. The pulse repetition frequency is 100 kHz. The acoustic output is recorded every minute for a period of 25 hours with a calibrated needle hydrophone located at a distance of 3 mm on the central axis of the CMUT array. In total $9 \cdot 10^9$ 2-cycle pulses are fired during the period of 25 hours.

Imaging set-up

To demonstrate the multi-frequency imaging capability of the collapse-mode CMUT array at its early stage of development a simple imaging set-up is designed. The CMUT mounted on a PCB is placed on top of a tissue-mimicking phantom (CIRS 050, Norfolk, Virginia, USA) and linearly moved with a motor across the phantom at a constant speed of approximately 10 mm s^{-1} as depicted in Fig. 3.6. The imaged part of the phantom contains nine non-scattering balls of 3 mm in diameter, one non-scattering rod having a diameter of 10 mm, and twelve 0.1 mm nylon wires. The CMUT active area is 2 mm which is about $\frac{1}{5}$ of the diameter of the non-scattering rod. Water is used as an acoustic matching medium between the CMUT and the phantom. All elements of the CMUT array are connected to a single channel of the custom ultrasound imaging system.

The system is capable of driving the CMUT with an arbitrary pulse defined by a 5 ns time resolution and with a maximum driving peak-to-peak voltage

level of 36 V. The analogue-to-digital convertor sampling time is 5 ns and the maximal TGC (time-gain control) value is 76 dB. In transmission all CMUT plates, being connected in parallel to a single transmit-receive channel, are excited at the same time at a pulse repetition frequency of 1 kHz. The combined echo signal from all CMUT cells is received, compensated for attenuation by a fixed TGC curve, 4 times averaged and stored in local memory for processing and display. As the CMUT is moved across the phantom, the envelope of the received echo is logarithmically compressed and converted to grayscale. Multiple envelopes displayed next to each other result in a B-mode image of the phantom.

Typical images are recorded at three different bias voltage settings and driving pulse widths. The bias voltage for a desired pulse width is chosen on the basis of the variable bias transmit sensitivity curve measured in the hydrophone set-up (Fig. 3.10(a)). The actual center frequency of the generated acoustic pulse is measured in the same pulse-echo set-up as described above. Recorded images are characterized by signal-to-noise ratio (SNR) calculated as

$$\text{SNR} = 20 \times \log_{10} \left(\frac{\mu_o}{\sigma_i} \right), \quad (3.3)$$

where μ_o is the mean of signal outside the anechoic region and σ_i is the standard deviation of signal inside the anechoic region.

3.3 Results

Acoustic characterizaton

Figure 3.7 shows impulse responses measured at three different bias voltages in pulse-echo and hydrophone set-ups together with their corresponding frequency spectra. The applied bias voltage shifts the total bandwidth of the CMUT towards the lower 9 MHz or higher 15 MHz center frequency. Figure 3.7(c) further shows that the transmit-receive and the squared transmit frequency impulse responses at the corresponding bias voltages are similar indicating reciprocity of the device. The complete scan of the frequency impulse responses as a function of bias voltage is shown in Fig. 3.8. The transmit-receive and squared transmit responses are almost identical. Analyzing the lower and upper bounds of the frequency responses we find $F_L = 7.9$ MHz and $F_U = 15.4$ MHz in the pulse-echo measurement resulting in a two-way maximum bandwidth achievable with variable bias voltage $\Delta_F = 7.5$ MHz. In the hydrophone measurement these numbers are similar, yielding $F_L = 7.6$ MHz, $F_U = 15.8$ MHz, and $\Delta_F = 8.2$ MHz for the transmit-only.

Figure 3.9(a) summarizes the transmit-receive center frequency and bandwidth for all applied bias voltages. It shows that the center frequency changes with bias voltage: range in center frequency is 8.7 MHz to 15.3 MHz and range in bandwidth is 37 % – 49 % at bias voltages of –50 V to –170 V, measured in transmit-receive. The transmit-only measurement results in similar numbers.

The maximum transmit-receive sensitivity is observed at an applied bias voltage of –130 V, at which the CMUT resonates at center frequency of 13.1 MHz as

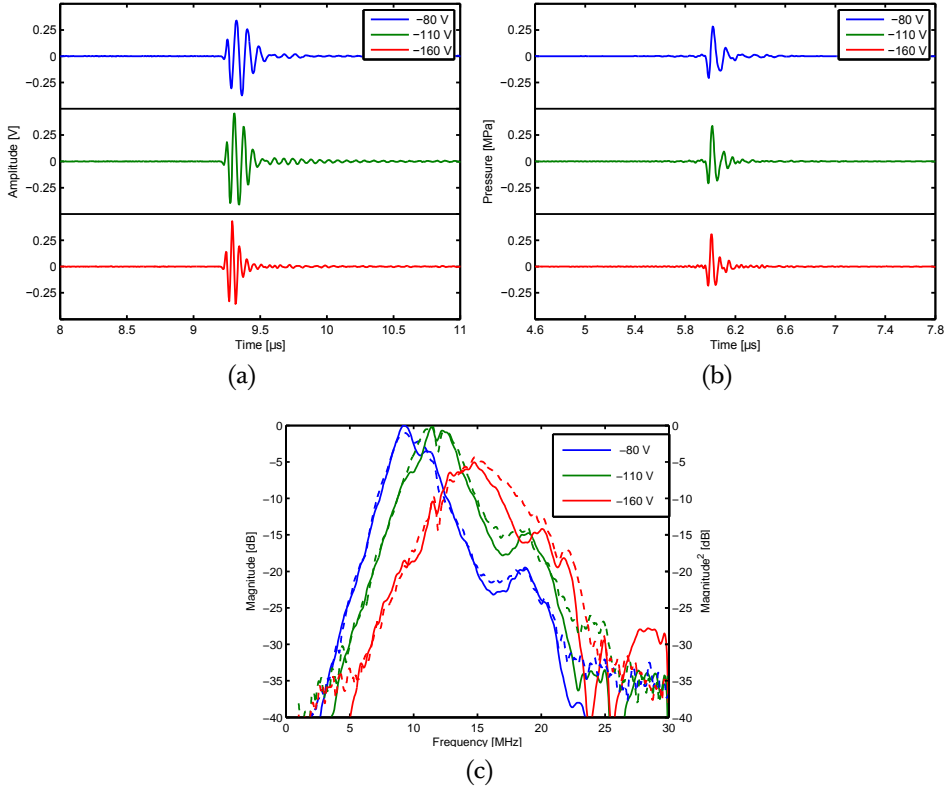


Figure 3.7: Transmit-receive (a) and transmit (b) waveforms at different bias voltages. Corresponding amplitude spectra (c) of the transmit-receive (dashed, left y-axis) and transmit waveforms (solid, right y-axis).

shown in Fig. 3.9(b). The sensitivity decreases as the bias voltage approaches the collapse voltage, resulting in a more than 6 dB lower response at the frequencies below 8.7 MHz. The transmit-receive pulse length in response to a single-impulse excitation ranges from 0.24 μs to 0.49 μs .

Figure 3.10(a) depicts the transmit sensitivity as a function of the bias voltage when driving the CMUT with a 10-cycle sine burst at frequencies ranging from 5 MHz – 25 MHz. The horizontal axis shows the bias voltage, the vertical axis shows the frequency and the color bar represents the measured transmit sensitivity. The CMUT device exhibits the highest transmit sensitivity at a sine burst frequency of 9.0 MHz with an applied bias voltage of -105 V. At a larger negative bias, the transmit sensitivity drops. The relationship between the driving frequency and the optimal bias voltage setting is shown in the same Fig. 3.10(a) as a white curve. Figure 3.10(b) illustrates the frequency tunability that can be achieved by varying the bias voltage, compared to a few single-voltage response curves. The peak transmit sensitivity is plotted as a function of the sine burst frequency for multiple fixed bias voltages as well as for vari-

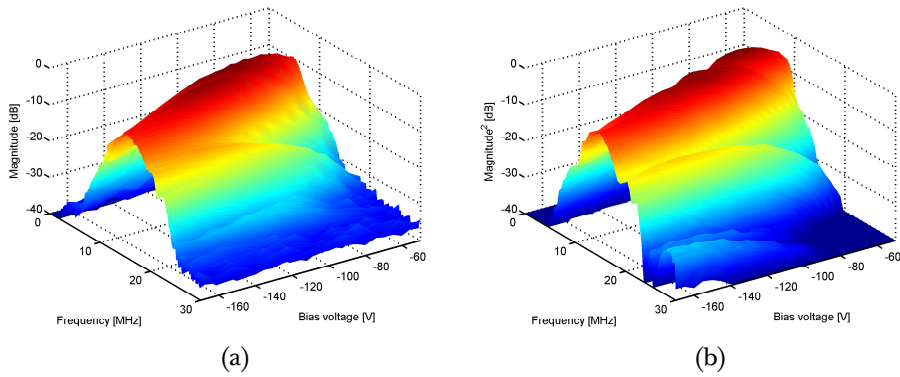


Figure 3.8: Transmit-receive (a) and transmit (b) frequency impulse responses as a function of the bias voltage.

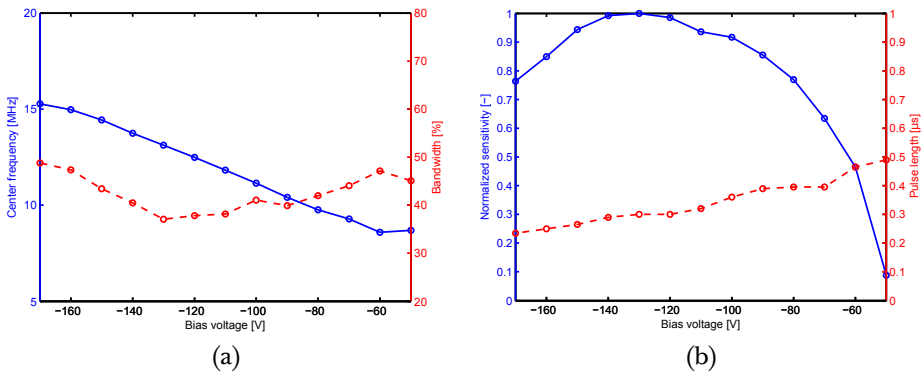


Figure 3.9: (a) center frequency (solid) and bandwidth (dashed), (b) normalized sensitivity (solid) and pulse length (dashed) measured at different bias voltages in transmit-receive.

able negative bias voltage. It can be seen from the graph that the bias voltage of -80 V gives an increase in transmit sensitivity up to 30 % at the frequencies lower than 7.5 MHz, whereas the bias voltage of -160 V boosts the frequency response above 12.5 MHz up to 36 % as compared to the frequency response at the bias voltage of -110 V. The maximum transmit sensitivity is 52 kPa V^{-1} . The transmit sensitivity changes with sine burst frequency: the -3 dB transmit range is 6.7 MHz to 15.5 MHz at bias voltages of -90 V to -165 V, respectively.

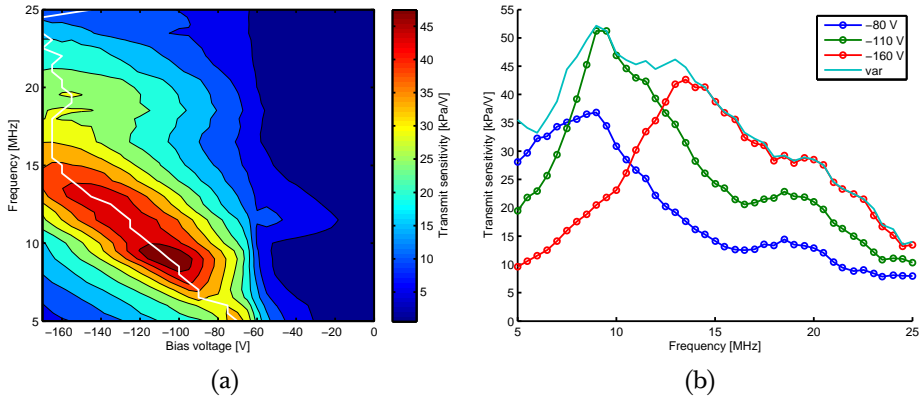


Figure 3.10: Typical transmit sensitivity measured at fixed AC voltage of 58 V (color map) overlaid with a peak transmit sensitivity at every sine burst frequency (white line) (a). Transmit sensitivity as a function of sine burst frequency at fixed and variable bias voltages (b).

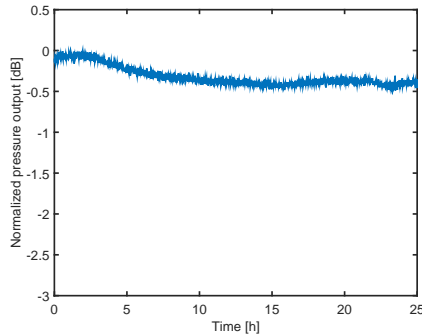


Figure 3.11: Reliability measurement results of the CMUT array biased at -110 V and excited with 2 unipolar pulses (-60 V, 10 MHz) at a pulse repetition frequency of 100 kHz. The logarithmic scale is normalized to 2.6 MPa peak-to-peak pressure.

Reliability

Figure 3.11 shows the reliability results of the CMUT array biased at -110 V and excited with 2 unipolar pulses (-60 V, 10 MHz) at a pulse repetition frequency of 100 kHz. The decrease in the acoustic output over the period of 25 hours was less than 0.5 dB, which is not expected to adversely affect the imaging performance.

Imaging

Three typical images are acquired at different frequencies using the imaging set-up. The pulse width of the bipolar single cycle driving pulse is matched to the bias voltage for optimum response. The matching is based on the peak transmit sensitivity curve shown in Fig. 3.10(a). Table 3.1 lists these parameters, together with center frequency of the resulting acoustic echo and measured SNR.

Table 3.1: Driving settings, acoustic frequency, and SNR.

	Setting I	Setting II	Setting III	Units
Bias voltage	-80	-110	-160	V
Driving pulse width	80	50	30	ns
Acoustic frequency	8.2	11.3	15.1	MHz
SNR	58	61	12	dB

Figure 3.12 shows images acquired at acoustic frequency of 8.2 MHz, 11.3 MHz and 15.1 MHz. The CMUT is moved linearly over the surface of the phantom. A mismatch in acoustic impedance of the phantom covering membrane and the background material causes multiple reverberations observed as bright parallel lines. The distance between the CMUT and the (not completely flat) surface of the phantom is about 2.5 mm – 5.0 mm. Different imaging frequencies result in varying axial resolution, observed as granularity of the speckle and sharpness of the non-scattering rod's edges. Frequency-dependent attenuation and CMUT sensitivity results in varying penetration depth for the images acquired at different frequencies. As an example, wire targets positioned at a depth of 20 mm – 25 mm are observed in Fig. 3.12(a) but are not visible in Fig. 3.12(b),(c).

3.4 Discussion

This paper focuses on the frequency tunability of a collapse-mode CMUT. We show that the center frequency of the impulse response can be tuned in a range of 8.7 MHz – 15.3 MHz with the maximum transmit sensitivity of 52 kPa V⁻¹. The three typical B-mode images presented in this study show the CMUT's multi-frequency imaging capability (Fig. 3.12). Although the granularity and sharpness of the large 10-mm non-scattering rod in the obtained B-mode images show an increase in resolution with increased imaging frequency, the 3-mm non-scattering balls are difficult to see at the high frequency of 15.1 MHz. This is due to an increased attenuation (0.7 dB cm⁻¹ MHz⁻¹) and lower signal-to-noise ratio (e.g. SNR = 12 dB for 15.1 MHz and SNR = 61 dB for 11.3 MHz).

The impulse responses in Fig. 3.7(a),(b) show similar characteristics, including a tail caused by ringing in the silicon substrate. The amplitude of the tail is below -20 dB of the waveform maximum and therefore does not affect the measured pulse length which ranges from 0.24 μs – 0.49 μs (Fig. 3.9). If needed, the silicon substrate ringing can be suppressed by addition of an acoustically-matched and highly attenuating backing layer or by thinning down the silicon

substrate to shift its resonance frequency out of the CMUT bandwidth. The thinning approach is however practically feasible up to the thickness of about 400 μm , because a thinner wafer lacks the robustness to support the moving CMUT plate. The observed substrate resonance causes a dip in the frequency spectra at about 12 MHz (Fig. 3.7(c)). At this frequency the thickness of the silicon substrate (670 μm) corresponds to one wavelength of the acoustic wave in silicon ($c = 8433 \text{ m s}^{-1}$). The peak at about 19 MHz is caused by resonance of the acoustic wave in the 40- μm thick silicone-like passivation layer, which has an acoustic impedance of about 1.1 MRayl resulting in an amplitude reflection coefficient of 0.15. Applying a passivation layer which better matches the acoustic impedance of water is subject to ongoing research. The subtle waves in the time signals between 5.8 μs and 5.9 μs in Fig. 3.7(b) are caused by discontinuity in the hydrophone calibration data curve at 30 MHz.

In this study, we show the CMUT frequency tunability in both transmit-receive (pulse-echo) and transmit-only (hydrophone). Performing these complementary measurements allows testing of the hypothesis about the transmit and receive reciprocity of the CMUT. We observe that the CMUT is a reciprocal device as shown in Fig. 3.7(c), suggesting that the same bias voltage can be used for transmit and receive at the given operating frequency. The CMUT's reciprocity holds for our set-up, because the impedance of the transmitter, receiver, and the cable are matched to 50 Ω and the components (including CMUT) are linear. The cable impedance is an order of magnitude lower as compared to the impedance of the CMUT (about 800 Ω), therefore we expect neither the loading conditions nor the parasitic capacitance to hamper the reciprocity. Though in transmit mode, the CMUT is driven with a rather large voltage (e.g. 20 V) as compared to the received signals (order of millivolts), measurements in a different study have shown that the device remains linear up to the voltage of 60 V. Therefore, the reciprocity theorem is not hampered by the different signal amplitudes.

The reliability measurement shows a less than 0.5 dB decrease in the acoustic output during the period of 25 hours at a pulse repetition frequency of 100 Hz. No adverse effects of dielectric charging or CMUT cell damage were observed. Such a reliability is sufficient for a single use devices, e.g. catheters, and is comparable to the reliability of collapse-mode CMUTs fabricated with the wafer-bonding technique published earlier in the literature⁸⁶.

Although the measured fractional bandwidth of around 43 % is a low value for CMUT compared to the 100 % presented in literature, our frequency-tunable CMUT exhibits 30 % higher maximum transmit sensitivity (52 kPa/V compared to 40 kPa V⁻¹)⁸⁶, demonstrating the trade-off in CMUT design between sensitivity and the achievable instantaneous bandwidth. We expect that by applying a matched backing and a thinner passivation layer to the CMUT, we can improve the fractional bandwidth^{94,95} and extend the frequency tunability bounds, which is the goal of on-going research. The -6 dB upper frequency bound in the spectra of the 20-ns driving pulse is at 21 MHz, which is higher than the measured maximum center frequency of 15.5 MHz. Therefore compensation for the driving pulse in the impulse response measurement would

have only a minor influence on the measured bandwidth.

The acoustic characterization of the CMUT in this study is done with both an impulse and a sine burst. While the former measurement reveals a frequency at which the CMUT „likes to resonate“ (transient response), the latter one indicates a resonance frequency range to which the CMUT „can be forced to“ (steady-state). Impulse-based characterization is important for high resolution imaging whereas the burst is relevant for Doppler or therapeutic ultrasound. We observe that by driving the CMUT with a sine-burst the frequency range extends to 6.7 MHz – 15.5 MHz (Fig. 3.10(b)).

Although there have been CMUTs published in literature which are capable of both conventional and collapse mode operation^{54,90}, our device, being optimized for (deep-)collapse mode operation⁷³, generates barely any pressure output when the CMUT is biased below the collapse voltage as can be seen in Fig. 3.10(a).

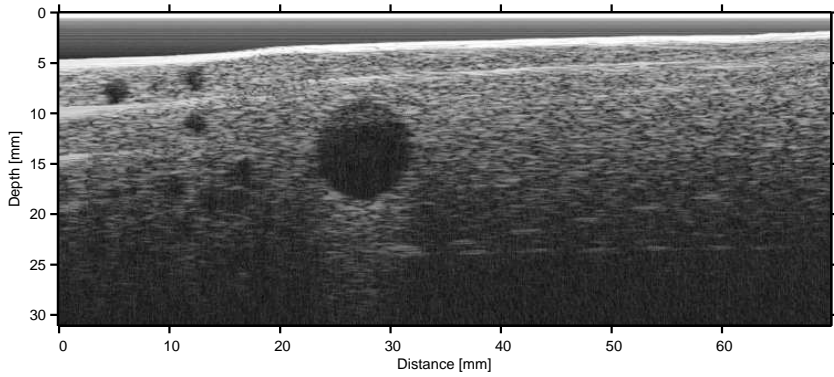
The experimental work presented in this study is done on a single-element CMUT. Further measurements have to be carried out to investigate variability in the frequency tunability of identical CMUT designs. The simple B-mode imaging generation of images at an early stage of CMUT development without any multi-wire bonding or multiple channel signal acquisition. In the next step, we plan to generate B-mode images at multiple frequencies with a frequency-tunable CMUT array and to quantify the imaging performance extensively.

3.5 Conclusion

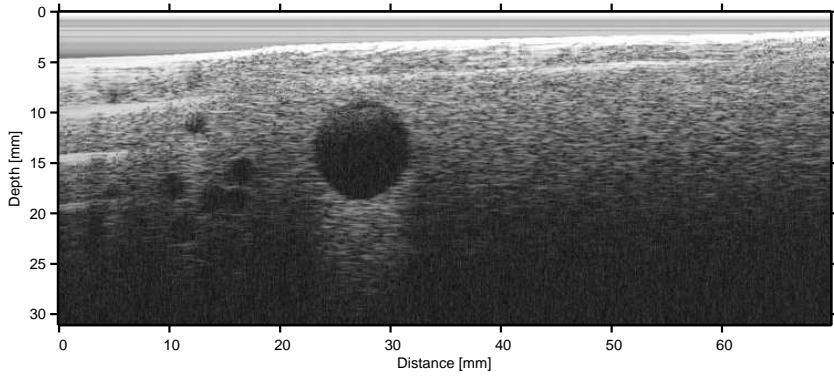
This paper investigates the frequency tunability of CMUT designed for ICE imaging. We show that the center frequency can be controlled between 8.7 MHz and 15.3 MHz of a CMUT transducer working in collapse mode. The frequency tunability, quantified as the maximum bandwidth accessible with variable bias voltage is measured to be 7.5 MHz. A transmit sensitivity up to 52 kPa V⁻¹ is achieved. The reciprocity measurements of a collapse-mode CMUT indicates that the same bias voltage can be used in transmit and receive for a given operating frequency. The CMUT does not show any reliability issues during continuous operation for 25 hours at a pulse repetition frequency of 100 kHz, bias voltage of –110 V, and excitation amplitude of 60 V. Further, mechanically-scanned B-mode imaging is performed on a phantom at 8.2 MHz, 11.3 MHz, and 15.1 MHz as first proof of principle of multi-frequency imaging with collapse-mode CMUT. Multi-frequency imaging definitively represents an attractive opportunity for frequency-tunable collapse-mode CMUTs.

Acknowledgments

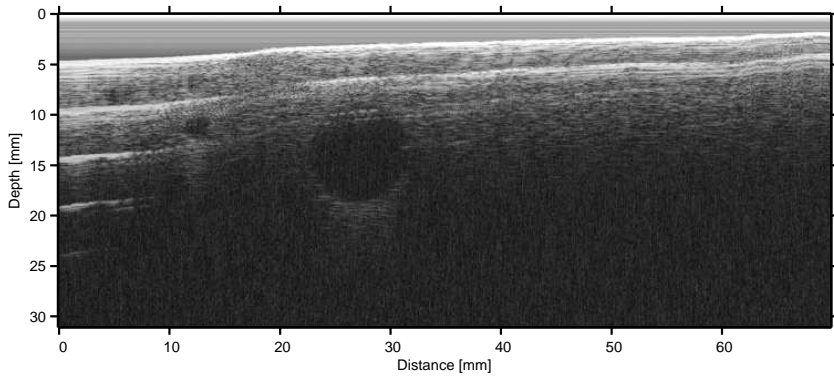
Authors would like to thank to Peter Dirksen and Jeannet van Rens for designing the CMUT samples and providing valuable insights. We thank to Alfons Groenland for fabricating the CMUT used in this study. This research is supported by European Union project OILTEBIA (grant no. 317526).



(a)



(b)



(c)

Figure 3.12: Ultrasound images acquired at the driving pulse width and bias voltage of 80 ns and -80 V (a), 50 ns and -110 V (b), 30 ns and -160 V (c). Each image shows dynamic range of 40 dB.

Imaging Performance of Frequency-Tunable CMUT Array

This chapter has been submitted for publication as:

Martin Pekař, Nenad Mihajlović, Harm Belt, Alexander F. Kolen, Jeanet van Rens, Frank Budzelaar, Bas Jacobs, Johan G. Bosch, Hendrik J. Vos, Debbie Rem-Bronneberg, Gijs van Soest, and Antonius F. W. van der Steen, Imaging Performance of Frequency-Tunable Collapse-Mode Capacitive Micromachined Ultrasonic Transducer Array, *Ultrasonics*.

Abstract

Commercially available intracardiac echo (ICE) catheters face a trade-off between viewing depth and resolution. Frequency-tunable ICE probes would offer the versatility of choice between high penetration or high resolution imaging within a single device. In this study, we report the acoustical characterization and quantitative imaging performance of a 1-D capacitive micromachined ultrasonic transducer (CMUT) array for forward-looking ICE. The array has 32 imaging elements, 63.6 μm pitch, active aperture of 9 Fr, and is integrated with custom front-end electronics in a rigid metal tube housing. The CMUT array is operated in collapse mode at bias voltages up to three times higher than the collapse voltage. Frequency tunability is quantified as the maximum bandwidth accessible with variable bias voltage. By setting the bias voltage the frequency of operation can be tuned between 8 MHz and 20 MHz. We evaluate the resolution and penetration depth in a static wire and a tissue-mimicking phantom as a function of bias voltage, frequency, and a number of transmit pulse cycles. Based on this characterization, optimal imaging modes for penetration, high-resolution, and generic views are identified.

4.1 Introduction

Background and Motivation

Cardiovascular disease is the leading global cause of death, accounting for more than 17 million deaths per year, which is expected to grow to more than 24 million by 2030. The costs of cardiovascular diseases including expenditures and lost productivity are more than \$316 billion¹. Minimally-invasive procedures have proven to be effective in the patient outcome while reducing the costs and complexity of the cardiac interventions. The minimally-invasive treatment requires a high-quality real-time imaging capable of accurately locating intracardiac regions of interest or prosthetic devices. Intracardiac echocardiography (ICE) has proven valuable in sophisticated anatomic interventions, including transseptal puncture, device closure of atrial septal defects, and pulmonary vein ablations²⁵. The advantage of ICE imaging over conventionally-used transesophageal imaging is that the patient does not have to be under general anesthesia, reducing the costs and the procedure time. Currently, a number of ICE catheters are available to interventionalists for intracardiac imaging²⁵. These 8-Fr to 10-Fr (2.6 mm – 3.3 mm) thick steerable catheters have a rigid tip which includes a side-looking ultrasound imaging array having a transducer surface of about 2 mm × 13 mm. The ICE catheter is typically introduced via a femoral vein into the right heart under fluoroscopic guidance. ICE imaging is initiated after the catheter is positioned in the mid-right atrium. The imaging tip can be further steered or rotated to get the desired view. ICE is standardly used in this position to guide transseptal punctures. High-resolution imaging is, however, required for other procedures, e.g. of mitral valve sizing, thrombus detection or closure device placement in the left-atrial appendage. In electrophysiology, it is desired to localize the ablation catheter, determine catheter contact and measure features in the left heart (e.g. wall thickness, lesion formation). For these procedures, the current ICE catheter has low resolution when imaging from the right heart. Although it is possible to bring the ICE catheter to the left side of the heart for improved lateral resolution, the long rigid tip and the side-looking geometry of the commercially available ICE catheters limit the view in the confined space of the left atrium.

Our ultimate goal is a versatile forward-looking ICE catheter which can be maneuvered to the left heart to produce both a high-level penetration image for overview and a close-range detailed anatomic image of the structures of interest by tuning its operation frequency on the fly to the specific task. A 5-MHz imaging mode in combination will provide coarse orientation and navigation in the heart (zoom-out). Considering 40 dB signal-to-noise ratio and 0.5 dB cm⁻¹ MHz⁻¹ attenuation in heart tissue and 0.25 dB cm⁻¹ MHz⁻¹ attenuation in blood, it is expected to achieve penetration depth of at least 8 cm in tissue or 16 cm in blood⁹⁶. The forward-looking nature of the device will allow intuitive navigation towards the specific feature of interest. Subsequent switching to a 15-MHz imaging mode will provide detailed close-up imaging (zoom-in).

We have developed a 1-D CMUT (Capacitive Micromachined Ultrasonic

Transducer) array operated in collapse mode, which allows for the frequency tuning^{65,75,97}. The array is mounted at the tip of a probe prototype, of which the characterization and frequency-tunable imaging is presented in this paper.

Collapse-mode CMUT

A CMUT consists of a top-electrode plate (commonly referred to as „membrane“) and a cavity which incorporates an insulated bottom electrode⁹⁸. Application or detection of an AC voltage enables transmission and reception of ultrasound. In collapse mode^{53,90}, the membrane is biased with a DC voltage high enough to pull the membrane in onto the bottom of the cavity. This regime offers greatly enhanced linearity⁶¹, sensitivity⁸⁶ and the frequency tuning^{58,65,75}.

Current forward-looking ICE catheters with CMUT technology

The first reported forward-looking intracardiac array based on conventional-mode CMUT had a center frequency of 9 MHz^{99,100}. Initial images acquired with a Vivid-i GE system, showed limited penetration depth of 1.5 cm in an *ex vivo* rabbit heart. Monolithic fabrication of CMUTs on top of an application specific integrated circuit (ASIC) allowed for a compact design which enabled integration into a 9-Fr catheter shaft¹⁰¹. This was used to obtain the first *in vivo* images of forward-looking CMUT ICE in 2012²⁴. Real-time images acquired with a GE Vivid 7 system showed improved penetration depth up to 3 cm in a porcine heart, demonstrating promising clinical usability of a forward-looking CMUT ICE, however, without the option of tuning the imaging frequency.

Our design utilizes a different CMUT operated solely in collapse mode, of which the details can be found in earlier papers^{65,73}. The developed CMUT has an extra feature that allows changing its operating frequency over a continuous range rather than switching between two discrete frequencies in conventional and collapse mode as shown earlier by Huang et al.⁹⁷. This continuous frequency tunability is investigated for forward-looking ICE imaging to meet the clinical requirement of having the possibility of high penetration or high resolution (zoom-in and zoom-out capability).

Scope of the study

This study provides a comprehensive and quantitative characterization of frequency response, sensitivity and imaging performance in controlled settings. A CMUT phased array is integrated with custom front-end electronics in a rigid metal tube housing and connected to a research ultrasound imaging system. The CMUT is operated at bias voltages up to three times higher than the collapse voltage. Resolution and penetration depth in a static wire and tissue-mimicking phantom is evaluated as a function of bias voltage, frequency, and number of transmit pulse cycles. Based on the characterization, penetration, high-resolution, and generic modes are derived and its imaging performance is demonstrated.

4.2 Materials and Methods

Transducer

The transducer array elements comprises of $60\text{-}\mu\text{m}$ CMUT cells⁸⁶, which are fabricated using the standard sacrificial release process described earlier^{72,73}. The cells enter collapse mode at a voltage of around -65 V . Columns of CMUT cells form a single phased imaging elements spaced at a pitch of $63.6\text{ }\mu\text{m}$ as shown in Fig. 4.1. The total array consists of 32 imaging elements, of which the first and the last seven elements are progressively shorter as compared to the middle elements to fit within the circular area of 9 Fr. The whole array is 12 Fr compliant including the wirebonds to a flexible PCB that will be in the future work rolled around the circular CMUT.

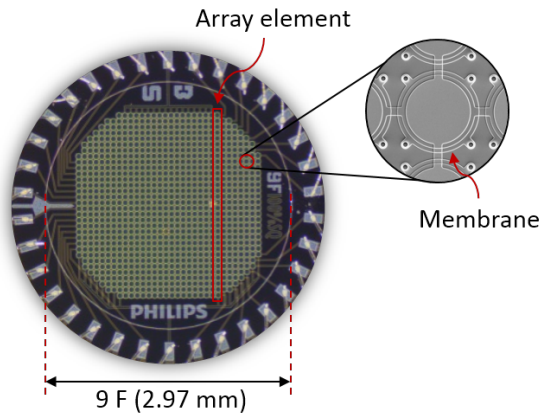


Figure 4.1: Photograph of the fabricated CMUT array.

ASIC

Individual imaging elements have a capacitance of approximately 5 pF , which is two orders of magnitudes smaller than the cable capacitance (about 250 pF). A direct connection of the transducer elements to an ultrasound imaging system via a 1.5-m long catheter shaft would result in severe signal degradation and thus in poor imaging performance. Therefore two custom-designed ASICs integrate front-end electronics closely with the CMUT at the tip of the catheter. Each of the two ASICs measures $2.0\text{ mm} \times 1.2\text{ mm} \times 0.4\text{ mm}$ and has 16 channels comprising of up to -60-V unipolar pulsers, transmit and receive switches, 27 dB amplifiers, and line drivers.

Assembly

The 32 transducer elements connect to two 16-channel ASICs via a flexible PCB as shown in Figure 4.2(a). The whole assembly is fitted into a 26-cm long metal

tube housing having a diameter of 11 mm in the current probe prototype. Figure 4.2(b) depicts the manufactured probe. To provide electrical insulation to the exposed connections and to protect it from corrosion the whole probe is coated with a 14- μm thick layer made from a silicone-like material.

Electronic interface

Bias voltage, ASIC control signals, power and data channels are connected via a 1.8-m long cable and a connector (JAE312, JAE, Tokyo, Japan) mounted on the PCB. The proximal end of the cable connects to an electronic board interfacing the imaging system.

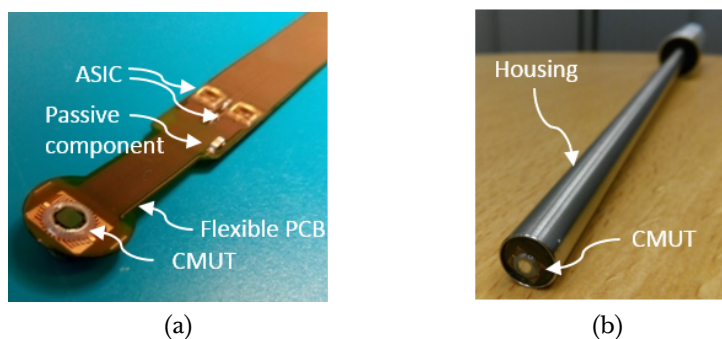


Figure 4.2: Photograph of the CMUT array mounted on a flexible printed circuit board (a) integrated in a probe prototype (b).

Imaging system

A Verasonics Vantage imaging system (Kirkland, WA, USA) is used to generate control signals and to capture ultrasound sensor data at different transmit and bias voltage parameters.

Conventional phased array imaging algorithm¹⁰² steers 106 beams in a 90° sector with 0.85° angular resolution. The transmitted beams are unfocused because the depth of view goes beyond the near-field (about 7 mm) up to a depth of 100 mm. No image improvement would result by focusing beyond the near-field. After beamforming the acquired sensor data a resulting ultrasound image is displayed on the machine.

Acoustic characterization

The CMUT probe is immersed in a water tank and carefully aligned towards a flat plate reflector positioned in the far field at a distance of 40 mm. The alignment is done based on the arrival time difference of the echoes from the most outer elements and based on the echo amplitude for the lateral and elevational axis, respectively. The whole array is driven with a unipolar 25-ns –40-V

pulse at bias voltage of -70 V to -160 V in steps of -5 V applied to the bottom electrode of the CMUT. Note that the negative bias voltage is additive to the ASIC's (unipolar) pulse amplitude resulting in maximum pressure output. Maximum voltage to the CMUT is limited to about -200 V (the breakdown voltage of the dielectric layer).

Spectra of the received signals are analysed for the frequency response of the CMUT array element at different bias voltages. The center frequency, bandwidth, and frequency tunability are calculated as a function of the bias voltage. The frequency tunability is quantified as the maximum bandwidth accessible with variable bias voltage

$$\Delta_F = F_U - F_L, \quad (4.1)$$

where F_L and F_U are the -6 dB upper and lower band edges evaluated in frequency spectra recorded over the full range of bias voltages.

Identifying imaging modes

B-mode sector scans of a tungsten wire having a diameter of $75 \mu\text{m}$ and a tissue-mimicking phantom (Model 465, Dansk Fantom Service, Frederikssund, Denmark) having an attenuation of $0.5 \text{ dB cm}^{-1} \text{ MHz}^{-1}$ in the range from 1 MHz to 20 MHz are utilized to quantify axial and lateral resolution and penetration depth as a function of bias voltage, frequency, and a number of transmit pulse cycles. The resolution is estimated as the full-width half-maximum (FWHM) of the point-spread function. The penetration depth is chosen to be estimated as the depth at which the mean signal amplitude differs less than 1 dB from the mean noise amplitude, where the means are calculated along the lateral dimension. In order to avoid influence of the frequency dependency of attenuation on the penetration depth estimation the received data is filtered prior to the beamforming by 51-coefficient linear phase finite-impulse response filter having a bandwidth of 10% relative to the transmit pulse frequency. This narrow band filter allows investigating the effect of bias voltage on the penetration depth. The other motivation for using such narrow band filter is to „force“ the intended frequency, irrespective of resonances in the probe which shift the actual frequency content of the transmit pulse to resonance frequency of the CMUT.

The transmit pulse frequency is swept from 5 MHz to 25 MHz in steps of about 2 MHz, the number of transmit pulse cycles is set to either 1 , 2 , or 3 , the bias voltage ranges from -70 V to -160 V in steps of -10 V. To quantify the imaging performance 100 B-mode images are recorded for each of the transmit pulse cycle setting. The acquired images are automatically analyzed. The resolution and penetration depth are displayed as a function of bias voltage, frequency, and a number of transmit pulse cycles.

A tissue-mimicking phantom (CIRS050, CIRS, Norfolk, VA, USA) containing $100 \mu\text{m}$ thick nylon targets and an anechoic target structure of 5-mm in diameter are used to demonstrate the CMUT probe's imaging performance. The images of the anechoic target are characterized by the image contrast¹⁰³

$$C = 20 \times \log_{10} \left(\frac{\mu_i}{\mu_o} \right), \quad (4.2)$$

where μ_i is the mean signal inside the anechoic region and μ_o is the mean signal outside the anechoic region.

4.3 Results

Pulse-echo response

Figure 4.3(a) shows the time-domain waveforms acquired with a typical imaging element in the center of the array at three example bias voltages. Higher frequency content is observed for the increasing absolute value of the bias voltages (since only negative bias voltage is used in this study, the *absolute value of the bias voltage* is hereby referred to as the *bias voltage* for readability). The pulse durations, measured between the first and the last point in the waveform at -20 dB to the envelope peak are 464 ns, 299 ns and 396 ns for the -90 V, -120 V and -160 V, respectively. Figure 4.3(b) shows the corresponding spectra at the three example bias voltages. It can be seen that the frequency response shifts towards the high frequencies with larger bias voltage. Measured frequency tunability of the CMUT as defined by Eq. 4.1 is 8 MHz – 20 MHz.

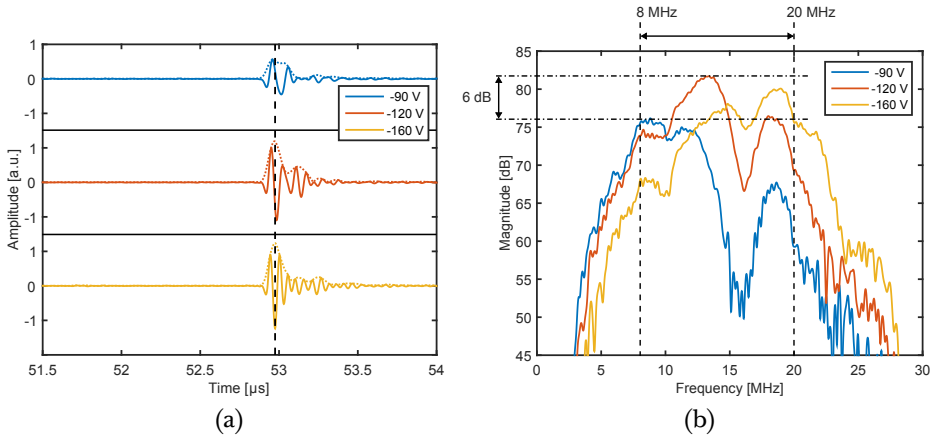


Figure 4.3: Typical envelope-detected pulse-echo (a) and frequency (b) response of the CMUT array element at three different bias voltages overlaid with frequency tunability bounds.

The measured center frequency of the CMUT array element changes from 8.6 MHz to 16.9 MHz within the range of bias voltages from -70 V to -160 V (Fig. 4.4), while the bandwidth varies from 5.9 MHz to 10 MHz. Note that the center frequency range is different from the frequency-tunability bounds

because the peak magnitude of the individual spectra acquired at different bias voltages is not the same as the peak magnitude at the variable bias voltage.

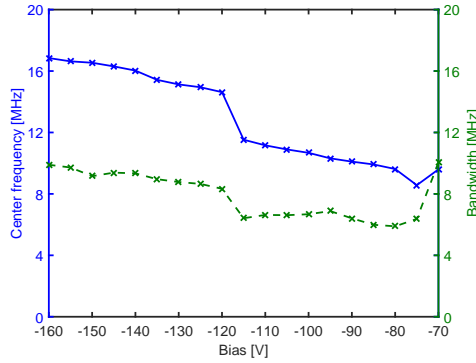


Figure 4.4: Measured center frequency (solid) and bandwidth (dashed) of the CMUT array element as a function of the applied bias voltage.

Figure 4.5 shows the uniformity of the fabricated CMUT array in terms of center frequency, bandwidth, and sensitivity (defined as peak-to-peak amplitude in arbitrary units) across a range of bias voltages. Standard deviations across the 32 array elements are below 635 kHz, below 14 % (1.1 MHz), and below 3.4 dB for the center frequency, bandwidth, and sensitivity, respectively; the outer elements show lower sensitivity because of their size tapering.

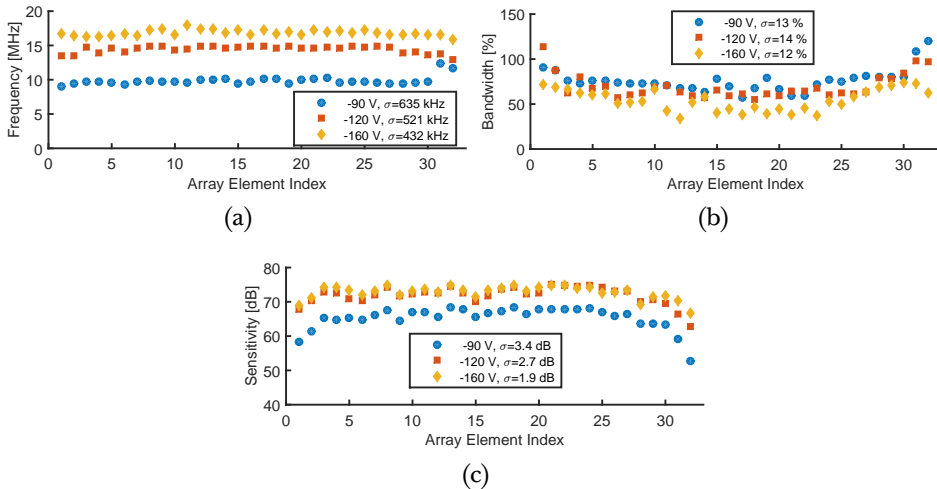


Figure 4.5: Center frequency (a), bandwidth (b), and element sensitivity (c) measured at three different bias voltages across the 32 element CMUT array. Note: due to the circular design the first and the last seven elements of the array are progressively shorter as compared to the middle elements (Fig. 4.1).

Imaging performance quantification

Figure 4.6 shows the axial and lateral resolution, and penetration depth as a function of bias voltage and the transmit pulse frequency. The center frequency of the CMUT increases approximately linearly with the bias voltage as shown in Fig. 4.4, which is in agreement with the earlier simulations⁵⁸. The resolution is a linear function of the center frequency, hence of the bias voltage too. Therefore the measured imaging performance in Figs.4.4 and 4.6 shows a linear combination of two vectors, the bias voltage vector and the resolution vector. A diagonal gradient rising from the lowest bias voltage and frequency to the highest bias voltage and frequency is to be expected. Similar trend is expected also for the penetration depth graph, because the tissue-mimicking phantom has attenuation linearly proportional to the frequency.

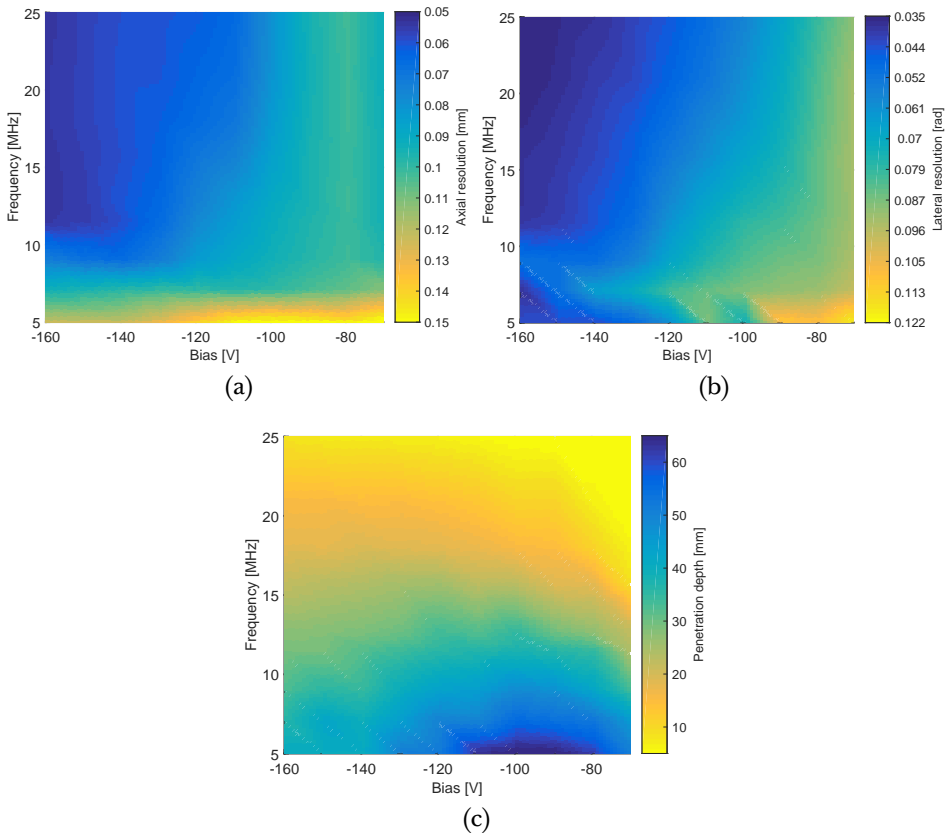


Figure 4.6: Measured axial (a) and lateral (b) resolution, and penetration depth (c) as a function of bias voltage and transmit pulse frequency (single cycle). In total 100 B-mode images were acquired to measure these imaging performance maps. The step size is -10 V for the bias voltage and about 2 MHz in the frequency.

Effect of the bias voltage on resolution and penetration depth at a fixed transmit frequency and different number of transmit pulse cycles is shown in Fig. 4.7 in comparison to the simulation. The axial and lateral resolution are simulated as

$$r_{\text{ax}} = n \frac{c}{2f}, \quad (4.3)$$

$$r_{\text{lat}} = 1.22 \frac{cR}{fD}, \quad (4.4)$$

where n is the number of transmit pulse cycles, c is the speed of sound, f is the transmit frequency, R is the range distance, D is the aperture size, and the factor of 1.22 accounts for -6 dB reduction in the beam amplitude of dual sided opening angle of the main lobe¹⁰⁴.

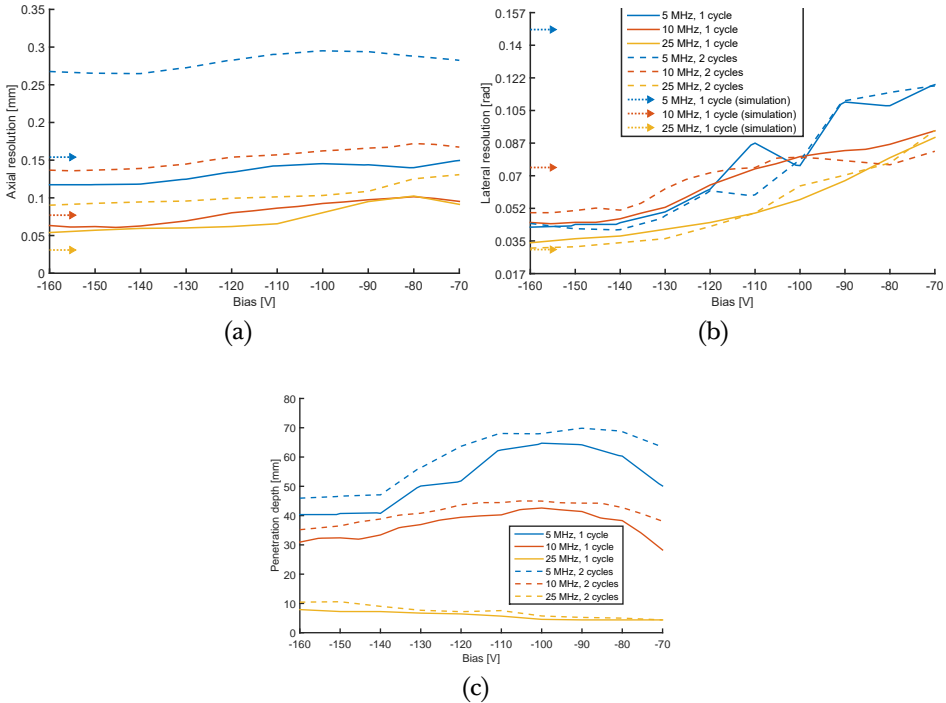


Figure 4.7: Effect of the bias voltage on axial (a) and lateral (b) resolution, and penetration depth (c) at three example transmit pulse frequencies and various number of transmit pulse cycles compared to the simulation based on Eqs. (3) and (4), which are independent of the bias voltage. Note: (a) and (b) share the same legend.

The effect of the bias voltage on the generated acoustic waveform was investigated by analyzing the mean envelope-detected echo. Figure 4.8(a) illustrates the effect of combining low transmit pulse frequency of 5 MHz with high bias voltage of -150 V compared to the echo obtained at the same frequency and

bias voltage of -90 V shown in Fig. 4.8(b). Since a single unipolar pulse is transmitted in both scenarios a single 5 MHz echo is expected. The envelope detected signal shows that this is not the case for the bias voltage of -150 V. Two echoes having a frequency higher than 5 MHz and a single 5 MHz echo are actually observed for the bias voltage of -150 V and -90 V, respectively.

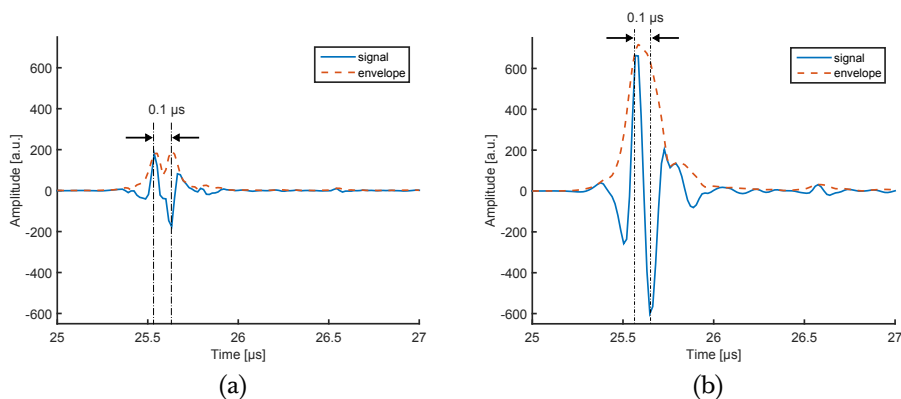


Figure 4.8: Mean envelope-detected echo from a wire target obtained at pulse frequency of 5 MHz and bias voltage of -150 V (a) compared to echo at bias voltage of -90 V (b). Note that the indicated interval of 0.1 μ s corresponds to a period of 0.2 μ s and a frequency of 5 MHz.

Identification of different imaging modes

High-resolution mode is determined as the setting which gives maximum lateral resolution and a penetration depth of at least 20 mm in tissue (arbitrary value corresponding to the typical size of the left atrial appendage³). Penetration mode corresponds to the settings that give maximal penetration at the cost of lateral resolution. Generic mode settings are calculated as a linear combination of the high-resolution and penetration mode settings, all of which are summarized in Tab. 4.1.

Table 4.1: Settings for the three imaging modes with a collapse-mode CMUT.

	Penetration	High-resolution	Generic	Units
Bias voltage	-90	-160	-120	V
Pulse frequency	5	20.8	12.5	MHz
Pulse cycles	3	1	2	–

B-mode imaging results

The preliminary 2-D B-mode images of a wire and a tissue-mimicking phantom acquired in the different imaging modes utilizing the CMUT's frequency tun-

ability are shown in Fig. 4.9 and Fig. 4.10, respectively. The low-bias voltage mode provides high penetration depth as shown in Figs. 4.9(b) and 4.10(b). Figures 4.9(d) and 4.10(d) show high resolution, which is apparent from the size of the wire target, fine granularity of the speckle, and sharpness of the cyst's edge. The latter images show reduced penetration depth due to the frequency-dependent attenuation of the tissue-mimicking phantom. Figures 4.9(c) and 4.10(c) are examples of generic mode images. The contrasts calculated according to Eq. 4.2 are -29 dB, -28 dB, and -26 dB for the penetration, generic, and resolution mode, respectively.

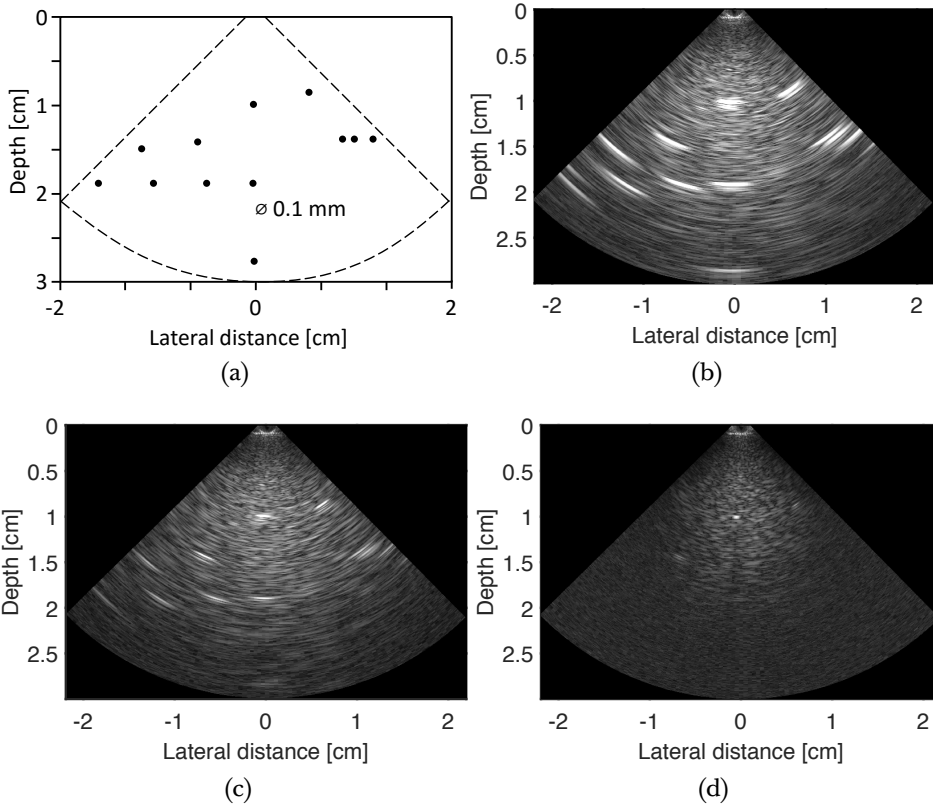


Figure 4.9: Images of the CIRS phantom containing wires (a) acquired in penetration (b), generic (c), and high-resolution (d) imaging mode. The dynamic range of the displayed images is 50 dB.

4.4 Discussion

This paper shows the frequency tunability (Eq. 4.1) of a collapse-mode CMUT array. By tuning the bias voltage the -6 dB frequency band of operation is lying between 8 MHz and 20 MHz (Fig. 4.3(b)). The advantage of CMUT's

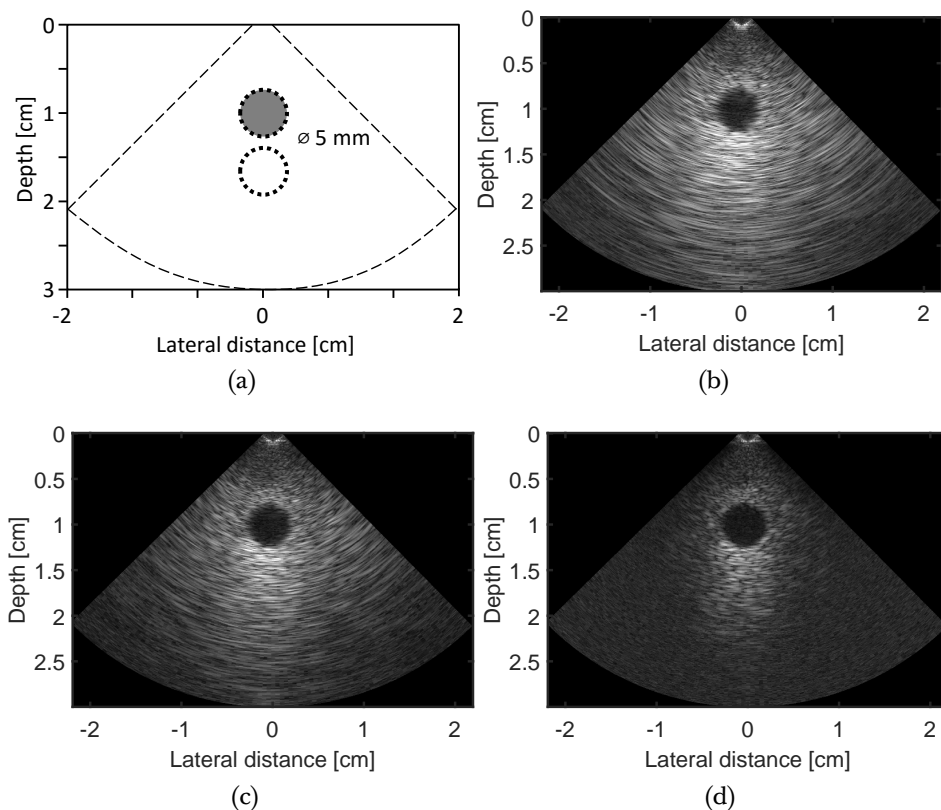


Figure 4.10: Schematic drawing of the CIRS phantom features (a) with overlaid dotted circles indicating the regions of interest used for the contrast calculation. Images of the anechoic phantom feature acquired in penetration (b), generic (c), and high-resolution (d) imaging modes. The dynamic range of the displayed images is 50 dB. The measured image contrasts are -29 dB (b), -28 dB (c), and -26 dB (d).

frequency tuning by the bias voltage is used to perform imaging at different modes. The contrast with which the wires are detected is low in the resolution mode image (e.g. most of the wires are not visible) shown in Fig. 4.9(d). This is explained by a relatively low scattering strength of the wires compared to the background material at frequencies higher than $\sim 12 \text{ MHz}$. Nevertheless, Fig. 4.10(d) shows that the image contrast that allows visualizing of the anechoic target is comparable. Therefore it can be deduced that heart valves located in a mildly attenuating blood pool could still be visualized with the technique presented in this study.

Despite its small and fixed aperture the probe shows to provide satisfactory imaging performance at a range of the driving pulse frequencies shown in Tab. 4.1. The demonstrated imaging modes offer the versatility of choice between high penetration or high resolution imaging without the need of ex-

changing the ultrasound probe, which is of crucial importance for catheter-based imaging. The functionality of the probe is comprehensive to a previously published dual-mode CMUT annular array that has been demonstrated earlier to operate at two distinguished frequencies⁹⁰.

Figure 4.7(a) suggests that the bias voltage only has a minor effect on the axial resolution, e.g. for the transmit pulse of 5 MHz it does not change by more than 12 %. This is readily explained by Fig. 4.8(a) which shows that a CMUT biased at -150 V and driven with a single long pulse of 5 MHz, reacts only on the rising and falling edges of the transmit pulse, generating two consecutive high frequency acoustic pulses. These pulses appear as a double peak in the envelope resulting in a comparable axial resolution as in the case of lower -90 V bias voltage which generates a single 5 MHz acoustic pulse as shown in Fig. 4.8(b). For the same reason Fig. 4.6(b) shows improved lateral resolution at the high bias voltages (> -120 V) and low pulse frequencies (< 7 MHz), while the axial resolution remains unaffected (Fig. 4.6(a)).

Lateral resolution is determined by the width of the beam, which for an unfocused system depends solely on the transmit frequency and the aperture width. Figure 4.7(b) shows that the measured lateral resolution does not change with the pulse length, as expected. However, the lateral resolution changes rapidly with the bias voltage because it affects the acoustic pulse frequency. Again, the measured lateral resolution approaches the simulation only at the bias voltage which supports the resonance frequency of the simulated transmit pulse, e.g. -115 V for the pulse frequency of 10 MHz. There is a discrepancy between the measurement and simulation of the lateral resolution for the 5 MHz transmit pulse. This is because the simple simulation assumes single frequency transmission whereas the actual measurement is done on a broad-band pulse. An advanced simulation which would account for the bandwidth of the transmitted pulse would provide more accurate results.

The presented CMUT array exhibits uniform frequency response across the elements at a range of bias voltages as shown in Fig. 4.5(a). The mean bandwidth varies between 76 % and 54 % for the lowest (-90 V) and the highest (-160 V) bias voltage, respectively. The higher bias voltage results in larger forces restricting the mode shapes of the membrane and thus narrowing the range of the vibrational frequencies. Standard deviation in the bandwidth across the array elements is less than 14 %. This variation is probably caused by the variation in the thickness of the applied passivation layer. The octagonal shape of the array (Fig. 4.1), which is required for the 9 Fr active aperture conformity, results in lower sensitivity of the outer elements providing an apodization that is close to what is often used in ultrasound imaging (e.g. Hanning window) as shown in Fig. 4.5(c). The measured standard deviation of the array sensitivity is less than 3.4 dB. This variation is caused namely due to the first and the last seven array elements being progressively shorter than the middle ones (Fig. 4.1).

The bandwidth of the presented probe is severely limited by the passivation layer artifacts, which facilitates undesired crosstalk between the elements (secondary echoes after $53.05 \mu\text{s}$ in Fig. 4.3(a))^{105,106} and generates a $\frac{\lambda}{4}$ resonance of

the acoustic wave (peak at about 18 MHz in Fig. 4.3(b))^{100,107}. This could be improved by applying a passivation material that closely matches the acoustic impedance of water. Design of an artifact-less passivation layer is the goal of on-going research.

The manufactured CMUT probe is a rigid stick, which can be used in emerging clinical procedures utilizing transapical access, e.g. monitoring the intramural cardiac ablations¹⁰⁸ or imaging of mitral and aortic valve¹⁰⁹. The same CMUT transducer has been integrated with the front-end electronics into a 12-Fr steerable catheter by utilizing a thin flexible PCB wirebonded and rolled around the circular CMUT. Finally, the clinical relevancy of the frequency tunability in an in-vivo animal model has been demonstrated¹¹⁰.

4.5 Conclusion

A collapse-mode CMUT array integrated with custom-designed front-end electronics is successfully tested. Phased array ultrasound imaging with a forward-looking CMUT probe prototype operated beyond collapse mode at voltages up to three times higher than the collapse voltage has been demonstrated. Imaging performance as function of bias voltage, transmit pulse frequency, and number of transmit pulse cycles is quantified, based on which penetration, high-resolution, and generic imaging modes are identified. We showed that by utilizing the concept of frequency tuning, we can generate images with different characteristics such as penetration, high resolution, or generic image quality. It is the high efficiency of collapse-mode CMUT and custom-integrated electronics that allows imaging up to 60 mm in a tissue-mimicking phantom, which is considerable, given the fact that the array has aperture smaller than 2 mm × 2 mm.

Acknowledgments

The authors would like to thank the following people for their effort and support in this study: Michel van Bruggen, Alfons Groenland, Marc Notten, Wim Weekamp, Wendy Dittmer, Nico de Jong, and René Aarnink.

This research is in part funded by the FP7 project „OILTEBIA“ (grant no. 317526) of the European Union.

Preclinical Testing of Frequency-Tunable CMUT Probes

This chapter has been published as:

Martin Pekař, Alexander F. Kolen, Harm Belt, Frank van Heesch, Nenad Mihajlović, Imo E. Hofer, Tamas Szili-Török, Hendrik J. Vos, Johan G. Bosch, Gijs van Soest, and Antonius F. W. van der Steen, Preclinical Testing of Frequency-Tunable Capacitive Micromachined Ultrasonic Transducer Probe Prototypes, *Ultrasound in Medicine & Biology*, 43, no. 9, pp. 2079 – 2085 (2017).

Abstract

In intracardiac echocardiography (ICE) it may be beneficial to generate ultrasound images acquired at multiple frequencies, having the possibility of high penetration or high resolution imaging in a single device. The objective of the presented work is to test two frequency-tunable probe prototypes in a preclinical setting: a rigid probe having a diameter of 11 mm and a new flexible and steerable 12-Fr ICE catheter. Both probes feature a forward-looking 32-element capacitive micromachined ultrasonic transducer array (aperture of $2 \times 2 \text{ mm}^2$) operated in collapse-mode, which allows for frequency-tuning in the range from 6 MHz to 18 MHz. The rigid probe prototype is tested *ex vivo* in a passive heart platform. Images of an aortic valve acquired in high-penetration (6 MHz), generic (12 MHz), and high-resolution (18 MHz) mode combine satisfying image quality and penetration depth between 2.5 cm and 10 cm. The ICE catheter prototype is tested *in vivo* using a porcine animal model. Images of an aortic valve are acquired in the three imaging modes with the ICE catheter placed in an ascending aorta at multiple depths. It was found that the combination of the forward-looking design and frequency-tuning capability allows visualizing intracardiac structures of various sizes at different distances relative to the catheter tip, providing both wide overviews and detailed close-ups.

5.1 Introduction

Cardiovascular deaths represent 31 % of all global deaths in the past few years, claiming more lives than all forms of cancer combined¹. Minimally-invasive procedures have proven to be effective in improving the patient outcome while minimizing trauma and complexity of cardiac interventions. Intracardiac echocardiography (ICE) is an established guidance tool for device closure of interatrial communications and electrophysiological ablation procedures^{111,112}. The exploitation of ICE for navigation during other cardiac interventions and, more importantly, its use as a diagnostic tool is currently limited by its imaging performance at a distance²¹ Fig. 3(c) and the restricted view it typically provides¹². Our goal is to design a steerable forward-looking catheter which can change its imaging frequency between 6 MHz and 18 MHz, allowing for high penetration or high resolution imaging within a single device. The forward-looking design will offer complementary views to the conventional side-looking ICE concept. The frequency tunability combined with the catheter maneuverability will allow for both navigation and detailed close-up imaging.

While the clinical review reports demonstrate the unmet need for a frequency-tunable forward-looking ICE catheter, only one description of a forward-looking ultrasound transducer array which can change its operating frequency⁹⁰. This design utilized a capacitive micromachined ultrasonic transducer (CMUT) ring array operated at 8 MHz and 19 MHz in conventional and collapse mode, respectively. The array could generate 3-D images of a wire phantom in oil, however, its integration in a steerable catheter shaft and its preclinical imaging capability remains to be demonstrated.

Our design utilizes a single-type CMUT operated solely in collapse-mode, which has an extra feature that allows changing its operating frequency. This behaviour is referred to as „frequency tunability“ over a continuous range of frequencies⁶⁵ as opposed to a discrete change between conventional and collapse mode. The frequency tunability is investigated in this preclinical study for forward-looking ICE imaging, addressing the requirement of having the possibility of high penetration (zoom-out) or high resolution (zoom-in).

The principal objective of the presented work is to test two frequency-tunable forward-looking probe prototypes in a preclinical setting: a rigid probe having a diameter of 11 mm and a new flexible and steerable 12-Fr catheter. The acoustic characterization of the rigid probe has been published earlier⁷⁵. The following section introduces the development of the new 12-Fr catheter. The concept of frequency tunability is first demonstrated on 2-D images of an aortic valve in a controlled *ex vivo* setting using the rigid probe. Zoom-in and zoom-out capability of the developed catheter is presented in *in vivo* imaging of the aortic valve in a live animal model.

5.2 Materials and Methods

Transducer technology

Our design utilizes a 32-element CMUT phased array operated in collapse-mode⁷³, having a 9-Fr active aperture of an octagonal shape as shown in Fig. 5.1(a). The CMUT consists of thousands of tiny capacitors (about 60 μm in diameter and 1.5 μm thick) with movable top membranes arranged in columns connected electrically in parallel. Static DC bias voltage (80 V – 160 V) is used to collapse the center area of the membrane onto the bottom of the cavity. Then AC voltage is applied to excite the free part of the membrane without releasing the center area from the bottom of the cavity. The CMUT transduces ultrasound and voltage as a result of these membrane vibrations, of which the resonance frequency increases for a high bias voltage magnitude, because the membrane stiffness and the contact radius of the collapsed portion of the membrane increases with larger deflection. The transmit pulse style and the bias voltage settings are tailored to the three imaging modes, based on initial resolution and penetration measurements on a tissue-mimicking phantom (unpublished observation).

Probe prototypes

The fabricated CMUT array is integrated with front-end electronics into two probe prototypes: a robust rigid probe having a diameter of 11 mm, and a steerable 12-Fr catheter. Both devices are equipped with an identical CMUT array and an application specific integrated circuit (ASIC) to integrate the front-end electronics closely with the CMUT at the tip of the probe. The ASIC has 16 channels, each of which comprises of a 60-V unipolar pulser, a transmit and receive switch, a 27 dB amplifier, and a line driver. The assembled catheter tip is shown in Fig. 5.1(a).

The 110-cm long catheter shaft offers omnidirectional steering achieved by manipulating 4 wires connected to an anchor ring near the tip and being controlled remotely via a mechanical joystick. The reach of the catheter is 38 mm when the tip is deflected at 90° and the maximum bending radius is 180° as shown in Fig. 5.1(b).

The probe prototypes are coated with a thin layer (about 15 μm) of a silicone-like material for electrical insulation of the array connections and passivation of the CMUT cells¹⁰⁷.

Imaging

The two probe prototypes are connected to a Verasonics Vantage imaging system (Kirkland, WA, USA), which is used to generate transmit pulses of arbitrary frequency (5 MHz – 20 MHz), amplify, digitize (14-bit, 62.5 MHz), and transfer the received sensor data to a host controller PC for real-time ultrasound image visualization or data recording. The transmit pulse frequency, number of transmit pulses and the CMUT bias voltage can be set via a graphical user

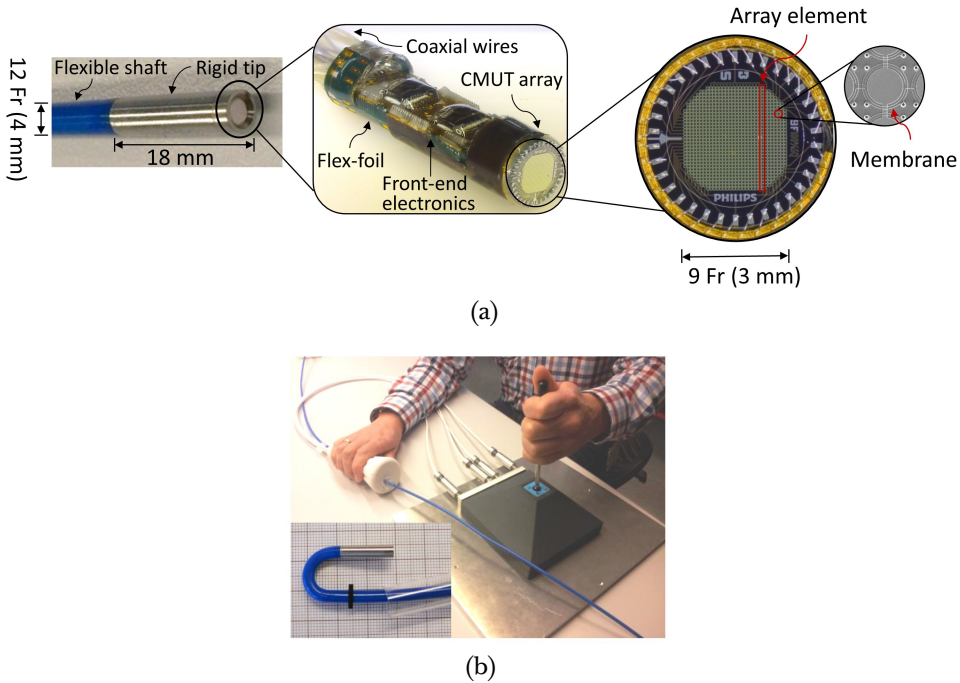


Figure 5.1: (a) assembled forward-looking catheter tip with integrated CMUT array and front-end electronics. (b) steerability of the catheter tip by a mechanical joystick.

interface which controls the Verasonics system and a programmable electronic toolbox.

Conventional line-based sector scanning¹⁰² is implemented on the Verasonics system for the real-time visualization, which is used to navigate the probes. The recording option facilitates high frame rate data acquisition for off-line processing⁴². The beamformed, high frame rate images are filtered in the fast-time domain with 50 % band-pass finite impulse response filter (FIR) centered at 6 MHz, 12 MHz, or 18 MHz yielding high-penetration, generic, or high-resolution imaging performance, respectively. A median-filter is applied on the consecutive frames to improve an image signal-to-noise ratio and to yield about 25 FPS, which is at the order of magnitude typically used for cardiac imaging. Electrocardiogram (ECG) is recorded synchronously with the pulse transmission via an audio card fitted on the host controller PC.

Passive heart platform

The concept of frequency tunability is first demonstrated by imaging an aortic valve in a passive beating heart platform (LifeTec Group BV, Eindhoven, the Netherlands) which features mechanical pumping of a porcine *ex vivo* heart freshly collected from a local abattoir. Air bubble-free, heparinized blood is

pumped through the left ventricle of the heart. The system allows precise control and monitoring of hemodynamical parameters and robust performance for up to 12 hours. Earlier validation of this platform shows reproducible physiological hemodynamics, e.g. aortic pressures of 120/80 mmHg with 5 L min^{-1} of cardiac output¹¹³.

The rigid probe prototype was inserted and sealed in the aorta facing the aortic valve (Fig. 5.2), of which the long-axis images were acquired in the three imaging modes.

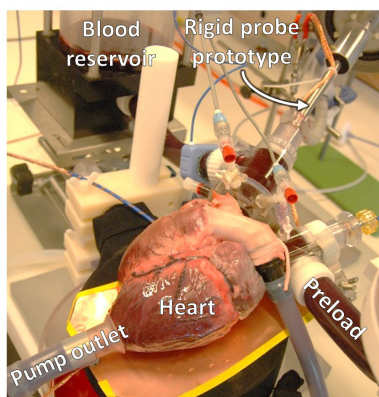


Figure 5.2: Photograph of the *ex vivo* testing of the rigid probe prototype using a passive heart platform.

Porcine animal model

Live animal studies were carried out after securing approval from the Dutch Central Commission for Animal Studies (protocol nr. AVD/115002015205) and according to the European directives (2010/63/EU) and the Guidelines for the Care and Use of Laboratory Animals (NIH). The forward-looking ICE catheter was tested in a porcine model (about 70 kg) under general anaesthesia with a mixture of midazolam, sufentail and pancuronium, and low-frequency mechanical ventilation. The animal was heparinized to avoid thrombus formation. The ECG and oxygen saturation were monitored continuously throughout the study. Access for the aortic valve imaging was obtained via a femoral artery or a left common carotid artery. Fluoroscopic images of the catheter position inside the heart were taken from the left anterior oblique view (LAO) with cranial angulation.

5.3 Results

Passive heart study

The frequency-tunable collapse-mode CMUT array is utilized to generate high-penetration depth (6 MHz), generic (12 MHz), and high-resolution (18 MHz)

images of an aortic valve in an *ex vivo* passive heart platform. Fig. 5.3 compares imaging performance of these three modes. The penetration mode shown in Fig. 5.3(a),(d) allows imaging the heart up to 10 cm, clearly visualizing the aorta, left atrium, left ventricle and providing a coarse imaging of the opening and closing of the aortic and the mitral valve. The generic mode (Fig. 5.3(b),(e)) provides increased resolution clearly depicting the leaflets of the aortic valve and a portion of the mitral valve up to the depth of about 5 cm. The high-resolution mode (Fig. 5.3(c),(f)) generates the finest detail of the aortic valve with penetration depth of about 2.5 cm.

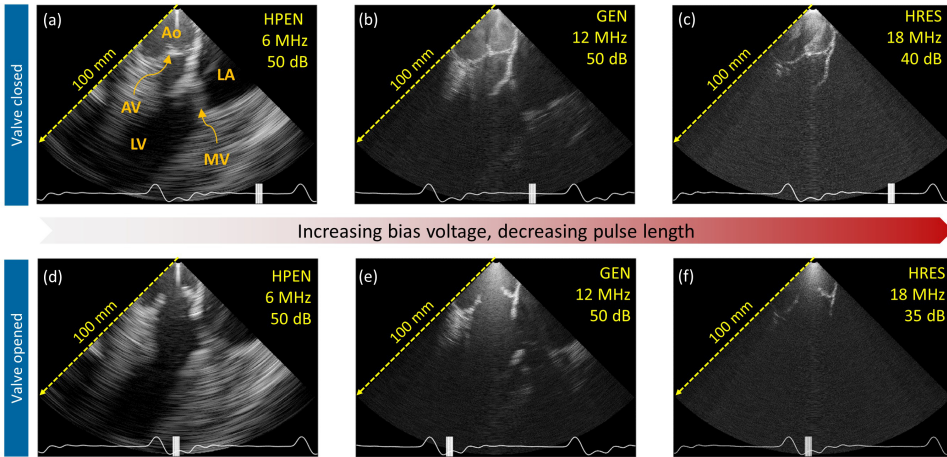


Figure 5.3: Imaging of an aortic valve using the frequency-tunable probe prototype in an *ex vivo* passive heart platform. Closed and open state of the aortic valve is shown in the top and bottom row, respectively. The imaging modes (HPEN indicates high-penetration; GEN, generic; HRES, high-resolution) and the displayed dynamic range are shown in the top-right corner. The white curve at the bottom of each image depicts the recorded ECG signal, of which the cursor indicates the displayed moment in the heart cycle.

The dynamic range in the obtained images is scaled to the peak signal intensity and optimized subjectively for display. If the Fig. 5.3(f) would be displayed at the same dynamic range as Fig. 5.3(e), it would exhibit lower contrast. Figs. 5.3(b),(c),(e),(f) utilize imaging frequency higher than 10 MHz, at which the spontaneous echo contrast of blood appears. This results in the white swirl seen above the closed aortic valve in Figs. 5.3(b),(c). The white pattern throughout the vertical center of the displayed images is common mode noise which is dominant at steering angles close to 0°.

Live animal study

To investigate the usability of having the high penetration (zoom-out) or high resolution (zoom-in) in a single device, the frequency tunability for forward-looking ICE imaging was studied in an *in vivo* animal model. The catheter prototype was first inserted via a femoral artery to the ascending part of the

aorta facing the aortic valve (Fig. 5.4(b)). Images of long-axis view of the aortic valve located at a depth of about 2.5 cm were acquired in the general mode (Figs. 5.5(b),(e)). The catheter could not be advanced closer to the aortic valve, due to its bending profile not allowing the advancement through the tight aortic arc of the porcine heart. It was therefore removed and inserted via the carotid artery (Fig. 5.4(c)). Thus close-up images of the aortic valve at a depth of about 1 cm in the high-resolution mode (zoom-in) have been obtained as shown in Figs. 5.5(c),(f). Subsequently, the catheter was pulled back to about 5 cm from the aortic valve (Fig. 5.4(a)) and images in the penetration mode were recorded (Figs. 5.5(a),(d)).

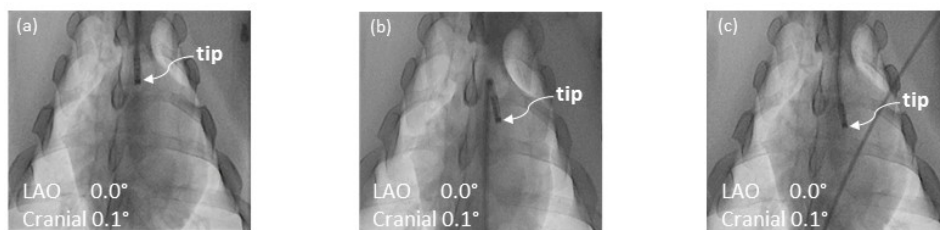


Figure 5.4: Fluoroscopic images indicating the position of the catheter's tip during the zoom-in and zoom-out imaging of an aortic valve using the developed prototype of frequency-tunable forward-looking ICE catheter in an *in vivo* animal model. The catheter is positioned at about (a) 5 cm, (b) 2.5 cm and (c) 1 cm from the aortic valve. These fluoroscopic images correspond to the ultrasound images shown in Fig. 5.5.

The zoom-in and zoom-out capability of the developed forward-looking frequency-tunable ICE catheter is shown in comparison of opened and closed aortic valve images (Fig. 5.5) displayed at 28 FPS. The opened and closed state of the valve can be identified in all three imaging modes. The penetration mode enables anatomical overview for navigation whereas the high-resolution mode allows a close-range, more detailed anatomic image of the aortic valve. The generic imaging mode provides a compromise of the two.

5.4 Discussion

This study reports on preclinical testing of a novel forward-looking ICE catheter prototype. The catheter is based on collapse-mode CMUT technology which features bias voltage-based frequency tuning to generate ultrasound images at the center frequencies of 6 MHz, 12 MHz, and 18 MHz, but any frequency in between is possible and can be changed in realtime.

It was found that intracardiac structures were delineated with satisfying image resolution or penetration depth. The frequency-tunable catheter can visualize anatomical structures of various sizes at different distances relative to the catheter tip, enabling both wide overviews and detailed close-ups.

The catheter prototype presented in this study has an active aperture of 9 Fr but outer diameter of 12 Fr, due to the wirebonds which connect the CMUT

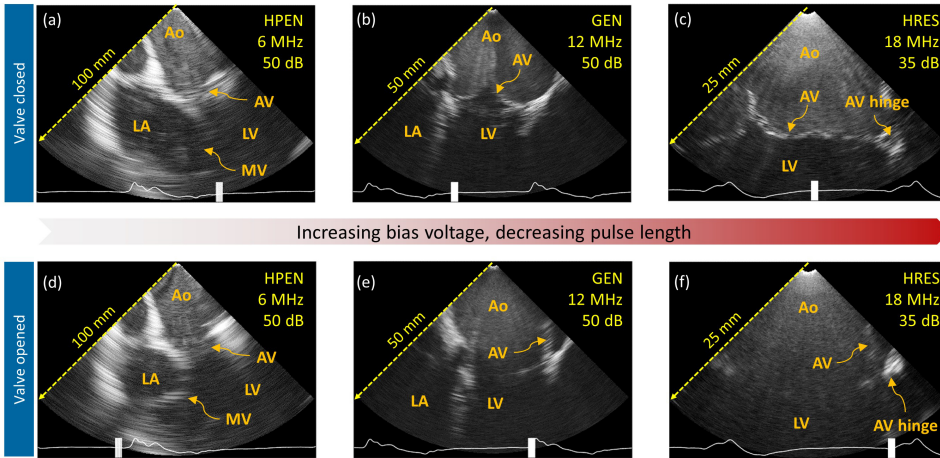


Figure 5.5: Imaging of an aortic valve using the developed prototype of frequency-tunable forward-looking ICE catheter in an *in vivo* animal model. Closed and open state of the aortic valve are shown in the top and bottom row, respectively. The imaging modes (HPEN indicates high-penetration; GEN, generic; HRES, high-resolution) and the displayed dynamic range are shown in the top-right corner. The white curve at the bottom of each image depicts the recorded ECG signal, of which the cursor indicates the displayed moment in the heart cycle.

array with the front-end electronics. Clinical practise requires the diameter to be reduced to at least 10 Fr. This could be achieved either by monolithic integration with the front-end electronics or by utilizing a flex-to-rigid technology^{30,114}. A decreased shaft diameter would increase the catheter's deflectability and steerability, which were found to be crucial for easy navigation in the confined space of the heart.

The potential gain in navigation efficiency of the forward-looking design, which is similar to using a flashlight, towards the specific feature of interest needs to be proven in a future study.

Even though it is common practice to place a commercial ICE catheter inside the right atrium, or aorta for investigational guidance¹², its restricted bandwidth and side-looking design limits its diagnostic capability, e.g. for infective endocarditis. Figure 5.6 shows a long-axis view of the aortic valve obtained at a frequency of 6 MHz with a commercial side-looking ICE placed in the right atrium *in vivo*. Lateral resolution of the commercial ICE is better, which is to be expected due to its seven times larger aperture. Nevertheless, it provides only a limited visualization of the aortic valve. The catheter design presented in this study allows for a complementary view and its switching to higher operation frequency exploits the usage of ICE for close-up high frequency diagnosis of the heart valves.

High frequency imaging would also allow for near-by thrombus detection or guidance of percutaneous biopsies of intra-aortic masses suspected to be

tumours. It is foreseen that frequency-tunable forward-looking ICE catheter will exploit the use of ICE for diagnosis of heart valves, guiding LAA closure and real-time lesion visualization during ablation procedures.

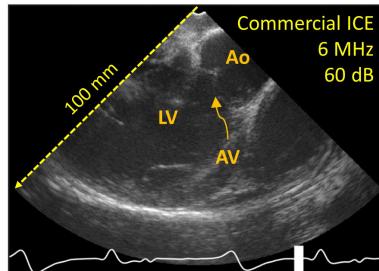


Figure 5.6: Long-axis view of a closed aortic valve (AV) obtained with a commercial ICE catheter (6 MHz phased-array, 64 elements, aperture size of 13 mm) placed in right atrium in an *in vivo* animal model. Ao and LV indicate aorta and left ventricle, respectively. The displayed dynamic range is shown in the top-right corner. The white curve at the bottom of the image depicts the recorded ECG signal, of which the cursor indicates the displayed moment in the heart cycle.

5.5 Conclusions

A rigid probe and a steerable ICE catheter prototype, both equipped with collapse-mode frequency-tunable forward-looking CMUT array, have been successfully tested in a passive heart platform and an animal experiment, respectively. Images of the aortic valve acquired in high-penetration (6 MHz), generic (12 MHz), and high-resolution (18 MHz) mode show satisfying image quality and penetration depth between 2.5 cm and 10 cm for the imaging aperture of $2 \times 2 \text{ mm}^2$. The ICE catheter prototype placed in the ascending aorta was utilized to image the aortic valve at multiple depths *in vivo*. It was found that the combination of the forward-looking design and frequency-tuning feature allows visualizing intracardiac structures of various sizes, e.g. leaflets of the heart valves and the ventricle at different distances relative to the catheter tip, providing both wide overviews and detailed close-ups. The promising approach may substantially influence the future role of forward-looking ICE in the clinical practice.

5.6 Acknowledgements

The authors would like to thank the following people for their effort and support in this study: Michel van Bruggen, Frank Budzelaar, Geert Gijssbers, Jeanet van Rens, Marc Notten, Bas Jacobs, Wim Weekamp, Alfons Groenland, Ferry van der Linde, Maurice van der Beek, Debbie Rem-Bronneberg, Wendy Dittmer and René Aarnink. This research is in part funded by European Union Seventh Framework Programme project „OILTEBIA“, grant no. 317526.

Part II

Wiring Electronics with Light

All-Optical Fiber Link for Catheters

This chapter has been published as:

Martin B. van der Mark, Anneke van Dusschoten, and **Martin Pekař**, All-optical power and data transfer in catheters using an efficient LED, *Proceedings of SPIE Photonics West, Bios*, 9317-13 (2015).

Abstract

Diagnostic value of minimally invasive medical devices can be improved by putting electronic functionality at the tip. At the same time the device should remain slim, flexible and affordable. We show transfer of high power and data over a catheter by a single optical fiber and LED. We find that simultaneous photovoltaic power conversion and data communication can be achieved via Photo-Induced Electro Luminescence (PEL), but only in case the LED has a high bidirectional conversion efficiency ($\eta > 0.3$). This eliminates the necessity of using thin electrical wires with fragile interconnects that compromise bandwidth as well as RF and MRI compatibility.

6.1 Motivation

There is a clear and ongoing trend to replace conventional surgical procedures with minimally invasive interventions. Reduced trauma, shorter hospital stay and reduced cost are the most important drivers of the adoption of minimally invasive techniques. To enable further innovation in medical instrumentation – thus enabling more advanced and more challenging minimally invasive interventions – there is a need to integrate miniature sensors for in-body imaging and physiological measurement as well as actuator for treatment in instruments like needles, catheters and guide wires.

The problem

When integrating sensors or actuators in the tip of interventional devices, the required electrical supply power and data transfer can be challenging, in particular when a high data-rate return channel, consisting of many electrical wires, must be integrated in the device. This is due to several reasons:

1. The combination of the small cross section (i.e. small diameter) combined with the long length of a guide wire or catheter does severely limit the total number of electrical wires that can be integrated in such an instrument.
2. The integration of (multiple) electrical wires compromises bending, a key property of the instruments.
3. For high data rate, such as required for an ultrasound image transducer or in case of low signal measurements, one often requires coaxial cables which may need even more space compared to single-core wires.
4. Instruments with electrical wires are typically incompatible and unsafe with the use of MRI^{43,115–117} due to resonances in the electric wiring leading to image artifacts, voltage build-up and heating.
5. Thin electrical cables are fragile and have poor RF compatibility.
6. Galvanic isolation of the patients is always an issue.

On top of the issues above, manufacturability is more difficult and assembly costs will go up, which is undesired because these devices are single-use disposables. The goal of this paper is to explain how we have been able to underpin and built an opto-electronic technology which we believe will make possible a much better, smarter and cost effective generation of catheters and guide wires.

The proposed solution

We propose that the wires for the high bandwidth data channel could be replaced by a single optical fiber. This will immediately solve issues of size, flexibility, galvanic isolation, RF and MRI compatibility, but may require massive multiplexing of data at the distal end as well as a (tiny) suitable light source for

data transmission. The latter can be realized with a vertical cavity surface emitting laser (VCSEL), whereas the electronics is application specific: an ASIC should be designed that can multiplex sensor data and drive the VCSEL. This in turn requires electrical power and wires to supply it. Now the question arises of whether we can use the same optical fiber to transport optical energy from the proximal side that may be converted to electricity to power ASIC and sensors at the distal end of the instrument. Indeed we propose that most problems may be solved by using an optical fiber for both power and data transfer. Some optical power source is therefore needed such as a laser (or perhaps an LED) and electricity will be generated by photovoltaic conversion at the tip of the medical instrument. Although this has been tried for specific cases before^{44,115,118}, the general opto-electronic technology solution to do so appears challenging. Some obvious requirements for a suitable power converter are that it must be small (due to limited space), it must have high efficiency (instrument temperature must stay below 42°C) and that it should typically deliver more than 1.65 Volt to drive the electronics. At the distal end of the medical device (the tip), the optical fiber connects to the photovoltaic cell for power conversion. Given the small lateral limitations in space, it is not obvious or trivial how to integrate another light emitting and receiving element for data communication on the same spot, using a beam splitter or grating. Stacking of devices is also challenging from a manufacturability point of view. To come to a solution we have now replaced our earlier set of challenges with another set. These will be addressed in what follows.

6.2 The essential parts of the system

Communication

For bi-directional data communication we need a transmitter and receiver on both ends of the catheter, as well as an optical fiber to connect them. A schematic overview is shown in Fig. 6.1. The catheter will be plugged into a console that will contain the laser and receiver on the proximal side where size or cost are not limiting factors and we are rather free to choose the communication wavelength. The difficult part is in the distal end and this is why we opt for a VCSEL to send data. We could use a VCSEL from ULM Photonics, for example ULM850-10-TT-C0104U, which operates at a wavelength of 850 nm, has maximum data rate of 10 Gb s⁻¹ and a chip diameter of 250 μm.

Optical fiber

The optical fiber must be integrated in the catheter and may be based on polymer or glass. Standard size optical glass fiber is flexible, has a buffer size of 250 μm (acrylate) or 155 μm (polyimide), a glass (cladding) diameter of 125 μm and a core diameter ranging from 5 μm – 110 μm with numerical aperture NA = 0.1 – 0.2. It is transparent over a wide range of wavelengths and also bandwidth is not an issue, even if highly dispersive multi-mode fiber would be used because distances are a few meters at most. Fused silica optical fibers of larger

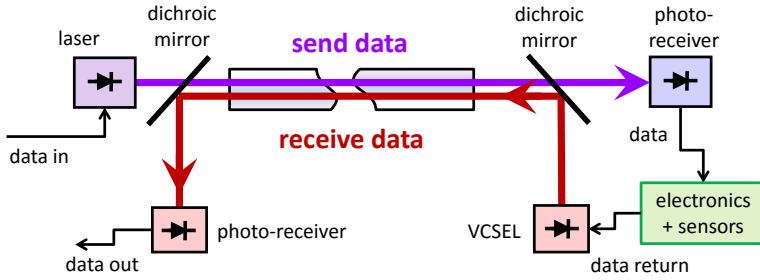


Figure 6.1: Schematic overview of bi-directional communication from proximal to distal side of a catheter. The laser, dichroic mirror and photo-receiver on the left are in the console, optical fiber, VCSEL, electronics, sensors, a second dichroic mirror and photo-receiver are in the catheter (the disposable part). Send and receive are preferably done at different wavelengths, but other configurations are possible.

diameters exist, but flexibility may become an issue. Larger diameter fiber with high NA are interesting because it may help to collect light from the transmitter at the distal end, for example if we want to omit the dichroic mirror or if we want to replace the VCSEL (when low data rate is sufficient) by a much more cost effective source such as an LED. The LED emission has rather high etendue, its light is diffuse and coming from a large area compared to the collimated or conical emission from a laser. As a more flexible alternative to glass fiber we could use polymer fiber (usually made of PMMA) and of a 0.5 mm diameter. These fibers may have high numerical aperture, $NA = 0.5$, (for example SKA POF CK20 Mitsubishi) and hence can collect an order of magnitude more light than glass fiber. Disadvantage is the absorption loss in the near infra-red (which may be less than 50 % transmission for one meter fiber at wavelengths above 850 nm) and in the blue-violet part of the spectrum. Potentially, fluorinated polymer fiber can improve this.

Photo-voltaic conversion at the catheter tip

Most preferably, we would like to avoid using any electrical wires in the catheter and use an optical fiber for optical power delivery, see Fig. 6.2. Possibly, we can even use the same optical fiber that is used for communication and functionally combine the layouts of Fig. 6.1 and Fig. 6.2. Most of all we must find a suitable photovoltaic power converter that may for example consist of a silicon p-n junction and a voltage up converter.

As mentioned earlier, the limited space available at the tip of a catheter (less than a mm^3) or guide wire imposes demanding requirements on the photovoltaic power converter, in particular if we want to drive some complex electronics that needs a few tenths of a Watt at, say, 2 V. Taken all together, we find the following list of requirements for a photo voltaic power converter at the catheter tip:

- Small and simple (< 1 mm in all directions)

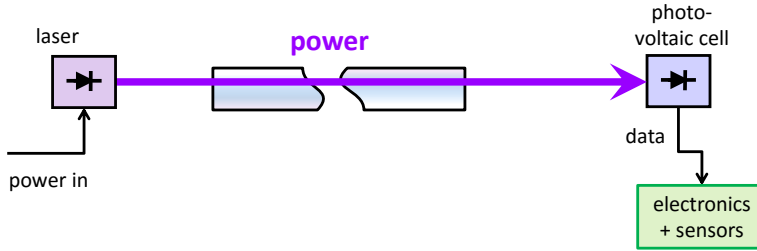


Figure 6.2: Optical power source, fiber and photovoltaic cell to power the electronics.

- High power density ($> 100 \text{ mW mm}^{-2}$)
- High efficiency (temperature $< 42^\circ\text{C}$, to prevent tissue heating)
- Voltage $> 1.65 \text{ V}$ for driving the electronics
- Voltage $> 40 \text{ V}$ to drive or bias an ultrasound transducer

If we confront those requirements with the properties of a Silicon photodiode

- Power density $< 10 \text{ mW mm}^{-2}$
- Efficiency $\eta \approx 25 \%$
- Voltage 0.5 V

First of all, we see that the power density is not suitable for demanding applications. To obtain more than the required 1.65 V at least 4 elements must be put in series, thus increasing size or reducing area, or instead a voltage up-converter must be added leading to additional losses, complexity and increase in size. Also the efficiency of $\eta = 25 \%$ is not very high compared to that of an electrical wire ($\eta > 99 \%$) of course, although it is doubtful that we can do much better. Then again, one should realize that the relative amount of heat H generated for a 50% efficient converter is a factor of 3 smaller than for a 25% efficient converter:

$$H = \frac{1-\eta}{\eta}, \quad (6.1)$$

Mostly based on power density arguments however, the conclusion must be that a silicon photodiode cannot do the job. In the next chapter we will discuss the solution we have found, and this is the most important result of this paper.

6.3 Photovoltaic conversion using a blue LED

A key insight

What we want for our small photovoltaic cell is a higher voltage so that we can eliminate voltage up-conversion. This can obviously be realized by using

a semiconductor material with a higher band gap than Silicon, such as Gallium Nitride (GaN). This material has a 3.4 eV gap in its pure form. Remarkably photovoltaic devices based on GaN seem to be very rare, if exist at all. The insight gained here is that any p-n junction is photo sensitive and that hence it should be possible to use an LED in reverse. While the band gap of a blue (InGaN) LED is 2.8 eV, the efficiency for blue emission can be as high as 43 %. In what follows we will present the characteristics for an LED used in reverse.

Characterization of a blue LED

We have tested several LEDs of different emission colors and pump wavelengths and found that blue LEDs work best. In this paper we report on some measured I-V curves and maximum power level of a particularly well performing blue LED, the Philips Lumileds Luxeon Z, Royal Blue (446 nm peak emission wavelength). In normal, forward, operation the LED runs on 1 A at 3 V with efficiency up to 43 %. Its area is just 1 mm², see Fig. 6.3, so we have a (forward) power density of about 1000 mW mm⁻².

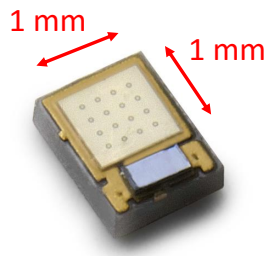


Figure 6.3: The Philips Lumileds Luxeon Z, Royal Blue LED.

For photovoltaic (reverse) operation of the LED, we have to illuminate it with a suitable light source. Presumably, for maximum possible efficiency, the wavelength of that source should be shorter than, but as close as possible to the emission wavelength of the LED so that the Stokes shift and loss associated with it is low. The maximum sensitivity of a photo cell is $S = \lambda e/hc$, which corresponds to 100 % Quantum Efficiency. The absorption of light is small at the band gap however and it increases steeply to 100 % at some 5 – 10 % shorter wavelength depending on the thickness of the absorbing layer in the photo cell.

For our blue LED with a peak emission wavelength of 446 nm, it appears that photo voltaic conversion works very well when illuminated with violet light of 405 nm. This means that a blu-ray disc laser, which operates at that wavelength, is a very suitable pump source.

We have measured some I-V curves (current-voltage characteristics) for the Philips Lumileds Luxeon Z at three different illumination powers, see Fig. 6.4. To measure such a curve a variable resistance is connected to the leads of the LED so that the load (the conductance) can be varied. What we see is that the curves are quite square and have a high fill factor. This means that the voltage drop upon increasing the load is quite limited up until the point where

more power is demanded than what is converted. For the curve with the highest pump power ($P_{\text{laser}} = 52.1 \text{ mW}$), the photovoltaic power generated at the Maximum Power Point (MPP) is $P_{\text{out,MPP}} = 2.23 \text{ V} \times 9.8 \text{ mA} = 21.9 \text{ mW}$. The MPP is where the most optimum conversion efficiency is obtained, in this case: $\eta = 21.9/52.1 = 42 \%$.

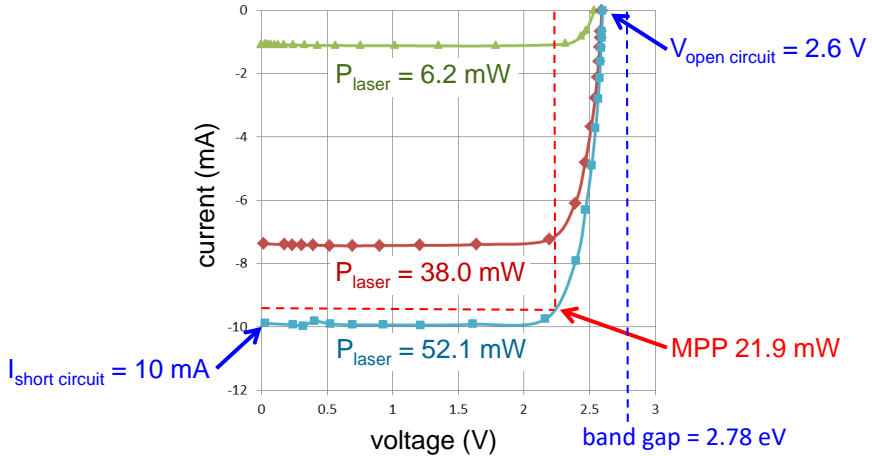


Figure 6.4: Three I-V curves at different laser powers for the Luxeon Z with a peak emission wavelength of 446 nm. A laser with a wavelength of 405 nm was used as illuminating pump source.

For a similar LED (444 nm peak emission wavelength) we have measured conversion efficiency as a function of laser pump wavelength, see Fig. 6.5, which shows that 405 nm is close to the optimum (left), and that the electrical output power as a function of optical pump power is linear to at least 200 mW electrical output (right). As a pump source a frequency doubled Ti:Sapphire laser (Mai Tai Inspire) was used. This laser is tunable in wavelength and has high average output power. We found that the efficiency is 33 % which is lower than expected (42 %) from experiments in which we used a continuous wave laser. The Mai Tai operates with femtosecond pulses at a repetition rate of 80 MHz. We do not know whether this or the laser beam quality or something else is the cause of this difference.

In further experiments using a 401 nm multi-mode semiconductor laser we have seen 333 mW output power at 1 W input power. The electrical output power is linear with optical input power within the experimental error and we may conclude that the LED output is not saturating and that the maximum power density it can handle is at least 1 mW mm^{-2} .

The key insight we have obtained is that silicon based photo-voltaic conversion (such as in solar cells) is totally inadequate for power conversion in a very small space. We have found that a solution is given by GaN based devices such as the blue InGaN LEDs for pumping phosphors in high-lumen lighting applications, combined with a violet laser source (such as a blu-ray diode laser). In Tab. 6.1 we summarize the difference between Silicon and Gallium Nitride

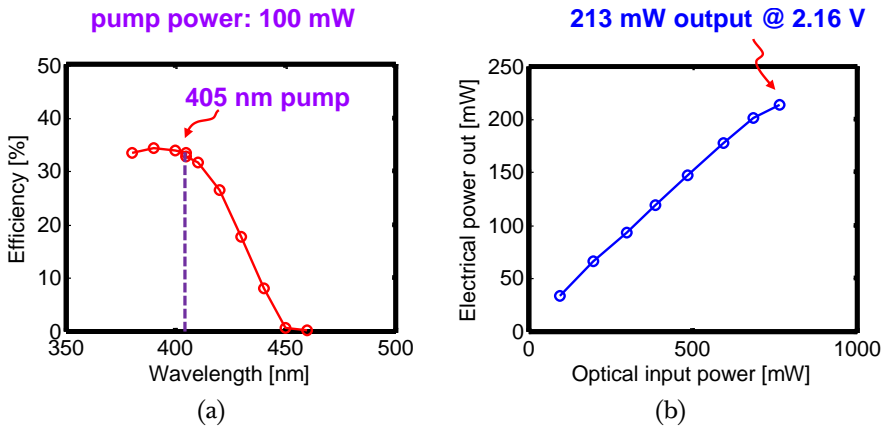


Figure 6.5: The efficiency as a function of laser wavelength showing that 405 nm is close to the optimum (a), and the electrical output power as a function of optical pump power (b) which is linear to at least 200 mW electrical output.

devices. The material has a suitable high direct band gap of about 2.8 V, is very robust, non-toxic and has high thermal conductivity. InGaN is estimated to be two orders of magnitude better than Si (as a combination of power density, efficiency, and conversion voltage at the maximum power point) for application in medical devices.

Table 6.1: Performance of a Si-photodiode versus a blue InGaN-LED.

	Silicon	Indium Gallium Nitride
Band gap	1.1 eV (indirect gap)	2.8 eV (direct gap blue LED), (3.4 eV direct gap for GaN)
Power density	10 mW mm ⁻²	1000 mW mm ⁻²
Voltage at MPP	0.5 V	2.3 V
Efficiency (PV)	$\eta \approx 25\%$	$\eta \approx 42\%$
Efficiency (EL)	$\eta = 0\%$ (no emission)	$\eta \approx 43\%$

These are very encouraging results and they fit our requirements as mentioned in Section 6.2. In addition, an InGaN LED is a *bidirectional* device and unlike a Si photodiode may be used for return signal transmission. We will come back to this in Section 6.3, as well as in the discussion.

High voltage LED for driving an ultrasound transducer

In some applications we may want to drive actuators or to read out sensors that require a high (bias) voltage. One such application is foreseen where capacitive micromachined ultrasonic transducers (CMUT) may be used for ultrasound imaging at the catheter tip. Bias and driving voltages may be as high as 150 V but technological developments have brought this down to 40 V in some cases.

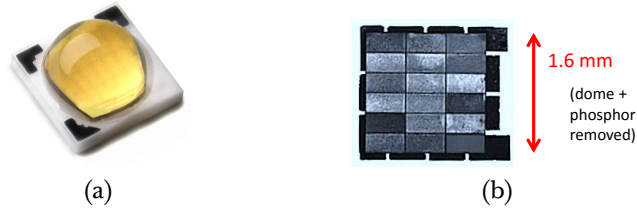


Figure 6.6: The Luxeon H (a) has 18 LED segments in series as we can see when dome and yellow phosphor have been removed (b).

It is a lucky coincidence that the lighting industry has developed blue LEDs suitable for high voltage to make them compatible with the mains power of 120 Volt and 240 Volt. For example, the Philips Lumileds Luxeon H is a 50 Volt LED with 18 monolithically integrated LEDs of $1.6 \times 1.6 \text{ mm}^2$, see Fig. 6.6. It is covered with a yellow phosphor to produce white light and a silicone dome for efficient light extraction. With our purpose in mind and used in reverse, this LED seems a very suitable candidate if we remove the dome and phosphor.

We have connected two high voltage LEDs in series, illuminated them with laser light of 405 nm and measured photovoltaic output of up to 93 V and more than 2.1 mA with $> 23 \%$ efficiency. In Fig. 6.7 a typical result is shown. The hackle in the curve is a consequence of inhomogeneity of illumination but also on different efficiency of the individual LED segments, a phenomenon well known from solar panels. We believe that more homogeneous illumination is possible and should result in higher efficiencies.

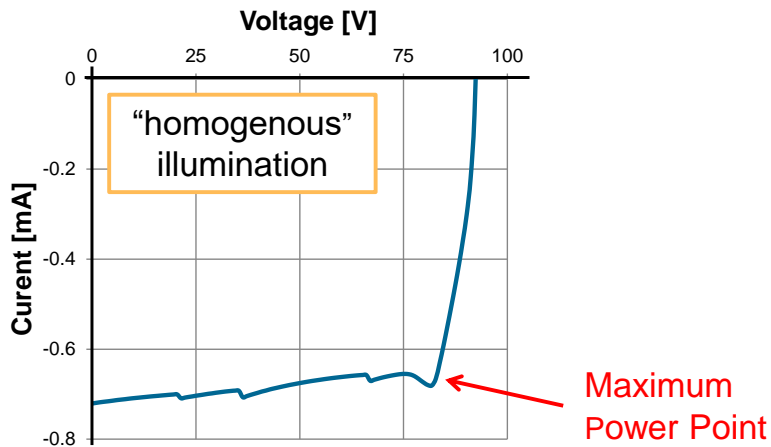


Figure 6.7: Photovoltaic output from two LEDs (Philips Lumileds Luxeon H) connected in series. Illumination was quasi homogeneous. From both LEDs the phosphor and dome have been removed.

Three types of luminescence

Now we return to the standard blue LED we used before and look closer to the different ways we can use it. First of all there is the normal use of LED as a light source; the energy from an input current is converted to produce light. This is called electroluminescence (EL, current \rightarrow light). Second, there is photoluminescence (PL, light \rightarrow light); light emission at the EL wavelength which occurs when light of higher energy than the band gap is illuminating the LED. This is the same situation that also produces a photovoltaic current and it may be seen as a “parasitic” effect for our purpose of photovoltaic conversion (PV). The emission is not very strong compared to EL at the same input power, however.

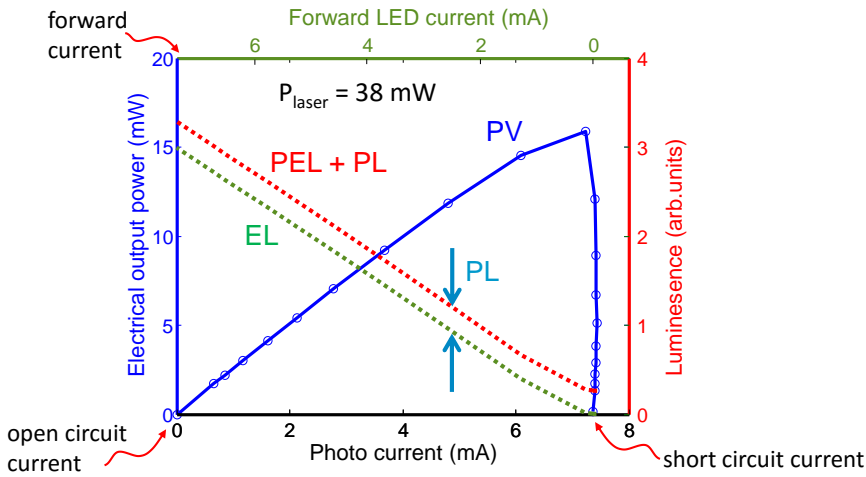


Figure 6.8: The measured output power from a Luxeon Z for PV (bottom and left axes), EL (top and right axes) and PEL + PL (bottom and right axes). Input laser power for PV conversion and PEL + PL is 38 mW. The level of PL is constant and is the difference between PEL+PL at the short circuit current. The slope of PEL + PL and EL are similar because $\eta_{PV} \approx \eta_{EL}$. The luminescence (right axis) was scaled in such a way that it almost corresponds with (optical) output power (left axis).

Then there is a third kind of luminescence effect¹¹⁹, called photo-induced electroluminescence (PEL), which is relatively unknown. PEL will occur when an LED is illuminated while its leads are connected to a resistance that is high enough for the LED to build up a voltage higher than the band gap. As a consequence the LED will start to conduct and emit light, as it does in EL. So for PEL we find light \rightarrow voltage \rightarrow current \rightarrow light. In the case of efficient LEDs this provides strong emission without a current source and variation of the load will modulate the PEL output level. The efficiency of PEL is the product of the photovoltaic power conversion efficiency and that of electroluminescence. For example, maximum emission is obtained at open circuit of the LED where it amounts: $\eta_{PEL} = \eta_{EL}\eta_{PV} \approx 18\%$ in case $\eta_{PV} \approx 42\%$ and $\eta_{EL} \approx 43\%$.

In Fig. 6.8 the measured output power from a Luxeon Z is shown in cave of photovoltaic conversion (PV) (bottom and left axes), EL (top and right axes) and PEL + PL (bottom and right axes). Input laser power for PV and PEL + PL is 38 mW. The level of PL is constant and is the difference between PEL+PL at the short circuit current. The slope of PEL + PL and EL are similar because $\eta_{PV} \approx \eta_{EL}$ and hence the total output power from the LED is (almost) constant, divided up between light and electricity, depending on the applied load. The luminescence (right axis in Fig. 6.8) was scaled in such a way that it almost corresponds with (optical) output power on the left axis.

PEL can be used for communication

We have realized that it is possible to simultaneously use the same LED for power conversion and to send and receive data¹²⁰ via PEL. In Fig. 6.9 we show a combined power and data link using PEL. The electronics powered by the LED has the property that it can vary its own load (its conductance) on the LED. The variable load modulates the LED light output by the PEL effect which corresponds to data to be sent to the proximal end of the optical link.

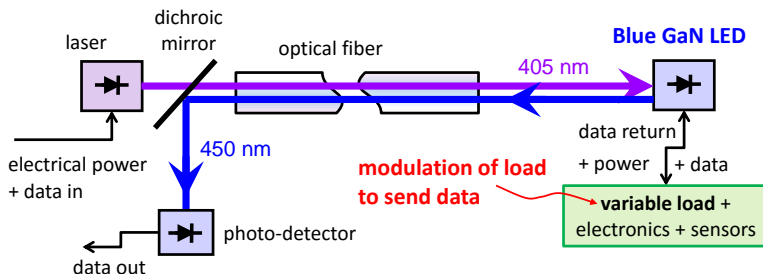


Figure 6.9: An optical power and data link with just one fiber and a single LED as transceiver and photovoltaic converter. The electronics can vary its load on the LED which modulates the PEL effect and makes the LED send pulses of light.

6.4 Demonstrator: a catheter with CMUT pressure sensor

To demonstrate the concept of the optical power and data transfer using an LED we have built an all-optical catheter. The complete catheter consists of a pressure-sensing tip at the distal end, a catheter shaft enclosing an optical fiber and a dummy handle from which the single optical fiber connects to a proximal console.

The pressure sensor

The capacitive pressure sensor was fabricated using micro-electromechanical systems (MEMS) technology and integrated together with an ASIC on a single chip. Here we will only present the basic concept because detailed description

of the sensor functionality is outside the scope of this paper. The chip essentially consists of a reference voltage circuitry and a membrane capacitor. A current source is used to deliver charge on the membrane capacitor leading to a voltage build-up V_c over time t , up to the source voltage V_s ,

$$V_c(t) = V_s \left(1 - e^{-t/\tau} \right). \quad (6.2)$$

The actual voltage V_c on the capacitor is continuously compared with the reference voltage. Once the reference level is reached, the capacitor is discharged via a switch (to account for discharging time the actual device contains two sensors which operate in switching mode). The characteristic time it takes for the capacitor to charge through the resistive load R is equal to $\tau = RC$, where the capacitance of the membrane $C = \epsilon S/d$ depends on the separation distance d between the top flexible membrane and bottom electrode of surface area S as well as the permittivity ϵ of the medium in the capacitor's gap (typically air). An external pressure applied on the membrane will cause a change in the separation distance d resulting in a change of capacitance. Depending on the external pressure, the membrane capacitor gets charged up to the reference voltage faster (decreased external pressure) or slower (increased external pressure). The integrated ASIC translates the pressure-dependent time constant into a frequency modulated signal.

The pressure sensing chip has three terminals in total, positive power supply (typically 2.0 V – 3.3 V), ground and frequency output (around 1 MHz at the atmospheric pressure).

Power to the sensor

Using the concept described earlier in this paper a single blue LED (a smaller, $0.7 \times 0.7 \text{ mm}^2$, experimental version of the Luxeon Z) was used to provide electrical power for the chip. A blu-ray laser was used to illuminate the GaN blue LED at the wavelength of 405 nm. Before final assembly of the catheter tip we have measured that for an input laser current of 36.3 mA, an optical power of 3.8 mW was delivered at the LED surface from the 0.5 mm thick plastic optical fiber (SKA POF CK20 Mitsubishi), as was measured using a photodiode (Hamatsu S2386-8K). This 3.8 mW optical power generated a voltage of 2.35 V and an electrical current of 0.37 mA to deliver 0.9 mW of electrical power to the low-voltage ASIC connected at the LED's terminals. The ratio of the optical and electrical power gives an overall conversion efficiency of 23 % for the complete system.

Signal transfer

The pressure-dependent frequency-modulated output signal is used to modulate the electroluminescence signal from the LED using some simple external electronics. Schematic lay-out of the electronics at the distal end is shown in Fig. 6.10. The ASIC is provided with positive and negative voltage supply from

the LED and the ASIC's pressure-dependent output signal is utilized to control the inverter with open collector (type 74AUP2G06 with SOT891 casing). As a result the inverter modulates the load on the LED by pinching off the current from the LED and at the same time the ASIC draws its own power from the capacitor.

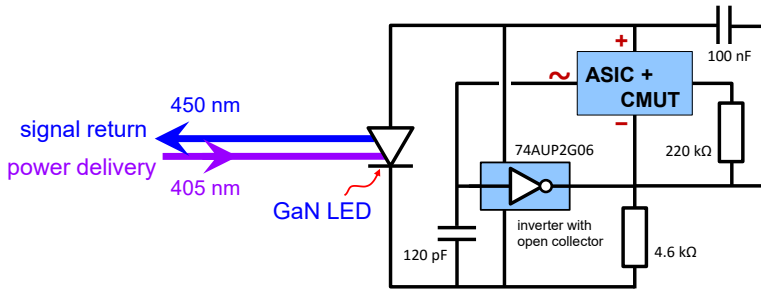


Figure 6.10: Schematic lay-out of the electronics at the distal end. The ASIC modulates the load on the LED by pinching off the current from the LED, at the same time drawing its own power from the capacitor.

In accordance to the concept described earlier in this paper, modulation of the load on the LED results in intensity modulation of the photo-induced electroluminescence light (PEL) which is collected via the same optical fiber as used for “pumping” the LED. At the proximal end, the PEL light of 450 nm wavelength is separated from the laser light (405 nm) by a dichroic mirror with subsequent detection by a silicon photodiode (Hamamatsu S2387-66R). The detected signal is further amplified and filtered by a custom-made trans-impedance amplifier (1000 VA^{-1}) and displayed on an oscilloscope.

Result

The final catheter assembly is shown in Fig. 6.11. The outside diameter of the catheter's tip and shaft is 2.3 mm. The plastic tip encapsulates the LED and the pressure-sensing electronics together with the electronic circuitry shown in Fig. 6.10. The tip is fitted at the end of a PEBAX catheter shaft. The optical fiber runs through the whole shaft as well as the dummy handle and is the only connection between the catheter's tip and the proximal end. At the proximal end the fiber is fitted with a standard optical connector which screws to the console (not shown in Fig. 6.11).

The complete demonstrator was tested at atmospheric pressure. The observed pressure-dependent signal detected by the photodiode was a continuous sine wave with a frequency of 940 kHz. Note that the bandwidth of the system is limited to approximately 500 kHz due to the LED capacitance, filtering the square wave from the ASIC to a sine wave. The pressure sensitivity at 1 bar is approximately $0.4 \text{ kHz mbar}^{-1}$ and S/N was approximately 10. Sensor read-out was found to be consistent with the previous experiments done with the same chip connected via conventional electrical wires.

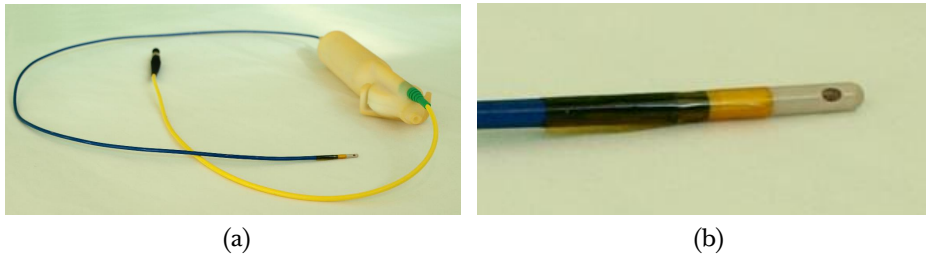


Figure 6.11: Pictures of the all-optical catheter (a) and tip encapsulating the LED and pressure-sensing electronics (b).

6.5 Discussion

Others have used LEDs and photodiodes to build transceivers in fiber networks for different applications^{121,122}. In this paper we have shown a unique application of a single LED that is used simultaneously as a photovoltaic converter, as well as a transmitter. It requires little imagination to see that modulation of the pump source may enable transmission of data in the other direction as well. The effect of photo-induced electroluminescence (PEL) allows us to combine all these features on a single junction device that therefore may be very compact.

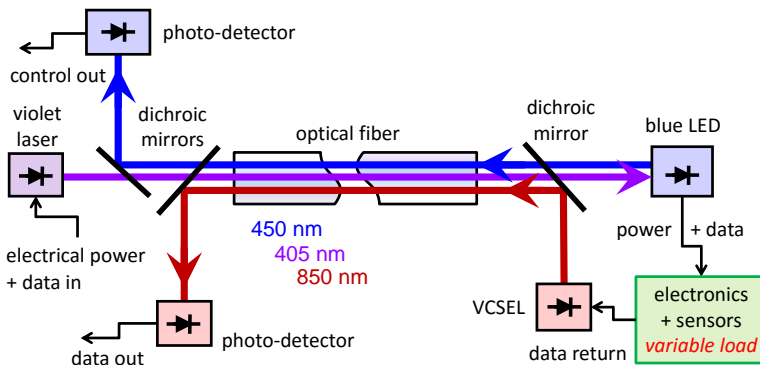


Figure 6.12: The combined power and data link with just one fiber and a single LED as photovoltaic converter, load sensor and transceiver of MHz bandwidth. A VCSEL is used for GHz bandwidth return signals such as required for imaging at the catheter tip.

We have not discussed an important extra feature that comes with PEL, that of optical monitoring of the power load or the possibility of feedback. Looking at Fig. 6.8 we can see that the electrical output power grows steadily with increasing load and then drops steeply just beyond the maximum power point (MPP). In an application where the load is unpredictable or may vary with time, the input laser power may suddenly run short and the supply voltage may col-

lapse. This may be prevented by high laser power continuously, but that in turn may lead to inefficiency and high temperature at the catheter tip. It is therefore beneficial to monitor the load, and this can be done easily using the PEL signal and feedback the outcome to the laser driver. In Fig. 6.12 a combination of a power and data link with control signal from PEL is shown. It has just one fiber and a single LED as photovoltaic converter, load sensor and transceiver of MHz bandwidth. A VCSEL is used for GHz bandwidth return signals such as required for imaging at the catheter tip. It should be noted again that the efficiency of PEL is $\eta_{\text{PEL}} = \eta_{\text{EL}}\eta_{\text{PV}}$, the product of the photovoltaic power conversion efficiency and that of electroluminescence. The amount of light received from PEL at the end of an optical fiber in a catheter is limited by the relative size of the fiber core and LED, as well as the NA and attenuation losses of the fiber. In a compact design, as required in a catheter tip, it appears hard to get losses much lower than a factor of 10. This means that if, for example, both $\eta_{\text{PV}} \approx \eta_{\text{EL}} \approx 30\%$, we can only harvest $0.3^2/10 = 0.9\%$ of the power as emitted PEL light at open circuit. With the load connected, the received PEL intensity will be even less and for this practical reason we suggest that the benefit of PEL is only significant in case the LED has high bidirectional conversion efficiency: $\eta_{\text{PV}} \approx \eta_{\text{EL}} > 0.3$.

6.6 Conclusions

In this paper we have presented the idea and development of an all-optical fiber link for both power and data streams with the aim to replace all electrical wires in catheters, guide-wires, needles etc. The key insight we have obtained is that silicon based photo-voltaic conversion (such as in solar cells) is totally inadequate for power conversion in a very small space. We have found that a solution is given by GaN based devices such as the blue LEDs for pumping phosphors in high-lumen lighting applications combined with a violet laser source (such as a diode laser for blu ray disc).

Using a violet laser we have shown photovoltaic conversion using a blue LED in reverse. A voltage of 2.3 V at 150 mA at the maximum power point is sufficient to power CMOS electronics, and a voltage of 40 V at 2.1 mA from a high-voltage LED is sufficient to drive an actuator or ultrasound transducer. The high efficiency and millimetre size of those devices are sufficient to be used in many demanding and dedicated applications. We have been able to fulfil all requirements mentioned at the beginning of this paper, and more, for example the application of photo-induced electroluminescence. No doubt we have also created new interesting challenges which may be addressed in future work.

We have found that the simultaneous transfer of high power and data can be achieved by a single LED via photo-induced electroluminescence (PEL), the effect of forward current through the LED as a consequence of open-loop voltage build-up. This is only practical, however, in case the LED has high conversion efficiency in both directions. In addition we have described how PEL may be used to monitor and control the power load of the entire link.

As a demonstrator, we have built a pressure sensing catheter with monolith-

ically integrated ASIC and pressure sensitive MEMS (CMUT) at the device tip. The device is powered by a 405 nm laser from the proximal end of the catheter and coupled via an optical fiber to a blue LED at the tip that serves simultaneously as a photovoltaic source and as a light source for signal transfer, back over the same optical fiber.

Compared to state-of-the-art electrical wiring, the integration of optical fiber technology for all-optical power (photovoltaic transfer of electrical power using efficient LEDs) and data transfer is very promising. By the nature of its construction, in the absence of conductors, it should show no RF interference and should have excellent galvanic isolation and MRI compatibility. It allows for slender devices with good flexibility (low bend radius) which are robust and simple to assemble. On top of the advantages listed above, a high level of integration improves performance while lowering cost. We believe this is the key feature in favor of this opto-electronical technology which will make disposable smart devices affordable.

Acknowledgements

The authors would like to acknowledge Peter Dirksen and Jeannet van Rens for designing the MEMS pressure sensor. We also would like to recognize Wim Weekamp and Henk Compen for their help on tip design and manufacturing, and Ferry van der Linde for the catheter shaft development. This work was supported by FP7 OILTEBIA Grant Agreement Number 317526.

Electrifying Catheters with Light

This chapter has been published and chosen for inclusion in *OSA Spotlight* as: **Martin Pekař**, Jeannet van Rens, and Martin B. van der Mark, Electrifying Catheters with Light, *Optics Express* 25, no. 8, pp. 8534 – 8549 (2017).

Abstract

Smart minimally invasive devices face a connectivity challenge. An example is found in intracardiac echocardiography where the signal transmission and supply of power at the distal end require many thin and fragile wires in order to keep the catheter slim and flexible. We have built a fully functional bench-top prototype to demonstrate that electrical wires may be replaced by optical fibers. The prototype is immediately scalable to catheter dimensions. The absence of conductors will provide intrinsic galvanic isolation as well as radio frequency (RF) and magnetic resonance imaging (MRI) compatibility. Using optical fibers, we show signal transfer of synthetic aperture ultrasound images as well as photo-voltaic conversion to supply all electronics. The simple design utilizes only off the shelf components and holds a promise of cost effectiveness which may be pivotal for translation of these advanced devices into the clinic.

7.1 Introduction

Modern medicine aims to replace conventional diagnostic and therapeutic procedures with minimally invasive interventions^{123–125}. Reduced trauma, shorter hospital stay and reduced costs are the most important drivers for the adoption of catheter-based invasive techniques. To increase the clinical value of minimally invasive tools (ie. catheters, guide wires, sheaths), navigational or therapeutic functionality is integrated at the tip of these devices. Smart sensors or actuators in the tip require integration of electrical supply power and signal transmission, which can be challenging, in particular when high data-rate channels, consisting of many electrical wires, are needed. The large aspect ratio of diameter and length of a guide wire or catheter severely limits the total number and diameter of electrical wires that can be integrated in such a device. The integration of wires compromises bending and stiffness, the key properties for steering of the instrument. Also, the metal wires severely challenge magnetic resonance imaging (MRI) compliance and radio frequency (RF) compatibility. Last but not least, extra measures are required regarding galvanic isolation, being of crucial importance for devices that come in an intimate contact with the patient.

Indeed, smart minimally invasive devices clearly face a connectivity challenge. An example is found in intracardiac echocardiography (ICE) which is a minimally-invasive procedure used to diagnose cardiovascular conditions and to provide navigation of other instruments inside the heart^{22,25,126}. During cardiac catheterization, the catheter (a long thin tube) is inserted in an artery or vein in the groin, neck or arm and threaded through the blood vessels into the heart. This is usually done under image guidance of X-ray fluoroscopy. Unfortunately, X-ray imaging technique provides poor soft-tissue contrast and generates ionizing radiation which is harmful to both the clinician and the patient. A lot of interest has grown in recent years in the use of real-time 2-D MRI which has proven to be safe and practical while enabling completely radiation-free navigation^{127,128}. Apart from the navigation, 3-D real-time imaging of heart features and instruments is desired for a complex catheter-based cardiovascular treatments of structural heart diseases, which is difficult to achieve with the real-time MRI. Present state-of-the-art research is therefore focused on developing 3-D ICE that would be MRI safe, by replacing the conventional coaxial wires with its MRI-compatible version¹²⁹. Metallic conductors longer than 10 cm, typically used in imaging catheters, are a potential hazard in the MRI environment⁴³. The specific hazard comes from the resonance of the RF waves, which can cause temperature rise to as much as 74°C in 30s¹³⁰, but the hazard of any specific conductor is difficult to predict. Furthermore, the high bandwidth required for present day's ultrasound imaging is hardly compatible with the several meters of ultra-thin and high-loss coaxial cables necessary to keep the catheter design practical.

To overcome these challenges, fiber optics have been proposed to replace metal wires⁴¹, for example inside an active position-tracking system for catheters⁴⁴. Glass or plastic optical fibers show low magnetic susceptibility and are immune to RF interference, allowing low-noise imaging during electro-

physiologic interventions. As opposed to state-of-the-art research and striving for the highest possible level of integration, we desire to replace all conductors in an ICE catheter by a single optical fiber, therefore electrifying the device with light, and setting the path for a smarter and cost effective generation of catheters. This study reports on a fully functional bench-top demonstrator that is immediately scalable to catheter dimensions. Signal transfer of synthetic aperture ultrasound images using a VCSEL (vertical cavity surface emitting laser) and optical fiber is shown together with power transfer over optical fiber, which uses violet light and *receiving* gallium nitride LEDs (light emitting diodes) as biocompatible photo-voltaic converters^{131,132} to supply all electronics. In our proposed solution, the absence of conductors provides galvanic isolation as well as intrinsic RF and MRI compatibility and the simple design utilizing off the shelf components holds a promise of cost effectiveness all of which may help translation of these advanced devices into the clinic.

7.2 Materials and Methods

Experimental system layout

The long term objective is to build an ICE catheter where all electrical wires will be replaced by fiber optics. The intermediate step towards this goal is to provide a scalable proof of concept. To this aim a bench-top setup consisting of a several blocks is built, as shown schematically in Fig. 7.1 and on a photograph in Fig. 7.2.

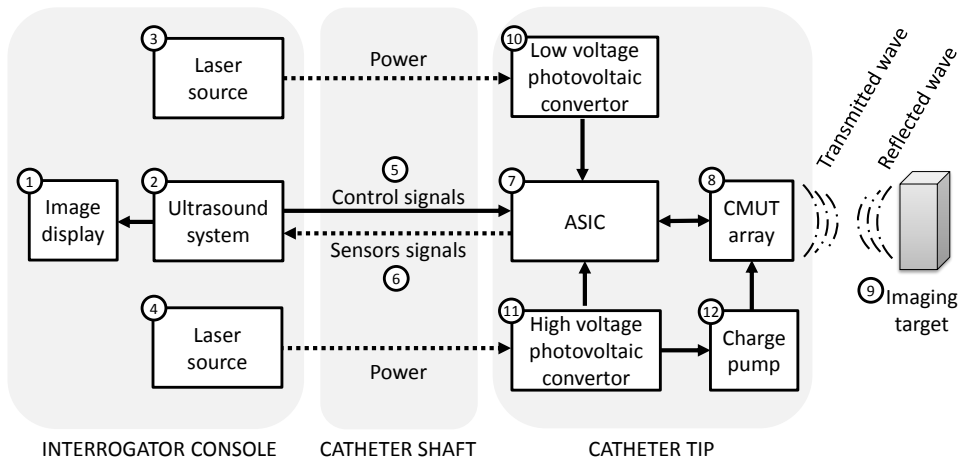


Figure 7.1: Schematics of the opto-electrical ultrasound imaging system. Electrical connections are shown as solid arrows and the optical connections are shown as dashed arrows. For comparison of system performance, the optical connections can be replaced by electrical wires. The labelled numbers correspond to the components shown in a photograph in Fig. 7.2.

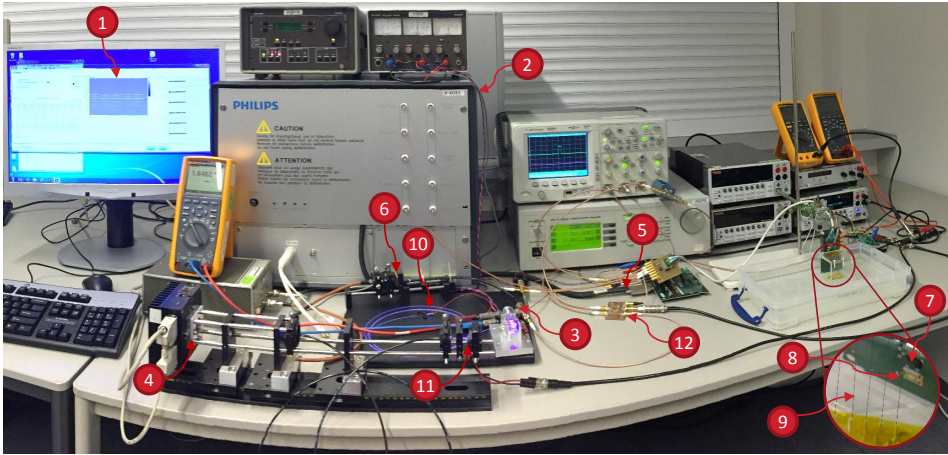


Figure 7.2: Photograph of the opto-electrical ultrasound imaging system. The labelled numbers correspond to the items shown in a schematic drawing in Fig. 7.1.

The left block, the interrogator console, contains laser sources to generate optical power and a custom ultrasound system which generates control signals. Electrical and optical connections are shown as solid and dashed arrows, respectively. The ultrasound system also performs beam-form processing of the received sensor signals, and the display shows the resulting ultrasound image.

The middle block depicts three optical fibers and a few electrical wires for transmission of the control signals connecting the left and right block. For the long term goal, one laser source with fiber can be replaced by a beam splitter at the catheter tip and the same fiber can be used as a return path using a dichroic mirror at both ends. Then, also the control signals will be sent over the same optical fiber and some receiving logic should be integrated in the catheter tip. Ultimately, only a single optical fiber will need to be integrated in the catheter shaft. This study compares system performance for electrical and optical connection and therefore the system is designed to allow replacing of the optical connections with electrical wires.

The right block comprises a capacitive micromachined ultrasonic transducer (CMUT) array, an application specific integrated circuit (ASIC), low and high voltage photo-voltaic converters, and a charge pump designed to be integrated in a catheter tip. The CMUT is immersed in water and utilized to both transmit an acoustic wave and receive the reflected echoes.

Transducer

The CMUT array is fabricated on 6-inch 670- μm thick silicon wafer utilizing a sacrificial release process^{65,72,73}. The array consists of 512 active CMUT cells, each cell has a diameter of 60 μm at a separation distance of 63.6 μm . The cells are arranged in 16 array elements, each containing 32 cells aligned in one column. The total active area is $2 \times 1 \text{ mm}^2$. The top electrodes of each array

element are wire-bonded via a printed circuit board (PCB) to the 16 channels of the ASIC. The bottom electrode is short circuit and connected to a common ground. The CMUT cells are operated in collapse-mode and require a magnitude of negative bias voltage higher than -65 V (typically -90 V) applied to the electrodes via 1 M Ω resistor. The surface of the CMUT is covered with approximately 15 μm thick layer of a silicon-like material for passivation and electrical insulation of the wirebonds. The CMUT array is mounted on the PCB without any acoustic backing layer.

ASIC

An already existing ASIC is used. It was designed to generate high voltage positive pulses to drive the CMUT cells, and it amplifies and buffers the received sensor signals. The ASIC is made by XFAB XP018 technology which provides high-voltage components based on 5 V gate-oxide transistors, that allow a maximum high-voltage swing of 60 V, which is additive to the negative bias voltage – see Fig. 7.3. The low-voltage transistors have a feature size of 0.18 μm and run at a typical supply voltage of 1.8 V.

Functionality of the ASIC is shown schematically in Fig. 7.3. The ASIC contains 16 transmitters that are capable of generating single-ended high-voltage pulses to stimulate the top electrodes of the CMUT array elements (the array columns). The ASIC also comprises 16 receivers for read-out of the elements. A multiplexer drives the low voltage stimulus signal to one of the high voltage transmitters. Another multiplexer connects one of the receivers to the signal output channel. A capacitor of 10 nF is used to decouple the high-frequency stimulus and echo-signals from the DC bias current. The amplified (26 dB) and buffered output signal is transferred from the ASIC to an ultrasound imaging system either via a 50 Ω coaxial cable or via an optical transmission link. This ASIC configuration allows generating synthetic aperture ultrasound images. The ASIC requires two external supply domains. A high-voltage supply domain which can be used at a range of 10 V – 60 V and a low-voltage supply domain of 1.8 V.

Electronic boards

The CMUT array and ASIC are mounted on a PCB, which hosts 47 nF and 100 nF capacitors connected to the common ground to stabilize the source voltage in the low and high voltage domains, respectively. The power to both high and low voltage domains is provided via a pin header connector mounted on the PCB. Bias voltage, control signals, sensor signals are connected via a 0.5 -m long cable and a JAE312 connector mounted on the PCB. The proximal end of the cable clicks on a fan-out board which connects 5 control signals (reset, TX control, RX control, TX/RX switch, transmit pulse) and the bias voltage via standard 50 Ω coaxial wires.

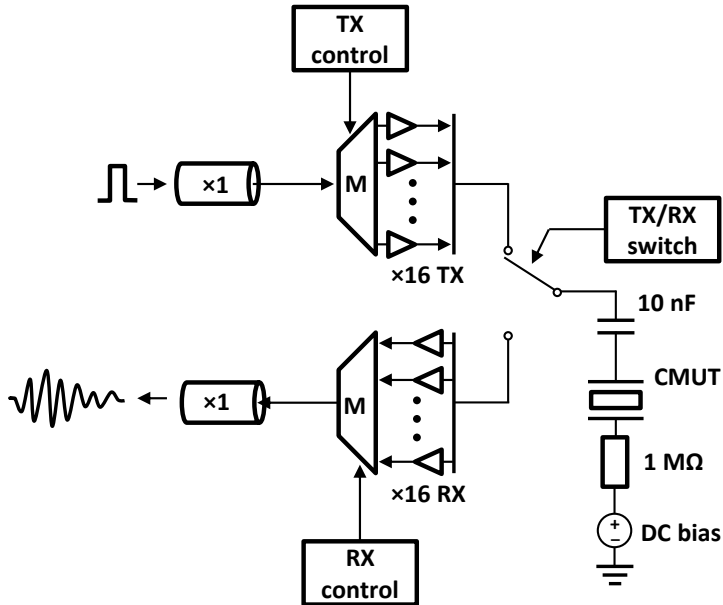


Figure 7.3: Schematic diagram of the ASIC functionality. The ASIC consists of 16 high voltage transmitters (TX), 16 receivers (RX), two multiplexers (M) controlled by the transmit (TX) and receive (RX) control signals, and a transmit-receive (TX/RX) switch which connects the ASIC to the CMUT array.

Ultrasound system

The control signals and the transmit pulse are generated by a custom high-frequency ultrasound imaging system (Philips Research, Eindhoven, the Netherlands) having a -6 dB bandwidth of 5 MHz – 50 MHz. The system is capable of driving the CMUT with arbitrary pulses defined by time increments of 5 ns. The 14-bit analogue-to-digital (AD) convertor sampling time is 5 ns. The sensor signals from the CMUT array are compensated for attenuation by TGC, 16 times averaged and stored at a local hard-drive for off-line processing before being displayed.

Signal generation and data acquisition

The ASIC is controlled via 5 signals which are generated at the pulse repetition frequency (PRF) of 2 kHz. The repetition period is divided into a transmit and receive window which define one acquisition event. Typical length of the transmit window and receive window is 2048 and 8192 samples, respectively. In total 289 $((16 + 1)^2)$ acquisition events are generated in sequential order to acquire synthetic aperture data from all combinations of 16 individual physical and one „dummy“ array element. During the dummy acquisition event, the transmit pulse is switched off and the receive remains active. A reset pulse is generated at start up, or once signals from all the elements have been received. The de-

sired transmit and receive array element is selected by applying the TX control and RX control signals in cyclical order, ie. n consecutive pulses at the transmit multiplexer selects the n^{th} array element for transmit. After the appropriate elements are chosen, the transmit-receive control signal switches the ASIC chip to transmit mode and disconnects the receive circuitry to protect it from overvoltage generated by the high-voltage pulser. An arbitrary unipolar pulse (typically 1 – 2 periods of 12 – 14 MHz) is generated in the transmit mode and the transmit-receive control signal switches the ASIC back to the receive mode. A signal having a frequency of 16 kHz is generated to seed the high-voltage bias needed for the CMUT array and will be discussed later in Sec. 7.2. All control signals are synchronized with a 200 MHz clock of the ultrasound system and have an amplitude of 1.8 V.

Image processing

A total of 289 signals are recorded, out of which 256 signals contain the ultrasound echo signal, 16 signals from the dummy transmit element are subtracted from the signals received by the corresponding element to compensate for various artifacts (e.g. unwanted echo generated by switching in between transmit and receive modes). The remaining 17 signals from the dummy receive element are not used. A synthetic transmit aperture method is utilized to form the ultrasound images¹³³. A 90° sector image is defined in a polar grid with an angular resolution of 5° and radial resolution of half the acoustic wavelength. The received signals are band-pass filtered with a linear-phase finite impulse response digital filter at a center frequency of 12 MHz and bandwidth of 6 MHz. A Hilbert transformation and a Hanning-window apodization is applied to the received signals. A beamforming algorithm finds the instantaneous envelope of the received signals at pre-defined grid points to form a low resolution image. When the width of the array element is comparable to the wavelength corresponding to the center frequency of the transmitted signal, angular dependence of the element's sensitivity has to be taken into the account by applying weights to the received signals¹³⁴. The weights are estimated by the means of a single element directivity function,

$$f(\Theta) = \frac{\sin(\pi d/\lambda \sin\Theta)}{\pi d/\lambda \sin\Theta} \cos\Theta, \quad (7.1)$$

where d is the element width and Θ is the observation angle. This is repeated for all 16 transmissions. The low resolution images are coherently added to form one high resolution image. The absolute value of the high resolution image is then visualized in a 40 dB range.

Optical signal transmission

To transfer signals from the ASIC to the ultrasound system analog modulation is applied to the vertical-cavity surface-emitting laser (VCSEL) emitting at 850 nm (ULM850-10-TT-C0104U, ULM Photonics, Ulm, Germany). The laser current is modulated in amplitude by the pre-amplified ultrasound signal via

the 4.7 nF decoupling capacitor, and Fig. 7.4 shows that the P-I characteristic of the laser is linear above threshold ($I_{th} \approx 1$ mA). Note that the I-V characteristic of the laser shown in Fig. 7.4 indicate that, above threshold, it has a (differential) impedance of approximately 50 Ω . As indicated in the electronic layout in Fig. 7.5, the effective impedance seen by the ultrasound signal is 34 Ω due to the necessary 300 Ω and 110 Ω resistors, of which the first one sets the DC bias current for the VCSEL and the latter one is required to eliminate charge build up at the ASIC's output circuit.

The modulated optical signal is focused by a lens on a photodiode (S5972, Hamamatsu, Hamamatsu City, Japan), amplified by a 20 dB amplifier (HP8447A, Hewlet-Packard, Palo Alto, CA, USA) which is connected to the ultrasound system. The electronic layout of the optical receiver is shown in Fig. 7.6. An impedance analyzer (HP8753ES, Hewlet-Packard, Palo Alto, CA, USA) is used to measure the total available bandwidth of the optical signal transmission.

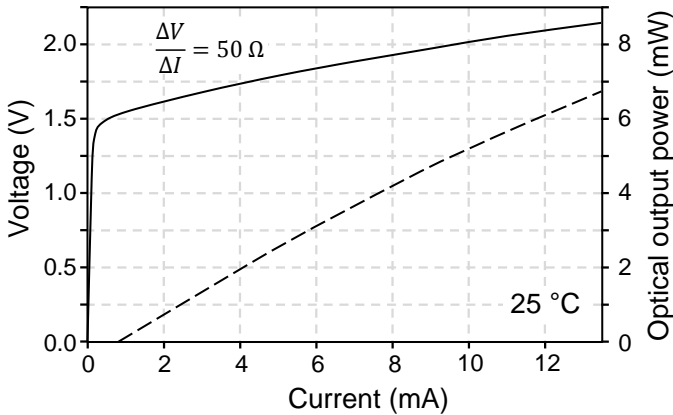


Figure 7.4: VCSEL characteristics: the current-voltage (solid) and current-power (dashed) curves.

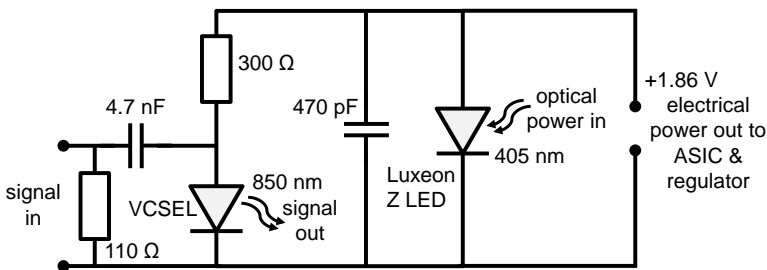


Figure 7.5: Electronic layout of the optical transmitter connected to the optical low voltage power supply.

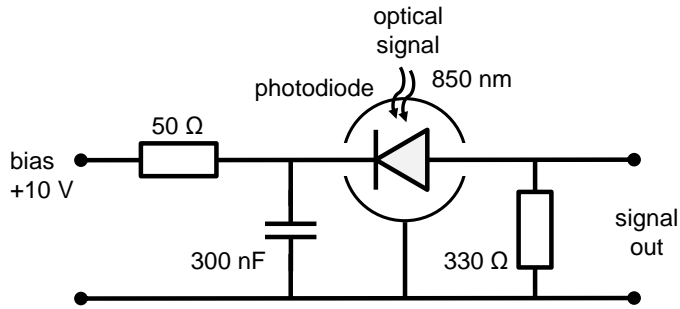


Figure 7.6: Electronic layout of the optical receiver.

Low voltage optical power

A single blue LED, type Luxeon Z Royal Blue (Philips Lumiled, San Jose, CA, USA), is used perhaps counterintuitively not as a light source but as a photovoltaic convertor to power both the low-voltage domain of the ASIC as well as to bias the VCSEL used for the optical signal transmission. The current-voltage characteristics of the LED can be found in¹³⁵. This LED is illuminated by light from a (HD-DVD or Blu-ray disc) laser (OEM) at a wavelength of 405 nm. The light from the laser is coupled via a lens and dichroic mirror (DLMP425, Thorlabs Inc, Newton, NJ, USA) into a 400- μm thick glass optical fiber (FT-400-UMT, 3M, St. Paul, MN, USA) which is in direct contact with the Luxeon Z LED. The dichroic mirror allows observing the Photo-Induced Electro Luminescence (PEL) from the LED which provides a measure for the resistive load on the LED by the electronics. The PEL signal may be used as a feedback signal to optimize the laser power¹²⁰. The optical power on the LED has been measured with a photodiode (S2386-8K, Hamamatsu, Hamamatsu City, Japan). The VCSEL is powered from the LED via the 300 Ω resistor which sets the DC bias current sufficiently above laser threshold. The measured VCSEL's bias voltage is 1.56 V.

The same LED is connected in parallel to a shunt regulator (ZR431LF01TA, Zetex, Oldham, United Kingdom) which limits the maximum current to 50 mA and stabilizes the output voltage to 1.8 V to protect the ASIC's sensitive low-voltage domain. This part has been added to protect the electronics from transients or overload while experimenting and may be omitted when a final design is implemented in the catheter tip. A wire connects the stabilized low-voltage to the PCB with the ASIC.

High voltage optical power

The Luxeon H, a 50 Volt multi-LED chip (Philips Lumiled, San Jose, CA, USA) consists of 18 monolithically integrated LEDs in series and is used as a photovoltaic convertor to power the ASIC's high voltage domain¹³⁵. The bare chip is illuminated by a high power violet laser diode (NDV7375E, Nichia, Tokushima, Japan). The light from the laser is coupled into a 1-mm thick glass

optical fiber (FT-1.0-URT, 3M, St. Paul, MN, USA) via a lens and then through a $1.5 \times 1.5 \text{ mm}^2$, 25-mm long glass mixing rod directly on the Luxeon H chip. In this way, the $1.5 \times 1.5 \text{ mm}^2$ area of the segmented LED is illuminated homogeneously and each of the segments can deliver the same current. The optical power on the Luxeon H chip has been measured with a photodiode (S2386-8K, Hamamatsu, Hamamatsu City, Japan). A coaxial wire is used to connect the Luxeon H chip to the high voltage domain of the ASIC and to the input of the charge pump. The PRF of 2 kHz and the duration of 2 periods of a 14 MHz pulse results in a duty cycle of 0.3%. Considering a 5 mW average power consumed by the ASIC pulser results in a peak power of 17.5 W. Such a peak power cannot be delivered instantaneously by the optical link. However, the calculated energy required for the pulse generation is only 2.5 μJ . This amount of energy can be stored in a 2.6 nF capacitor charged at 44 V. To account for an over-head, a 100 nF capacitor is used in the ASIC's high voltage domain to store the charge required for the generation of the transmitted pulses.

The charge pump is applied to invert and boost up the input voltage above the level required to collapse the CMUT cells (about -90 V). It utilizes the 16 kHz switch signal to charge the capacitors connected in series with the source to approximately double the input voltage. Output of the charge pump is connected to the fan-out board and then via the cable to the CMUT array.

Frequency response and image characteristics

The CMUT array is characterized in a pulse-echo experiment. Center frequency and -6 dB bandwidth of the received echo are measured per array element. Synthetic aperture ultrasound images of a wire and a tissue-mimicking cyst phantom are acquired. In both experiments, the CMUT array is connected to the optical power and signal link and, alternatively, to the conventional electrical power and signal link at the same input source voltages. The signals received with the optical and electrical power and signal link are compared. The generated images of the two phantoms are evaluated by comparison to simulations done using the Field II package^{93,136}. The images are characterized by commonly used contrast-to-noise ratio (CNR) and image signal-to-noise ratio (SNR) calculated using the following equations¹⁰³:

$$\text{CNR} = \frac{|\mu_i - \mu_o|}{\sqrt{\sigma_i^2 + \sigma_o^2}}, \quad (7.2)$$

where μ_i and μ_o are the mean signals at the same depth inside and outside the phantom feature, respectively. σ_i and σ_o are the standard deviations of signals at the same depth inside and outside the phantom feature, respectively.

$$\text{SNR} = 20 \times \log_{10} \left(\frac{\mu_i}{\sigma_o} \right). \quad (7.3)$$

Note that the simulation takes into account only the signal generated noise neglecting any thermal or quantization noise effects¹⁰⁴.

7.3 Results

Power considerations

Table 7.1 shows the measured average power consumption. The ASIC consumes, on average, 30 mW of the input power, out of which 25 mW is continuous power needed for the receive chain and 5 mW is used for generation of transmitted pulses. To account for the peak power demand of the ASIC pulser the 100 nF capacitor in the ASIC's high voltage domain is continuously recharged via the high voltage optical power link and partially discharged during the pulse generation. The low voltage ASIC domain does not exhibit any peak power demands and is therefore continuously powered by the low voltage optical link. Table 7.2 summarizes the measured efficiencies of the low and high voltage optical links.

Table 7.1: Average electrical power consumption by electronics.

		Voltage (V)	Current (mA)	Power (mW)
High voltage	ASIC pulser	44	0.106	4.7
	CMUT bias	-88.5	0	0
	Charge pump (16 kHz)	44	0.211	9.3
Low voltage	ASIC logic and amplifiers	1.86	13.3	25
	Low voltage stabilizer	1.86	1	1.9
	VCSEL	1.56	1	1.56
Total power requirements				42.5

Table 7.2: Optical power link efficiency.

	Power			Conversion efficiency (%)
	Electrical into laser (mW)	Optical on LED (mW)	Electrical from LED (mW)	
Low voltage	595	77.4	28.5	36.8
High voltage	1407	104.5	14	13.4

Signal characteristics

The bandwidth of the optical signal link is measured to be 200 MHz as shown in Fig. 7.7. The signal was filtered down to 30 MHz bandwidth to be compatible (to prevent folding) with the AD-conversion in the ultrasound receiver.

Typical pulse-echo waveforms, received by a single array element, from a wire target using the optical or electrical version of the imaging setup are compared in Fig. 7.8(a). Center frequency and bandwidth of individual transducer elements for the two versions of the setup are shown in Fig. 7.8(b) and Fig. 7.8(c), respectively.

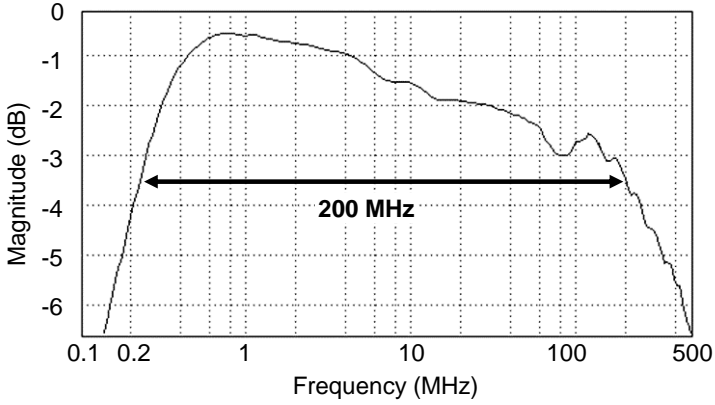


Figure 7.7: Optical signal link bandwidth.

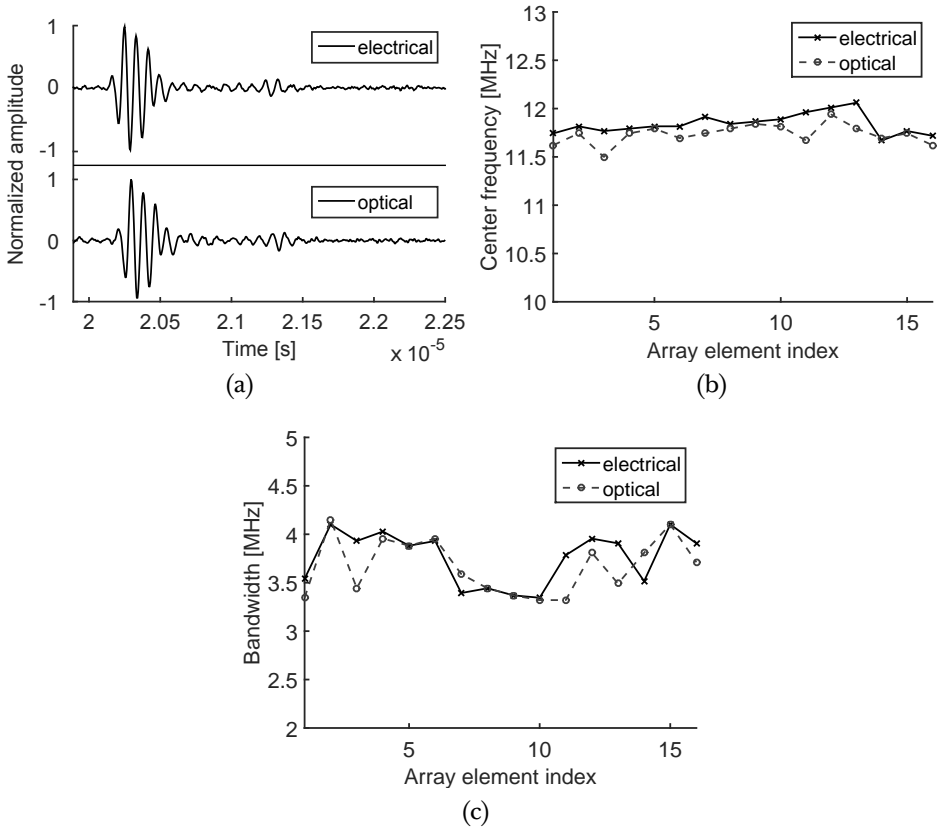


Figure 7.8: Typical pulse-echo transducer array characteristics: waveforms (a), center frequency (b), and bandwidth (c).

Imaging

Figure 7.9(a) shows a simulated synthetic aperture ultrasound image of a wire phantom generated with the designed CMUT array. The simulation is compared to images of a custom-made wire phantom obtained experimentally using the optical power and signal link, and to its electrical equivalent as shown in Fig. 7.9(e) and Fig. 7.9(c), respectively. Similarly, Figs. 7.9(b), 7.9(d) and 7.9(f) compare images of a cyst phantom. Quantitative image characteristics are summarized in Tab. 7.3.

Table 7.3: Image characteristics

	Target	Figure	CNR (-)	SNR (dB)
Simulation	wire	7.9(a)	0.5	67
Electrical link	wire	7.9(c)	0.5	50
Optical link	wire	7.9(e)	0.5	35
Simulation	cyst	7.9(b)	1.9	23
Electrical link	cyst	7.9(d)	1.6	22
Optical link	cyst	7.9(f)	1.6	22

7.4 Discussion

As shown in Fig. 7.8(a), no significant difference is observed between the waveforms acquired via the conventional electrical and the novel optical link. The array uniformity in center frequency and bandwidth is shown in Figs. 7.8(b) and 7.8(c), respectively. The frequency responses of the individual array elements are uniform. No significant differences in resonance frequency or bandwidth are observed between the CMUT powered and read-out via the optical fibers as compared to the conventional electrical wires.

Lateral resolution in the experimental images of the wire phantom (Figs. 7.9(c) and 7.9(e)) matches well with the simulation shown in Fig. 7.9(a). As compared to the simulation, axial resolution in the experimental image is compromised due to the ringing in the silicon substrate of the fabricated CMUT⁹⁴. No difference in resolution is observed between the CMUT connected to the optical power and signal link as compared to the electrical wires.

Table 7.3 summarizes the characteristics of all obtained images. The experimentally obtained image of the wire phantom (Fig. 7.9(c)) shows 17 dB lower SNR as compared to the simulation (Fig. 7.9(a)). This is because the simulation takes into account only the signal generated noise neglecting the thermal and quantization noise, which decreases the SNR in the experimental image. The image acquired with the optical link has SNR of 35 dB, which is ample for ultrasound imaging as barely any difference is observed in comparison of the images shown in Figs. 7.9(c),(e). Although the CNR definition in Eq. (7.2) is a commonly used image quality metric¹⁰³ to express the fact that detectability increases with increasing object contrast and decreasing acoustic noise, its

numerical value is highly object dependent. Therefore the CNRs of all the three images of the wire phantom are equal to a relatively low value of 0.5 as compared to the CNRs of a cyst phantom.

Figure 7.9(b) shows a simulated image of the cyst phantom exhibiting a contrast-to-noise ratio of 1.9 and SNR of 23 dB. These values are comparable to those of B-mode image of a cyst presented in the literature¹⁰³. The experimental image generated with the electrical link (Fig. 7.9(d)) shows 0.3 lower contrast-to-noise ratio and only 1 dB lower SNR than the simulation, indicating that the SNR is dominated by the signal generated noise rather than thermal or quantization noise. The dynamic range of the optical link as compared to the electrical one is very much the same as demonstrated by the identical CNR and SNR values of 1.6 and 22 dB, respectively measured in the images of the cyst phantom (Figs. 7.9(d),(f)). The experimentally obtained dynamic range of 22 dB is remarkable, given the small size of the aperture ($1 \times 2 \text{ mm}^2$) and the chosen synthetic aperture imaging method when only a single element is used in transmit and receive mode. A chirp technique or multi-element synthetic aperture imaging could be employed to further increase the SNR to the value of 40 dB typically used in medical ultrasound imaging^{133,137}.

Note that the darkening of the sector images at large angles of the cyst phantom happens due to the low element's angular sensitivity, which is a projection of its area in the given direction, a cosine of the angle, for both transmission and reception.

A reception bandwidth of 200 MHz of the ultrasound signals is achieved by utilizing amplitude modulation of a VCSEL (Fig. 7.7) and non-linear distortion is avoided by operating the VCSEL in its linear regime. The optical signal transfer does not suffer from RF-signal interference in comparison to poorly-shielded thin coaxial wires as would be the case for integration of wires in a catheter.

The optoelectronic components presented in this study will ultimately have to fit in a catheter tip and must show sufficiently low heat dissipation so that they will not harm or denature adjacent tissue or passing blood. The presented photovoltaic-conversion dissipates 139 mW of electrical power (Tab. 7.2). The reverse conversion efficiency of the low voltage LED reaches 37 % which is close to the limit of its design efficiency. The high voltage LED's efficiency is 13 %, which can be improved up to about 25 % by more homogeneous illumination of the 18 LEDs on the Luxeon H chip. The conversion efficiency can be further increased by matching the voltage requirements of the ASIC and the CMUT array to the limits of the LEDs, putting them in a more favorable working point. Also the charge pump presented here is rather inefficient and its current can be lowered by at least a factor of 10 (unpublished observation). The low voltage power dissipation of 25 mW from the ASIC is relatively high because all 16 receiver amplifiers are powered in the receive mode. This power could be lowered by factor of 16 when the ASIC is optimized for receiving with only a single amplifier. Similarly, the high voltage power dissipation can be reduced by powering only a single transmitter. Despite the possibility for optimization of the system efficiency, the amount of power dissipated in the small contact area is sufficiently low for intracardiac catheters placed typically in the flowing

blood pool of the heart. Optimization will allow reaching the limit for intravascular catheters (100 mW for a catheter of 1.8 mm in diameter¹³⁸), which have four times smaller cross-sectional area and are placed in tight coronary arteries. Then it is also possible to irrigate the catheter to lower its temperature, or a heat conducting element in the catheter tip may spread the heat load and reduce the temperature.

The reason for using a GaN device, the blue LED, as a photovoltaic converter is its high bandgap of 2.8 eV which provides a compact power source that can deliver directly up to 2.4 V. In addition to that, the LED device can handle high power density on the order of 1 W/mm², which is at least hundred times more than that of a silicon photodiode. Using the high power-density LED enables the optical solution presented in this study to be integrated in an intracardiac catheter having a typical diameter of about 3 mm.

Previous demonstration of light powering in a magnetic resonance catheter detector utilized a GaAs photovoltaic converter⁴⁴. The disadvantage of GaAs is, however, its toxicity and a low bandgap (1.1 eV), which results in a factor of two lower power density as compared to GaN. Our approach, which utilizes a non-toxic GaN LED is therefore a more appropriate solution for medical devices, in which the biocompatibility and power density is of crucial importance.

All the components have been designed with a catheter-scale miniaturization in mind. The Luxeon Z and Luxeon H chip having the package dimensions of $1.0 \times 1.0 \text{ mm}^2$ and $1.6 \times 1.6 \text{ mm}^2$, respectively, exhibit a great power density allowing its integration in a tip of an intracardiac catheter. Using a different wavelength for optical power delivery and signal transmission enables single-optical fiber integration, some of which designs have been published earlier¹³⁵. Nevertheless, the integration challenge of the individual optical components (ie. beam splitters, lenses) needs to be solved before the all-optical ICE imaging catheter can be built.

An ICE catheter is a single-use device, of which the price exceeds a few thousand Euro. Lowering the costs is therefore critical so that patients may benefit from these medical devices. Batch manufacturing possibility of CMUT, low price of the optical components, and the simple synthetic aperture ultrasound imaging technique will enable development of a low-cost ICE system^{27,91,139,140}.

The minimum time to receive echoes from a depth of 31.5 mm is 41 μs resulting in a maximum PRF of 24 kHz. Such a system would allow imaging at 83 FPS without averaging. Due to the limited bandwidth of the data stream channel the system presented in this paper achieves maximum PRF of 2 kHz, which results in a very slow frame rate considering the 16 times averaging. Therefore only images of static objects were acquired.

The presented device facilitates five low voltage control signals for the ASIC which is at odds with the all-optical concept. Re-design of the ASIC is needed to transmit all the control signals in series via a single channel. These control signals could then be transmitted via an optical signal link analogue to the one presented in this paper. Such a device would facilitate solely optical connections between the distal sensor and proximal end, thus providing total galvanic isolation (therefore eliminating the need and desire of grounding the catheter

tip), immunity to RF interference, MRI compatibility and safety.

The current design utilizes a shunt regulator to limit the maximum current and to stabilize the output voltage to protect the ASIC's sensitive low-voltage domain during the various experiments. This regulator can, however be omitted once all the design parameters are optimized and fixed, increasing the efficiency of the optical power transmission and decreasing the size of the device.

The practical data rate of a VCSEL transmitter is 10 Gbit s^{-1} which is large enough to transmit, in parallel, 16 AD-converted ultrasound signals with 40 dB dynamic range, therefore speeding up the acquisition and limiting the required number of connections within the restricted space of a catheter. To this aim of full frame imaging, the development of a small-size and low power AD-converter would be required. The measured bandwidth of the VCSEL-based optical link described in this paper is 200 MHz, which is limited by the rather bulky passive components used to match the impedance of the VCSEL to set its operating point and by the bandwidth of the amplifier connected to the photodiode. It should be noted that in our electronic design no coils or ferrites have been used anywhere and that this was done to make sure that the ultimate goal, of total miniaturization and integration in a catheter, can be met.

7.5 Conclusion

We have built a bench-top demonstrator that is scalable to catheter dimensions, in which conventional electrical wires used for ultrasound sensor-signal and power transfer are replaced by three optical fibers. We have shown photo-voltaic conversion of 405 nm light to 44 V and 1.8 V by two blue LEDs to supply all electronics. Synthetic aperture ultrasound images were acquired at a frequency of 12 MHz with a collapse-mode CMUT. Analog modulation of a 850 nm VCSEL showed 200 MHz broad-band signal transfer. System bandwidth, noise level and dynamic range are nearly identical as shown in comparison of the images acquired with the optical link and its electrical equivalent. The absence of conductors will provide galvanic isolation and intrinsic RF / MRI compatibility without any noticeable loss in the image quality. The robust and simple design holds a promise of cost effectiveness and facilitates the emerging application of (bi-directional) photo-voltaic devices with fiber-optics as a backbone of connectivity in medical catheters. These results may assist translation of such advanced devices into the clinic.

Funding

European Union Seventh Framework Programme (EU FP7) (317526); Electronic Components and Systems for European Leadership Joint Undertaking (ECSEL JU) (2014-2-662155).

Acknowledgments

The authors would like to thank the following people for their effort and support: Anneke van Dusschoten, Alfons Groenland, Nenad Mihajlovič, Walter Hermans, John Reuvers, Jim Oostveen and Peter Barendse.

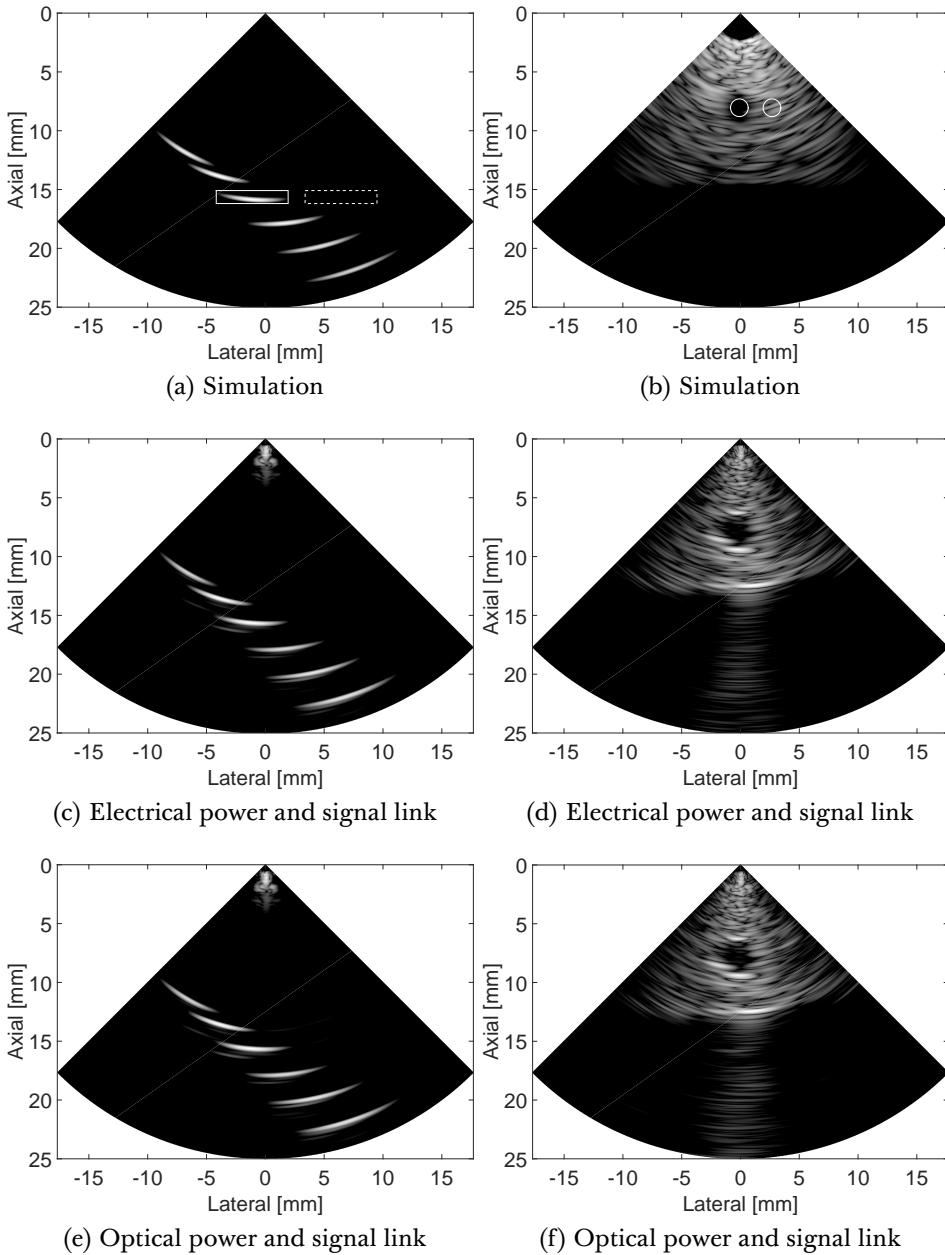


Figure 7.9: Synthetic aperture images of (a, c, e) a wire phantom and (b, d, f) a cyst phantom shown at a dynamic range of 40 dB. The white (a, c, e) rectangles and (b, d, f) circles show the region of interest inside (solid) and outside (dashed) the phantom feature used for the calculation of the image characteristics (CNR, SNR).

Overview and Conclusions

8.1 Overview

This thesis investigates two apparently unrelated novel solutions for smart intracardiac catheters – a new transducer technology that allows ultrasound frequency tuning, and an optical signal and power transmission using a light-emitting diode (LED) operated in a reverse. From an engineering point of view, smart catheters are challenging medical devices to design and manufacture. They have to be thin, long, flexible, steerable, biocompatible, safe, useful, intuitive to use, effective and all of that for an affordable price. This thesis illustrates the necessity of combining multiple disciplines, such as acoustic, optics, electronics, and clinical science to solve the challenging task of designing a novel imaging catheter that can provide valuable feedback to the clinician and therefore facilitate improvement of the patient's health.

Contribution to CMUT physics

Ultrasound technology has progressed significantly since the first intracardiac imaging experiments were done in 1960¹⁵. The idea of utilizing a large bandwidth transducers to provide an image at virtually any clinically relevant ultrasound frequency, trading image resolution with penetration depth, dates back to 1990⁸⁴. In 2006, frequency-tunability of a collapse-mode capacitive micromachined ultrasonic transducer (CMUT) was explored and quantified in electrical and acoustic measurements⁸⁹. Building upon the state-of-the-art scientific knowledge, research results presented in this thesis take the frequency-tunability of a collapse-mode CMUT a few steps further.

Modelling

An electro-mechanical, semi-analytic, reduced-order model of a fluid-loaded transmitting CMUT operated in collapse mode is developed in Chapter 2. The model requires conventional geometrical, mechanical and electrical parameters as an input and can predict membrane to voltage acceleration as well as pressure waveform at an arbitrary location in a fluidic medium. In future work, the model can be therefore coupled to an ultrasound image simulator, e.g. Field 2^{79,80,141,142}, providing a powerful tool to link the CMUT design parameters with its imaging performance.

Experiments

Experimental measurements of the fabricated CMUT prototype show that the developed model captures the collapse-mode static behaviour of a CMUT with a high accuracy and even outperforms some of the other state-of-the-art models published in literature. The dynamic, frequency-tunable behaviour of a collapse-mode CMUT is modelled with a satisfactory accuracy as validated in acoustic measurements.

Key capabilities

Transmit and transmit-receive sensitivity of a CMUT array prototype, operated for simplicity as a single element, is characterized in Chapter 3. The sensitivity measurements indicate reciprocity of the collapse-mode CMUT, which suggests that the model of a transmitting CMUT developed in Chapter 2 could potentially be used to predict the CMUT's receive behaviour too. The study shows that a collapse-mode CMUT can operate efficiently at multiple center frequencies when the driving pulse and the bias voltage are optimized.

Limitations

The simulations at different bias voltages, however, indicate that the frequency tunability comes at the cost of a waveform ringing as can be seen in comparison of the pressure waveforms acquired at the bias voltage of 120 V and 160 V. Increase in bias voltage leads to a larger contact radius, which in turn results in a higher natural resonance frequency. However, at the same time the CMUT membrane gets stressed and therefore vibrates at a reduced bandwidth. This effect is observed by an increased number of cycles in the high frequency pressure waveforms presented in Chapters 2, 3, and 4.

To protect the CMUT device from the capacitive and conductive effect of water, it needs to be coated with a passivation layer¹⁰⁷. Although this layer was not simulated and avoided in the experimental work in Chapter 2 by immersing a bare CMUT into a non-conductive oil, it was necessary for the phantom and subsequent *ex vivo* and *in vivo* investigation. The transmit-receive frequency response in the measurements presented in Chapter 3 and 4 show the undesired effect of the applied passivation layer observed as a peak at 18 MHz – 19 MHz. This peak originates from a quarter-wavelength resonance of the acoustic wave in the passivation layer, in which a thin-film interference occurs^{100,107}. The severity of this artifact could be lowered by applying a passivation material that closely matches the acoustic impedance of water. Design of such an artifact-less layer is the goal of on-going research.

The frequency spectra in Chapter 3 and 4 show a dip at a frequency of about 11 MHz – 12 MHz. At this frequency the thickness of the silicon substrate corresponds to a multiple of half the acoustic wavelength in silicon, causing an anti-resonance. The silicon substrate ringing can be suppressed by addition of a better acoustically-matched and highly attenuating backing layer or by thinning down the silicon substrate to shift its resonance frequency out of the CMUT bandwidth. The thinning approach is however only practically feasible up to a thickness of about 400 μm , because a thinner substrate lacks the robustness to support the moving CMUT membrane.

Contribution to intracardiac echocardiography

The usefulness of frequency tuning is first demonstrated in Chapter 3 in a comparison of rudimentary images at different optimal combinations of driving pulse frequency and bias voltage, acquired by linearly moving the transducer across a tissue mimicking phantom.

2-D imaging capabilities of a frequency-tunable CMUT array are fully exploited in Chapter 4. A rigid probe prototype has been built and its imaging performance was quantified in terms of resolution and penetration depth at various combinations of continuously varied bias voltage and pulse settings on a wire and a tissue-mimicking phantom. Three optimal settings giving the maximum resolution for a desired penetration depth have been identified for three distinct imaging modes, of which the imaging performance has been demonstrated.

The initial concept of frequency-tunability studied in Chapters 2 – 4 has been extended further to a clinically viable application. The frequency-tunability, forward-looking design and steerability have been identified as the three key aspects of an agile zoom-in and zoom-out imaging concept. These design aspects are combined in a single catheter prototype introduced in Chapter 5. It is found out in an *in vivo* animal study that such a combination allows visualizing intracardiac structures of various sizes *in vivo*, e.g. leaflets of the heart valves and the ventricle at different distances relative to the catheter tip, providing both wide overviews and detailed close-ups. The promising zoom-in and zoom-out concept may substantially influence the future role of forward-looking ICE in the clinical practice. Nevertheless, the potential gain in navigation efficiency of the forward-looking design, which is similar to using a flashlight, towards the specific feature of interest remains to be proven in a future study.

Solution to connectivity problem in smart catheters

The catheter prototype presented in Chapter 5 had an outer diameter of 12 Fr. This relatively large diameter was required to wirebond the CMUT array with the front-end electronics and to fit 32 coaxial wires and a several power connections inside the lumen of the catheter. Clinical practise, however, requires the diameter to be reduced to at most 10 Fr.

While the connections to the CMUT at the tip could be resolved by utilizing a monolithic integration of the CMUT with the front-end electronics, through silicon-via connections or flex-to-rigid technology, interconnecting the catheter tip the with outside world represents a though challenge^{30,114}.

A bright solution of using an all-optical fiber link, a sort of an optical USB cable for catheters, is introduced and developed in Chapter 6. The key insight obtained is that a blue LED used in a reverse absorbs up to 1 W mm^{-1} of bright violet light with high conversion efficiency up to 37 %, which makes it a unique miniature power source for catheters.

Key capabilities

It is shown that a single $1 \times 1 \text{ mm}^2$ LED illuminated by violet light can provide voltage that is ample to power CMOS electronics, and a $1.6 \times 1.6 \text{ mm}^2$ array of a several LEDs can power a high-voltage ultrasound transducer. In addition to the optical power delivery, the photo-induced electroluminescence provides a practical mean of transmitting signal from the distal catheter tip to

the proximal end via the same fiber-link. Chapter 6 introduces a pressure sensing catheter prototype with a monolithically integrated ASIC and pressure sensitive micromachined capacitive sensor to demonstrate this LED-based optical solution. The device is powered by a laser from the proximal end of the catheter and coupled via an optical fiber to an LED at the tip that serves simultaneously as a photovoltaic convertor and as a light emitter for the signal transmission, back over the same optical fiber.

The analogue signal bandwidth of the demonstrator built in Chapter 6 was limited by capacitance of the LED to about 500 kHz, which is not sufficient for a megahertz ultrasound sensor signal transmission. The problem is solved by utilizing a VCSEL (vertical-cavity surface-emitting laser, commonly used in telecommunications) instead of the LED. In contrast to the traditional utilization of VCSEL for digital communication (10 Gbit s^{-1}), it was found that analog modulation can provide broad-band signal transmission up to at least 200 MHz. Such bandwidth is sufficient to demonstrate ultrasound imaging at a frequency range of 5 MHz – 60 MHz, which is used in intracardiac echocardiography. Nevertheless, the transmission bandwidth could be increased to its theoretical limit of 10 GHz by eliminating the rather bulky passive components used to match the impedance of the VCSEL to set its operating point.

Imaging with all-optical fiber link

The potential of the power and signal fiber link solution is exploited further for ultrasound imaging in Chapter 7. A bench-top demonstrator scalable to catheter dimensions is built, in which three electrical wires are replaced by three optical fibers. A synthetic aperture ultrasound images acquired at center frequency of 12 MHz (4 MHz bandwidth) with the optical fiber link were compared to a conventional acquisition via electrical wires. Nearly equivalent system bandwidth, noise level and dynamic range was found, which proves feasibility of the optical link for ultrasound imaging. Even though only three wires have been replaced by three optical fibers for simplicity, future implementations of the optical link could facilitate transmission of hundreds of signals by only a few optical fibers.

Limitations and recommendations

In Chapter 7, a readily available CMUT not optimized for efficiency was used. It required large voltage amplitudes challenging the design of the optical power link. Collapse mode simulations suggest a new generation of CMUTs generating pressure of 4 MPa and requiring a bias voltage of less than 10 V⁵⁹. These low voltage CMUT designs will allow using a small single LED chip to power both the CMUT, VCSEL and the front-end electronics (ASIC), enormously simplifying the optical power link and reducing the size factor. Nevertheless, a small and efficient charging pump, preferably integrated within the ASIC, may still be required to bias the CMUT to a collapse state.

Compared to the state-of-the-art electrical wiring, the all-optical fiber link for power and signal transmission is very promising. The absence of conduc-

tors provides intrinsic galvanic isolation, MRI compatibility and RF-free interference. The optical solution allows for slender devices with good deflectability, robustness, high level of integration and simple assembly, all of which may make these smart disposable devices affordable and therefore facilitate their translation into the clinic.

Future prospects

Once the frequency tunable, forward-looking, steerable catheter takes the full-advantage of the all-optical fiber link connection, an ultimate ICE catheter will be brought forth. Such catheter will have smaller diameter and could perhaps feature a 3-D imaging capability. It could be brought into the right heart to guide transseptal puncture and then moved forward to the left side of the heart. There, while being switched to the high-resolution zoom-in mode, it could monitor in real-time for thrombus formation, left atrial appendage (LAA) anatomy, mitral valve functionality, or assist by a pulmonary artery ablation. The zoom-out mode could be useful for global orientation and navigation inside the heart, monitoring for pericardial effusion, or prosthetic valve and closure device placement as well as verification of their functionality. Although this thesis investigated *in vivo* only the zoom-in and zoom-out imaging of an aortic valve, there are many more clinical applications that remain to be researched.

In prospect, the frequency Agile ultrasound imaging and the Bright optical link solution for Catheters presented in this thesis may be the ABCs of future intracardiac ultrasound imaging.

8.2 Conclusions

- A semi-analytic, reduced-order model of fluid-coupled thin annular plates captures the static, dynamic and frequency-tunable behaviour of a collapse-mode CMUT (Chapter 2).
- A CMUT cell within an array exhibits a shorter response and a broader bandwidth as compared to a detached single CMUT cell, because of the mutual radiation forces damping the motion of the CMUT plates (Chapter 2).
- Collapse-mode CMUT is a reliable, reciprocal and frequency-tunable imaging device (Chapter 3).
- Passivation layer and silicon substrate cause artifacts in the frequency response of a CMUT device (Chapter 3).
- Different combinations of bias voltage and driving pulses allows high penetration or high resolution 2-D imaging in a single device (Chapter 4).
- The key combination of forward-looking design, frequency-tunability and steerability enables a new zoom-in and zoom-out intracardiac imaging concept (Chapter 5).

- A blue LED used in a reverse enables simultaneous optical power delivery and signal transmission for catheters using a single all-optical fiber link (Chapter 6).
- Fiber-optics and LEDs or a VCSEL can replace electrical wires in intracardiac echocardiography catheters without any noticeable loss in ultrasound image quality (Chapter 7).

References

- [1] Dariush Mozaffarian, Emelia J Benjamin, Alan S Go, Donna K Arnett, Michael J Blaha, Mary Cushman, Sandeep R Das, Sarah de Ferranti, Jean-Pierre Després, Heather J Fullerton, Virginia J Howard, Mark D Huffman, Carmen R Isasi, Monik C Jiménez, Suzanne E Judd, Brett M Kissela, Judith H Lichtman, Lynda D Lisabeth, Simin Liu, Rachel H Mackey, David J Magid, Darren K McGuire, Emile R Mohler, Claudia S Moy, Paul Muntner, Michael E Mussolino, Khurram Nasir, Robert W Neumar, Graham Nichol, Latha Palaniappan, Dilip K Pandey, Mathew J Reeves, Carlos J Rodriguez, Wayne Rosamond, Paul D Sorlie, Joel Stein, Amytis Towfighi, Tanya N Turan, Salim S Virani, Daniel Woo, Robert W Yeh, and Melanie B Turner. Executive Summary: Heart Disease and Stroke Statistics—2016 Update. *Circulation*, 133(4):447–454, 2016.
- [2] Brian Olshansky, Mina K Chung, Steven M Pogwizd, and Nora Goldschlager. *Arrhythmia Essentials*. Elsevier Health Sciences, 2016.
- [3] John P Veinot, Phillip J Harrity, Federico Gentile, Bijoy K Khandheria, Kent R Bailey, Jeffrey T Eickholt, James B Seward, A Jamil Tajik, and William D Edwards. Anatomy of the Normal Left Atrial Appendage. *Circulation*, 96(9):3112 – 3115, 1997.
- [4] Joseph L Blackshear and John A Odell. Appendage obliteration to reduce stroke in cardiac surgical patients with atrial fibrillation. *The Annals of thoracic surgery*, 61(2):755–9, 1996.
- [5] K Chatterjee and E J Topol. *Cardiac Drugs*. Jaypee Brothers, Medical Publishers Pvt. Limited, 2015.
- [6] David R Holmes, Vivek Y Reddy, Zoltan G Turi, Shephal K Doshi, Horst Sievert, Maurice Buchbinder, Christopher M Mullin, and Peter Sick. Percutaneous closure of the left atrial appendage versus warfarin therapy for prevention of stroke in patients with atrial fibrillation: a randomised non-inferiority trial. *Lancet*, 374(9689):534–42, 2009.
- [7] Craig T. January, L. Samuel Wann, Joseph S. Alpert, Hugh Calkins, Joaquin E. Cigarroa, Joseph C. Cleveland, Jamie B. Conti, Patrick T. Ellinor, Michael D. Ezekowitz, Michael E. Field, Katherine T. Murray, Ralph L. Sacco, William G. Stevenson, Patrick J. Tchou, Cynthia M. Tracy, and Clyde W. Yancy. 2014 AHA/ACC/HRS guideline for the management of patients with atrial fibrillation: A report of the American college of Cardiology/American heart association task force on practice guidelines and the heart rhythm society. *Journal of the American College of Cardiology*, 64(21):e1–e76, 2014.
- [8] William H Maisel. Left Atrial Appendage Occlusion — Closure or Just the Beginning? *The New England Journal of Medicine*, 360(25):2601–2603, 2009.
- [9] J Kautzner and P Peichl. Intracardiac echocardiography in electrophysiology. *Herzschrittmachertherapie & Elektrophysiologie*, 18(3):140–6, 2007.
- [10] J D Carroll and J G Webb. *Structural Heart Disease Interventions*. Lippincott Williams & Wilkins, 2012.
- [11] Alan S. Go, Dariush Mozaffarian, Veronique L. Roger, Emelia J. Benjamin, Jarett D. Berry, William B. Borden, Dawn M. Bravata, Shifan Dai, Earl S. Ford, Caroline S. Fox, Sheila Franco, Heather J. Fullerton, Cathleen Gillespie, Susan M. Hailpern, John A. Heit, Virginia J. Howard, Mark D. Huffman, Brett M. Kissela, Steven J. Kittner, Daniel T. Lackland, Judith H. Lichtman, Lynda D. Lisabeth, David Magid, Gregory M. Marcus, Ariane Marelli, David B. Matchar, Darren K. McGuire, Emile R. Mohler, Claudia S. Moy, Michael E. Mussolino, Graham Nichol, Nina P. Paynter, Pamela J. Schreiner, Paul D. Sorlie, Joel Stein, Tanya N. Turan, Salim S. Virani, Nathan D. Wong, Daniel Woo, and Melanie B. Turner. Heart disease and stroke statistics - 2013 update: A Report from the American Heart Association. *Circulation*, 127(1), 2013.
- [12] Thomas Bartel, Silvana Müller, Angelo Biviano, and Rebecca T. Hahn. Why is intracardiac echocardiography helpful? Benefits, costs, and how to learn. *European Heart Journal*, 35(2): 69–76, 2014.
- [13] Sandhya Nalmas, Rangadham Nagarakanti, Jihad Slim, Elfatih Abter, and Eliahu Bishburg. Electrocardiographic changes in infectious diseases. *Hospital Physician*, 43(9):15, 2007.

- [14] D G Karalis, R C Bansal, A J Hauck, J J Ross Jr., P M Applegate, K R Jutzy, G S Mintz, and K Chandrasekaran. Transesophageal echocardiographic recognition of subaortic complications in aortic valve endocarditis. Clinical and surgical implications. *Circulation*, 86(2):353–362, 1992.
- [15] T Cieszyński. Intracardiac method for the investigation of structure of the heart with the aid of ultrasonics. *Archivum Immunologiae et Therapiae Experimentalis*, 8:551, 1960.
- [16] S Kimoto, R Omoto, M Tsunemoto, T Muroi, K Atsumi, and R Uchida. Ultrasonic Tomography of the Liver and Detection of Heart Atrial Septal Defect with the Aid of Ultrasonic Intravenous Probes. *Ultrasonics*, 2:82–86, 1964.
- [17] N. Bom, C. T. Lancée, and F. C. Van Egmond. An ultrasonic intracardiac scanner. *Ultrasonics*, 10(2):72–76, 1972.
- [18] James B. Seward, Douglas L. Packer, Rodrigo C. Chan, Michael Curley, and A. Jamil Tajik. Ultrasound Cardioscopy: Embarking on a New Journey. *Mayo Clinic Proceedings*, 71(7):629–635, 1996.
- [19] Acuson Files for 510(k) Clearance With the FDA for the AcuNav(TM) Diagnostic Ultrasound Catheter That Captures Images From Inside the Heart, 1999.
- [20] Kentaro Shibayama and Hiroyuki Watanabe. Clinical use of echocardiography in structural heart disease. *General Thoracic and Cardiovascular Surgery*, 64(7):365–372, 2016.
- [21] Nicola Vitulano, Vincenzo Pazzano, Gemma Pelargonio, and Maria Lucia Narducci. Technology update: Intracardiac echocardiography – A review of the literature. *Medical Devices: Evidence and Research*, 8:231–239, 2015.
- [22] Thomas Bartel, Nikolaos Bonaros, Ludwig Müller, Guy Friedrich, Michael Grimm, Corinna Velik-Salchner, Gudrun Feuchtner, Florian Pedross, and Silvana Müller. Intracardiac echocardiography: a new guiding tool for transcatheter aortic valve replacement. *Journal of the American Society of Echocardiography*, 24(9):966–75, 2011.
- [23] Antonio Dello Russo, Eleonora Russo, Gaetano Fassini, and Michela Casella. Role of Intracardiac Echocardiography in Atrial Fibrillation Ablation. *Journal of Atrial Fibrillation*, 5(6):118–135, 2013.
- [24] Douglas N Stephens, Uyen T. Truong, Amin Nikoozadeh, Ömer Oralkan, Chi Hyung Seo, Jonathan Cannata, Aaron Dentinger, Kai Thomenius, Alan de la Rama, Tho Nguyen, Feng Lin, Pierre Khuri-Yakub, Aman Mahajan, Kalyanam Shivkumar, Matt O’Donnell, and David J Sahn. First In Vivo Use of a Capacitive Micromachined Ultrasound Transducer Array – Based Imaging and Ablation Catheter. *Journal of Ultrasound in Medicine*, 31:247–256, 2012.
- [25] Ziyad M Hijazi, Kalyanam Shivkumar, and David J Sahn. Intracardiac echocardiography during interventional and electrophysiological cardiac catheterization. *Circulation*, 119(4):587–96, 2009.
- [26] Akifumi Sako, Kazunari Ishida, Makoto Fukada, Katsunori Asafusa, Shuzou Sano, and Mikio Izumi. Development of Ultrasonic Transducer “Mappie” with cMUT Technology. *MEDIX*, 51:31–34, 2009.
- [27] I Ladabaum, X Jin, H T Soh, A Atalar, and B T Khuri-Yakub. Surface micromachined capacitive ultrasonic transducers. *IEEE Transactions on Ultrasonics, Ferroelectrics and Frequency Control*, 45(3):678–90, 1998.
- [28] Ömer Oralkan, A Sanlı Ergun, Jeremy A Johnson, Mustafa Karaman, Utkan Demirci, Kam-biz Kaviani, Thomas H Lee, and Butrus T Khuri-yakub. Transducers : Next-Generation Arrays for Acoustic Imaging ? *IEEE Transactions on Ultrasonics, Ferroelectrics, and Frequency Control*, 49(11):1596–1610, 2002.
- [29] Utkan Demirci, Arif S Ergun, Omrer Oralkan, Mustafa Karaman, and Butrus T Khuri-Yakub. Forward-viewing CMUT arrays for medical imaging. *IEEE Transactions on Ultrasonics, Ferroelectrics, and Frequency Control*, 51(7):887–95, 2004.
- [30] Butrus T Khuri-Yakub and Ömer Oralkan. Capacitive micromachined ultrasonic transducers for medical imaging and therapy. *Journal of Micromechanics and Microengineering*, 21(5):54004–54014, 2011.
- [31] Gokce Gurun, Coskun Tekes, Jaime Zahorian, Toby Xu, Sarp Satir, Mustafa Karaman, Jennifer Hasler, and F Levent Degertekin. Single-chip CMUT-on-CMOS front-end system for real-time volumetric IVUS and ICE imaging. *IEEE Transactions on Ultrasonics, Ferroelectrics, and Frequency Control*, 61(2):239–250, 2014.

- [32] Danhua Zhao, Steve Zhuang, and Lee Weng. One-Probe Solution in Medical Ultrasound Imaging with CMUT Technology. In *Proceedings - IEEE Ultrasonics Symposium*, Tours, 2016. IEEE.
- [33] Mitul B. Kadakia, Frank E. Silvestry, and Howard C. Herrmann. Intracardiac echocardiography-guided transcatheter aortic valve replacement. *Catheterization and Cardiovascular Interventions*, 85(3):497–501, 2015.
- [34] David E. Dausch, John B. Castellucci, Kristin H. Gilchrist, James B. Carlson, Stephen D. Hall, and Olaf T. von Ramm. Live volumetric imaging (LVI) intracardiac ultrasound catheter. *Cardiovascular Revascularization Medicine*, 14(3):157–159, 2013.
- [35] Intracardiac Echocardiography and Ultrasound Catheter. *Advances in Catheter-Based Ultrasound Imaging. IEEE*, pages 669–678, 2005.
- [36] Hendrik J. Vos, Bas M. van Dalen, Ilkka Heinonen, Johan G. Bosch, Oana Sorop, Dirk J. Duncker, Antonius F.W. van der Steen, and Nico de Jong. Cardiac Shear Wave Velocity Detection in the Porcine Heart. *Ultrasound in Medicine & Biology*, 43(4):753–764, 2017.
- [37] Wojciech Kwiecinski, Jean Provost, Rémi Dubois, Frédéric Sacher, Michel Haïssaguerre, Mathieu Legros, An Nguyen-Dinh, Rémi Dufait, Mickaël Tanter, and Mathieu Pernot. Quantitative evaluation of atrial radio frequency ablation using intracardiac shear-wave elastography. *Medical Physics*, 41(11), 2014.
- [38] J Provost. *Electromechanical wave imaging*. Dissertation thesis, Columbia University, 2012.
- [39] Henning Braunisch, James E. Jaussi, and Jason A. Mix. High-Speed Flex Chip-to-Chip Interconnect Henning. In *IEEE Electrical Performance of Electronic Packaging High-Speed*, pages 273–276. IEEE, 2006.
- [40] E Iannone. *Telecommunication Networks*. Devices, Circuits, and Systems. CRC Press, 2016.
- [41] Andrew Alduino and Mario Paniccia. Wiring electronics with light. *Nature Photonics*, 1(3):153–155, 2007.
- [42] Gabriel Montaldo, Mickaël Tanter, Jérémy Bercoff, Nicolas Benech, and Mathias Fink. Coherent plane-wave compounding for very high frame rate ultrasonography and transient elastography. *IEEE Transactions on Ultrasonics, Ferroelectrics, and Frequency Control*, 56(3):489–506, 2009.
- [43] MK Konings, S Weiss, and CJG Bakker. Catheters and guidewires in interventional MRI: problems and solutions. *Medica Mundi*, 45(1):31–39, 2001.
- [44] Stephan Fandrey, Steffen Weiss, and Jörg Müller. A novel active MR probe using a miniaturized optical link for a 1.5-T MRI scanner. *Magnetic Resonance in Medicine*, 67(1):148–55, 2012.
- [45] Byung-Gil Jeong, Dong-Kyun Kim, Seog-Woo Hong, Seok-Whan Chung, and Hyung-Jae Shin. Performance and reliability of new CMUT design with improved efficiency. *Sensors and Actuators, A: Physical*, 199:325–333, 2013.
- [46] Tahereh Arezoo Emadi and Douglas Andrew Buchanan. A novel 6x6 element MEMS capacitive ultrasonic transducer with multiple moving membranes for high performance imaging applications. *Sensors and Actuators, A: Physical*, 222:309–313, 2014.
- [47] Alessandro Stuart Savoia, Giosuè Calianov, and Massimo Pappalardo. A CMUT probe for medical ultrasonography: from microfabrication to system integration. *IEEE Transactions on Ultrasonics, Ferroelectrics, and Frequency Control*, 59(6):1127–38, 2012.
- [48] K. K. Park, O. Oralkan, and B. T. Khuri-Yakub. Comparison of conventional and collapse-mode CMUT in 1-D array configuration. In *Proceedings - IEEE Ultrasonics Symposium*, pages 1000–1003. IEEE, 2011.
- [49] Cyril Meynier, Franck Teston, and Dominique Certon. A multiscale model for array of capacitive micromachined ultrasonic transducers. *The Journal of the Acoustical Society of America*, 128(5):2549–2561, 2010.
- [50] R. M C Mestrom, R. H B Fey, K. L. Phan, and H. Nijmeijer. Simulations and experiments of hardening and softening resonances in a clamped-clamped beam MEMS resonator. *Sensors and Actuators, A: Physical*, 162(2):225–234, 2010.
- [51] Nicolas Ségond, Dominique Certon, Jean Edouard Bernard, and Franck Teston. Characterization of cMUT by dynamic holography microscopy. *Proceedings - IEEE Ultrasonics Symposium*, pages 2205–2208, 2009.
- [52] Laura Ruzziconi, Stefano Lenci, Laura Ruzziconi, Abdallah H. Ramini, and Mohammad I. Younis. Theoretical prediction of experimental jump and pull-in dynamics in a MEMS sensor. *Sensors (Switzerland)*, 14(9):17089–17111, 2014.

- [53] Baris Bayram, Edward Hæggröm, Goksen G. Yaralioglu, and Butrus T. Khuri-Yakub. A new regime for operating capacitive micromachined ultrasonic transducers. *IEEE Transactions on Ultrasonics, Ferroelectrics, and Frequency Control*, 50(9):1184–1190, 2003.
- [54] Baris Bayram, Mario Kupnik, Goksen G. Yaralioglu, Ömer Oralkan, Arif Sanli Ergun, Der Song Lin, Serena H. Wong, and Butrus T. Khuri-Yakub. Finite element modeling and experimental characterization of crosstalk in 1-D CMUT arrays. *IEEE Transactions on Ultrasonics, Ferroelectrics, and Frequency Control*, 54(2):418–429, 2007.
- [55] Selim Olcum, F. Yalcin Yamaner, Ayhan Bozkurt, and Abdullah Atalar. Deep-collapse operation of capacitive micromachined ultrasonic transducers. *IEEE Transactions on Ultrasonics, Ferroelectrics, and Frequency Control*, 58(11):2475–2483, 2011.
- [56] Amin Nikoozadeh, B. Bayram, G.G. Yaralioglu, and B.T. Khuri-Yakub. Analytical calculation of collapse voltage of CMUT membrane. *IEEE Ultrasonics Symposium, 2004*, 1(c):256–259, 2004.
- [57] Cyril Meynier, Franck Teston, Edgard Jeanne, Jean Edouard Bernard, and Dominique Certon. Combined finite difference - Lumped modelling of fluid loaded Cmut arrays. *Physics Procedia*, 3(1):1017–1023, 2010.
- [58] Elif Aydođdu, Alper Ozguruk, Abdullah Atalar, and Hayrettin Köymen. Parametric non-linear lumped element model for circular CMUTs in collapsed mode. *IEEE Transactions on Ultrasonics, Ferroelectrics and Frequency Control*, 61(1):173–81, 2014.
- [59] Selim Olcum, F. Y. Yamaner, A. Bozkurt, H. Köymen, and A. Atalar. An equivalent circuit model for transmitting capacitive micromachined ultrasonic transducers in collapse mode. *IEEE Transactions on Ultrasonics, Ferroelectrics, and Frequency Control*, 58(7):1468–77, 2011.
- [60] Nicolas Sénépond, Audren Boulmé, Camille Plag, Franck Teston, and Dominique Certon. Fast time-domain modeling of fluid-coupled cMUT cells: From the single cell to the 1-D linear array element. *IEEE Transactions on Ultrasonics, Ferroelectrics, and Frequency Control*, 60(7):1505–1518, 2013.
- [61] B Bayram, E Haeggstrom, A S Ergun, G G Yaralioglu, and B T Khuri-Yakub. Dynamic analysis of CMUTs in different regimes of operation. *IEEE Symposium on Ultrasonics, 2003*, 1: 481–484, 2003.
- [62] Gregory W Vogl and Ali H Nayfeh. A reduced-order model for electrically actuated clamped circular plates. *Journal of Micromechanics and Microengineering*, 15(4):684, 2005.
- [63] Lior Medina, Rivka Gilat, and Slava Krylov. Bistable behavior of electrostatically actuated initially curved micro plate. *Sensors and Actuators, A: Physical*, 248:193–198, 2016.
- [64] Leonard Meirovitch. *Fundamentals of Vibrations*. McGraw-Hill, New York, 2001.
- [65] Martin Pekař, Wendy U. Dittmer, Nenad Mihajlović, Gijs van Soest, and Nico de Jong. Frequency Tuning of Collapse-Mode Capacitive Micromachined Ultrasonic Transducer. *Ultrasonics*, 74:144–152, 2017.
- [66] W Merlijn van Spengen, Robert Puers, and Ingrid De Wolf. A physical model to predict stiction in MEMS. *Journal of Micromechanics and Microengineering*, 12(5):702, 2002.
- [67] Mathias Engholm, Thomas Pedersen, and Erik Vilain Thomsen. Modeling of plates with multiple anisotropic layers and residual stress. *Sensors and Actuators, A: Physical*, 240:70–79, 2016.
- [68] Ali Nayfeh, Mohammad Younis, and Eihab Abdel-Rahman. Reduced-Order Models for MEMS Applications. *Nonlinear Dynamics*, 41:211–236, 2005.
- [69] A W Leissa. *Vibration of Plates*. NASA SP. Scientific and Technical Information Division, National Aeronautics and Space Administration, 1969.
- [70] Kwan Kyu Park and Brutus T Khuri-Yakub. Dynamic response of an array of flexural plates in acoustic medium. *The Journal of the Acoustical Society of America*, 132(4):2292–303, 2012.
- [71] Sarp Satir, Jaime Zahorian, and F. Levent Degertekin. A large-signal model for CMUT arrays with arbitrary membrane geometry operating in non-collapsed mode. *IEEE Transactions on Ultrasonics, Ferroelectrics, and Frequency Control*, 60(11):2426–2439, 2013.
- [72] Arif S. Ergun, Goksen G. Yaralioglu, and Butrus T. Khuri-Yakub. Capacitive Micromachined Ultrasonic Transducers: Theory and Technology. *Journal of Aerospace Engineering*, 16(2):76–84, 2003.
- [73] Johan H Klootwijk, Peter Dirksen, Marcel Mulder, and Elisabeth M L Moonen. Capacitive Micromachine Ultrasound Transducer. Patent US2011163630 (A1), 2011.
- [74] Yongli Huang, Edward O. Hæggröm, Xuefeng Zhuang, Arif S. Ergun, and Butrus T. Khuri-Yakub. A solution to the charging problems in capacitive micromachined ultrasonic

- transducers. *IEEE Transactions on Ultrasonics, Ferroelectrics, and Frequency Control*, 52(4):578–580, 2005.
- [75] Martin Pekař, Nenad Mihajlović, Harm Belt, Alexander F. Kolen, Jeannet van Rens, Frank Budzelaar, Bas Jacobs, Johan G. Bosch, Hendrik J. Vos, Antonius F.W. van der Steen, and Debbie Rem-Bronneberg. Frequency-Agility of Collapse-Mode 1-D CMUT Array. In *Proceedings - IEEE Ultrasonics Symposium*, Tours, 2016. IEEE.
- [76] Elif Aydogdu. *Lumped Element Modeling of Circular CMUT in Collapsed Mode*. PhD thesis, Bilkent University, 2014.
- [77] Alessandro Caronti, Alessandro Savoia, Giosuè Caliano, and Massimo Pappalardo. Acoustic coupling in capacitive microfabricated ultrasonic transducers: modeling and experiments. *IEEE Transactions on Ultrasonics, Ferroelectrics, and Frequency Control*, 52(12):2220–2234, 2005.
- [78] M. Thränhardt, P. C. Eccardt, H. Mooshofer, and P. Hauptmann. A resonant CMUT-based fluid sensor: Modeling and simulation. *Sensors and Actuators, A: Physical*, 156(1):191–195, 2009.
- [79] Jørgen Arendt Jensen and Niels Bruun Svendsen. Calculation of pressure fields from arbitrarily shaped, apodized, and excited ultrasound transducers. *Ultrasonics, Ferroelectrics, and Frequency Control, IEEE Transactions on*, 39(2):262–267, 1992.
- [80] D Bäck, Ö Oralkan, M Kupnik, M Willatzen, B T Khuri-Yakub, and J A Jensen. Simulating CMUTs using Field II. in *Proc. IEEE Ultrasonics Symposium*, pages 439–442, 2010.
- [81] G. Pećanac, T. Bause, and J. Malzbender. Ring-on-ring testing of thin, curved bi-layered materials. *Journal of the European Ceramic Society*, 31(12):2037–2042, 2011.
- [82] Josefina Ballarre, Damián A. López, and Ana L. Cavalieri. Nano-indentation of hybrid silica coatings on surgical grade stainless steel. *Thin Solid Films*, 516(6):1082–1087, 2008.
- [83] Thomas L Szabo. *Diagnostic Ultrasound Imaging: Inside Out*. Elsevier Academic Press, 2004.
- [84] Qjan Zhang and Peter A. Lewin. PVDF polymers: Imaging transducers and ultrasonic hydrophone probes. *Ferroelectrics*, 171(1):381–403, 1995.
- [85] F. Stuart Foster, Kasia A. Harasiewicz, and Michael D. Sherar. A history of medical and biological imaging with polyvinylidene fluoride (PVDF) transducers. *IEEE Transactions on Ultrasonics, Ferroelectrics, and Frequency Control*, 47(6):1363–1371, 2000.
- [86] Kwan Kyu Park, Ömer Oralkan, and Butrus T Khuri-Yakub. A comparison between conventional and collapse-mode capacitive micromachined ultrasonic transducers in 10-MHz 1-D arrays. *IEEE Transactions on Ultrasonics, Ferroelectrics, and Frequency Control*, 60(6):1245–1255, 2013.
- [87] Mette Funding la Cour, Thomas Lehrmann Christiansen, Jorgen Arendt Jensen, and Erik Vilain Thomsen. Electrostatic Analysis of CMUTs with Circular and Square Anisotropic Plates. *IEEE Transactions on Ultrasonics, Ferroelectrics and Frequency Control*, pages 1–13, 2014.
- [88] Dieter K Schroder. *Semiconductor material and device characterization*. John Wiley & Sons, 2006.
- [89] Ömer Oralkan, Baris Bayram, Goksen G Yaralioglu, A. Sanli Ergun, Mario Kupnik, David T Yeh, Ira O Wygant, and Butrus T Khuri-Yakub. Experimental characterization of collapse-mode CMUT operation. *IEEE Transactions on Ultrasonics, Ferroelectrics, and Frequency Control*, 53(8):1513–23, 2006.
- [90] David T. Yeh, Ömer Oralkan, Ira O. Wygant, Matthew O’Donnell, and Butrus T. Khuri-Yakub. 3-D Ultrasound Imaging Using a Forward-Looking CMUT Ring Array for Intravascular / Intracardiac Applications. *IEEE Transactions on Ultrasonics, Ferroelectrics, and Frequency Control*, 53(6):1202–1211, 2006.
- [91] Cornelius T. Leondes, editor. *MEMS/NEMS Handbook: Techniques and Applications*. Springer US, 2007.
- [92] Chong-Ping Chang. MEMS for telecommunications: devices and reliability. In *Custom Integrated Circuits Conference, 2003. Proceedings of the IEEE 2003*, pages 199–206. IEEE, 2003.
- [93] Jorgen Arendt Jensen. Field: A program for simulating ultrasound systems. *Medical & Biological Engineering & Computing*, 34(1):351–353, 1996.
- [94] Igal Ladabaum, Paul Wagner, Claudio Zanelli, John Mould, Paul Reynolds, and Greg Wojcik. Silicon substrate ringing in microfabricated ultrasonic transducers. In *Proceedings - IEEE Ultrasonics Symposium*, pages 943–946, 2000.
- [95] Sigrid Berg. *Capacitive micromachined ultrasonic transducers: Acoustic challenges and proposed solutions*. PhD thesis, NTNU - Trondheim, 2012.
- [96] Francis A. Duck. *Physical Properties of Tissue: A Comprehensive Reference Book*. Academic Press, 1990.

- [97] Yongli Huang, Edward Hæggeström, Baris Bayram, Xuefeng Zhuang, Arif Sanh Ergun, Ching Hsiang Cheng, and Butrus T. Khuri-Yakub. Comparison of conventional and collapsed region operation of capacitive micromachined ultrasonic transducers. *IEEE Transactions on Ultrasonics, Ferroelectrics, and Frequency Control*, 53(10):1918–1932, 2006.
- [98] B T Khuri-Yakub, A S Ergun, O Oralkan, and G G Yaralioglu. Ultrasonic Transduction. In Yogesh B. Gianchandani, Osamu Tabata, and Hans P. Zappe, editors, *Comprehensive Microsystems*, pages 517–539. Elsevier, 2008.
- [99] Amin Nikoozadeh, Ira O. Wygant, Der Song Lin, Orner Oralkan, Arif Sanli Ergun, Kai Thomenius, Aaron Dentinger, Douglas Wildes, Gina Akopyan, Kalyanam Shivkumar, Aman Mahajan, Douglas N. Stephens, David Sahn, and Pierre T. Khuri-Yakub. Fully integrated CMUT-based forward-looking intracardiac imaging for electrophysiology. In *Proceedings - IEEE Ultrasonics Symposium*, pages 900–903. IEEE, 2007.
- [100] Amin Nikoozadeh, Ira O Wygant, Der Song Lin, Ömer Oralkan, A. Sanli Ergun, Douglas N Stephens, Kai E Thomenius, Aaron M Dentinger, Douglas Wildes, Gina Akopyan, Kalyanam Shivkumar, Aman Mahajan, David J Sahn, and Butrus T Khuri-Yakub. Forward-looking intracardiac ultrasound imaging using a 1-D CMUT array integrated with custom front-end electronics. *IEEE Transactions on Ultrasonics, Ferroelectrics, and Frequency Control*, 55(12):2651–2660, 2008.
- [101] Amin Nikoozadeh, Ömer Oralkan, Mustafa Gencil, Jung Woo Choe, Douglas N. Stephens, Alan De La Rama, Peter Chen, Feng Lin, Aaron Dentinger, Douglas Wildes, Kai Thomenius, Kalyanam Shivkumar, Aman Mahajan, Chi Hyung Seo, Matthew O’Donnell, Uyen Truong, David J. Sahn, and Pierre T. Khuri-Yakub. Forward-looking intracardiac imaging catheters using fully integrated CMUT arrays. *Proceedings - IEEE Ultrasonics Symposium*, 2:770–773, 2010.
- [102] Olaf T Von Ramm and Stephen W Smith. Beam steering with linear arrays. *IEEE Transactions on Biomedical Engineering*, (8):438–452, 1983.
- [103] Muyinatu A. Lediju, Gregg E. Trahey, Brett C. Byram, and Jeremy J. Dahl. Short-lag spatial coherence of backscattered echoes: Imaging characteristics. *IEEE Transactions on Ultrasonics, Ferroelectrics, and Frequency Control*, 58(7):1377–1388, 2011.
- [104] Bjørn A. J. Angelsen. *Ultrasound imaging: waves, signals, and signal processing Vol I*. Emantec, 2000.
- [105] Xuecheng Jin, Ömer Oralkan, F. Levent Degertekin, and Butrus T. Khuri-Yakub. Characterization of one-dimensional capacitive micromachined ultrasonic immersion transducer arrays. *IEEE Transactions on Ultrasonics, Ferroelectrics, and Frequency Control*, 48(3):750–760, 2001.
- [106] Reza Pakdaman Zangabad, Ayhan Bozkurt, Goksenin Yaralioglu, Johan G. Bosch, Gijs van Soest, and Antonius F. W. van der Steen. Mutual Radiation Impedance of Circular CMUT on a Cylinder. In *Proceedings - IEEE Ultrasonics Symposium*, Tours, 2016. IEEE.
- [107] Xuefeng Zhuang, Amin Nikoozadeh, M A Beasley, Goksen G Yaralioglu, Butrus T Khuri-Yakub, and B L Pruitt. Biocompatible coatings for CMUTs in a harsh, aqueous environment. *Journal of Micromechanics and Microengineering*, 17:994–1001, 2007.
- [108] Douglas N. Stephens, Josquin Foiret, Steven Lucero, Katherine W. Ferrara, Kalyanam Shivkumar, and Pierre Khuri-Yakub. 10 MHz Catheter-based Annular Array for Thermal Strain Guided Intramural Cardiac Ablations. *International Ultrasonics Symposium*, 2015.
- [109] Samuel V. Lichtenstein, Anson Cheung, Jian Ye, Christopher R. Thompson, Ronald G. Carere, Sanjeevan Pasupati, and John G. Webb. Transapical transcatheter aortic valve implantation in humans: Initial clinical experience. *Circulation*, 114(6):591–596, 2006.
- [110] Martin Pekař, Alexander F Kolen, Harm Belt, Frank van Heesch, Nenad Mihajlović, Imo E Hoefler, Tamas Szili-Török, Hendrik J Vos, Johan G Bosch, Gijs van Soest, and Antonius F W van der Steen. Preclinical Testing of Frequency-Tunable Capacitive Micromachined Ultrasonic Transducer Probe Prototypes. *Ultrasound in Medicine & Biology*, 43(9):2079–2085, 2017.
- [111] Michael G Earing, Allison K Cabalka, James B Seward, Charles J Bruce, Guy S Reeder, and Donald J Hagler. Intracardiac echocardiographic guidance during transcatheter device closure of atrial septal defect and patent foramen ovale. *Mayo Clinic Proceedings*, 79(1):24–34, 2004.
- [112] Vivek Y Reddy, Gustavo Morales, Humera Ahmed, Petr Neuzil, Srinivas Dukkipati, Steve Kim, Janet Clemens, and Andre D’Avila. Catheter ablation of atrial fibrillation without the

- use of fluoroscopy. *Heart rhythm : the official journal of the Heart Rhythm Society*, 7(11):1644–53, 2010.
- [113] A. M. Leopaldi, R. Vismara, S. van Tuijl, A. Redaelli, F. N. van de Vosse, G. B. Fiore, and M. C M Rutten. A novel passive left heart platform for device testing and research. *Medical Engineering and Physics*, 37(4):361–366, 2015.
- [114] Benjamin Mimoun, Vincent Henneken, and Ronald Dekker. Flex-to-Rigid (F2R): A novel ultra-flexible technology for smart invasive medical instruments. In *Proceedings of the MRS Symposium on Stretchable Electronics and Conformal Biointerfaces, San Francisco, CA, USA*, volume 89, 2010.
- [115] S Weiss, P Vernickel, T Schaeffter, B Gleich, and V Schulz. Towards an RF-safe active catheter for MR-guided interventions. *Medicamundi*, 2005.
- [116] Peter Vernickel, Volkmar Schulz, Steffen Weiss, and Bernhard Gleich. A safe transmission line for MRI. *IEEE Transactions on Biomedical Engineering*, 52(6):1094–1102, 2005.
- [117] M E Ladd, H H Quick, J F Debatin, G K von Schulthess, and G C McKinnon. Resonant heating of intravascular RF coils. In *Proceedings of the 6th annual meeting of ISMRM, Sydney, Australia*, page 473, 1998.
- [118] Stephan Fandrey, Steffen Weiss, and Jörg Müller. Aktive intravaskuläre Magnetresonanz-Sonde auf Basis einer optischen Signalübertragung. *MikroSystemTechnik*, 2009.
- [119] Martin F. Schubert, Qi Dai, Jiuru Xu, Jong Kyu Kim, and E. Fred Schubert. Electroluminescence induced by photoluminescence excitation in GaInN/GaN light-emitting diodes. *Applied Physics Letters*, 95(19):191105, 2009.
- [120] Martinus Bernardus van der Mark and Anna Hendrika van Dusschoten. An optical probe system. Patent US2015335231 (A1), 2015.
- [121] K Vääntinen, J Lammasniemi, K Rakennus, H Asonen, R Jurva, and P Karioja. A Ga_{0.51}In_{0.49}P/GaAs-based photovoltaic converter for two-directional optical power and data transmission. *Progress in Photovoltaics: Research and Applications*, 3(1):57–63, 1995.
- [122] M Röger, G Böttger, M Dreschmann, C Klamouris, Michael Huebner, A W Bett, J Becker, W Freude, and Juerg Leuthold. Optically powered fiber networks. *Optics Express*, 16(26):21821–21834, 2008.
- [123] Delos M Cosgrove and Joseph F Sabik. Minimally invasive approach for aortic valve operations. *The Annals of thoracic surgery*, 62(2):596–597, 1996.
- [124] José L Navia and Delos M Cosgrove. Minimally invasive mitral valve operations. *The Annals of thoracic surgery*, 62(5):1542–1544, 1996.
- [125] Nikolaos Baltayiannis, Chandrinios Michail, George Lazaridis, Dimitrios Anagnostopoulos, Sofia Baka, Ioannis Mpoukovinas, Vasilis Karavasilis, Sofia Lampaki, Antonis Papaiwannou, Anastasia Karavergou, and Others. Minimally invasive procedures. *Annals of Translational Medicine*, 3(4), 2015.
- [126] Ismael Gonzalez, QL Cao, and ZM Hijazi. Role of Intracardiac Echocardiography (ICE) in Transcatheter Occlusion of Atrial Septal Defects. In P. Syamasundar Rao, editor, *Atrial Septal Defects*, pages 99–118. InTech, 2012.
- [127] Kanishka Ratnayaka, Anthony Z. Faranesh, Michael S. Hansen, Annette M. Stine, Majdi Halabi, Israel M. Barbash, William H. Schenke, Victor J. Wright, Laurie P. Grant, Peter Kellman, Ozgur Kocaturk, and Robert J. Lederman. Real-time MRI-guided right heart catheterization in adults using passive catheters. *European Heart Journal*, 34(5):380–388, 2013.
- [128] Reza Razavi, Derek L G Hill, Stephen F. Keevil, Marc E. Miquel, Vivek Muthurangu, Sanjeet Hegde, Kawal Rhode, Michael Barnett, Joop Van Vaals, David J. Hawkes, and Edward Baker. Cardiac catheterisation guided by MRI in children and adults with congenital heart disease. *Lancet*, 362(9399):1877–1882, 2003.
- [129] Fahrettin Levent Degertekin, Coskun Tekes, Lederman Robert Jay, Ozgur Kocaturk, M. Wasequr Rashid, and Maysam Ghovanloo. MRI Compatible 3-D Intracardiac Echography Catheter and System. Patent WO2015048321 (A1), 2015.
- [130] Maurits K. Konings, Lambertus W. Bartels, Henk F M Smits, and Chris J G Bakker. Heating around intravascular guidewires by resonating RF waves. *Journal of Magnetic Resonance Imaging*, 12(1):79–85, 2000.
- [131] Markus Hofstetter, John Howgate, Martin Schmid, Sebastian Schoell, Matthias Sachsenhauser, Denis Adigüzel, Martin Stutzmann, Ian D Sharp, and Stefan Thalhammer. In vitro bio-functionality of gallium nitride sensors for radiation biophysics. *Biochemical and Biophysical Research Communications*, 424(2):348–353, 2012.

- [132] Scott A Jewett, Matthew S Makowski, Benjamin Andrews, Michael J Manfra, and Albena Ivanisevic. Gallium nitride is biocompatible and non-toxic before and after functionalization with peptides. *Acta Biomaterialia*, 8(2):728–733, 2012.
- [133] K L Gammelmark and J A Jensen. Multielement Synthetic Transmit Aperture Imaging Using Temporal Encoding. *IEEE Transactions on Medical Imaging*, 22(4):552–563, 2003.
- [134] Ihor Trots, Andrzej Nowicki, Marcin Lewandowski, and Yuriy Tasinkevych. Synthetic aperture method in ultrasound imaging. In Masayuki Tanabe, editor, *Ultrasound Imaging*, chapter 3, pages 37–56. InTech, Rijeka, 2011.
- [135] Martin B. van der Mark, Anneke van Dusschoten, and Martin Pekař. All-optical power and data transfer in catheters using an efficient LED. In Israel Gannot, editor, *Optical Fibers and Sensors for Medical Diagnostics and Treatment Applications XV*, number 9317, San Francisco, 2015. SPIE Photonics West.
- [136] Jørgen Arendt Jensen. Ultrasound imaging and its modeling. In *Imaging of Complex Media with Acoustic and Seismic Waves*, volume 84, pages 135–136. Springer, 2002.
- [137] Jørgen Arendt Jensen, Svetoslav Ivanov Nikolov, Kim Løkke Gammelmark, and Morten Høgholm Pedersen. Synthetic aperture ultrasound imaging. *Ultrasonics*, 44:e5–15, 2006.
- [138] William C Black, Senior Member, and Douglas N Stephens. CMOS Chip for Invasive Ultrasound Imaging. *IEEE Journal of Solid-State Circuits*, 29(11):1381–1387, 1994.
- [139] Paulo Roriz, Orlando Frazão, António B Lobo-Ribeiro, José L Santos, and José A Simões. Review of fiber-optic pressure sensors for biomedical and biomechanical applications. *Journal of Biomedical Optics*, 18(5):50903, 2013.
- [140] M. Karaman and M. O'Donnell. Synthetic aperture imaging for small scale systems. *IEEE Transactions on Ultrasonics, Ferroelectrics and Frequency Control*, 42(3):429–442, 1995.
- [141] David Bæk, Jørgen Arendt Jensen, and Morten Willatzen. Modeling transducer impulse responses for predicting calibrated pressure pulses with the ultrasound simulation program Field II. *The Journal of the Acoustical Society of America*, 127(5):2825–35, 2010.
- [142] David Bæk, Jørgen Arendt Jensen, and Morten Willatzen. Calibration of field II using a convex ultrasound transducer. In *Physics Procedia*, volume 3, pages 995–1001. Elsevier, 2010.

Summary

Intracardiac catheters are at the heart of this thesis and likewise inside the heart of a patient, who might hopefully benefit from the new technologies we have developed. Catheters represent unique instruments to diagnose and treat a diseased heart. While there are imminent advances in medical innovation, many of the commercially available imaging catheters are outdated. Some of them have been designed more than 20 years and therefore they lack novel sensor technology, multi-functionality, and often require manual assembly process. **Chapter 1** discusses clinical needs and introduces new technological concepts that are needed to progress the functionality and clinical value of the intracardiac catheters along with efficient and simple designs to make the catheters affordable for the patients.

The chapters of this work are grouped into two parts that explore complementary transducer technology and a novel optical fiber-link solution for catheter-based intracardiac imaging. **PART I** focuses on developing a new intracardiac catheter that has an advanced functionality, which provides clinician with high penetration or close-up high resolution ultrasound imaging in a single device. This agile ultrasound visualization is enabled by a capacitive-micromachined ultrasound transducer (CMUT), operated in collapse-mode, of which the operating frequency can be tuned. **Chapter 2** presents a new electro-mechanical model of a collapse-mode CMUT including the frequency tunable transmission. We benchmark our model against two state-of-the-art models and validate it with experimental measurements of a fabricated CMUT prototype. It is concluded that the newly developed model allows fast parameter analysis and is a powerful tool for CMUT pre-design.

The CMUT technology for frequency-tunable ultrasound imaging is explored experimentally in **Chapter 3**. It is shown that the collapse-mode CMUT can operate efficiently at multiple center frequencies when driving pulse and bias voltage are optimized. The usefulness of the frequency tuning is demonstrated by comparing images acquired at multiple frequencies by moving a single-element CMUT across a phantom.

An electronically-scanned, forward-looking, rigid probe prototype based on the CMUT technology is presented in **Chapter 4**. Acoustic performance of the probe is characterized using a pulse-echo technique, in which short-duration ultrasound pulses are transmitted towards a flat target and echo signals are detected and analyzed for amplitude, frequency content, and uniformity. Imaging performance of the probe is evaluated on phantoms in terms of resolution and penetration depth, based on which optimal settings for images acquired in three different modes are identified.

In **Chapter 5**, the rigid probe is advanced to a steerable, forward-looking ICE catheter prototype and both are tested in a heart. Images of an aortic valve are acquired with the rigid probe and the ICE catheter *ex vivo* in a passive heart platform and *in vivo* using a porcine animal model, respectively. The catheter is positioned in an ascending aorta and images of an aortic valve are obtained in the three imaging modes *in vivo*. It is found that the combination of the forward-looking design, frequency-tuning and agile deflectability of the catheter allow for visualizing intracardiac structures of various sizes at different distances relative to the catheter tip, providing both wide overviews and detailed close-ups.

PART II is devoted to a novel optical technology for transmitting signals and transferring power inside catheters. A novel concept of an all-optical fiber link is introduced in **Chapter 6**. A key insight obtained is that a blue light-emitting diode (LED) may be used as a photo-voltaic converter. Used in reverse under illumination with violet light, it converts significant amount of photonic energy to electricity and at the same time it may emit blue light back, which makes it a unique miniature power and communication channel for catheters. A pressure-sensing catheter prototype is built to demonstrate the concept of transmitting signals and delivering power using a single optical fiber and an LED.

The potential of the power and signal fiber link solution is exploited further for ultrasound imaging in **Chapter 7**. A bench-top demonstrator scalable to catheter dimensions is built, in which electrical wires for ultrasound-sensor signal and power transfer are replaced by optical fibers. Power to the ultrasound transducer is delivered optically and converted to electricity by two LEDs. The ultrasound-sensor signal is transmitted via a miniature laser that is commonly used in Ethernet communication. Images obtained with the optical fiber link are compared to those obtained with conventional electrical wires. Because no noticeable difference in image quality is found, it is concluded that the optical solution is suitable for intracardiac echocardiography. This new technology allows for slender devices with high level of integration and simple assembly, which may make these smart disposable devices more affordable.

Once matured and integrated in a single device, the innovative frequency-tunability and all-optical fiber link concepts presented in this thesis may become the **ABCs** of future intracardiac ultrasound imaging.

Samenvatting

Intracardiale katheters zitten zich in het hart van dit proefschrift en evenzo in het hart van de patiënt, die hopelijk voordeel kan ondervinden van de nieuwe technologieën die we ontwikkeld hebben. Katheters zijn unieke instrumenten voor zowel het diagnosticeren als het genezen van een hartziekte. Door de voortdurende vorderingen in medische innovatie zijn een aantal commerciële beeldkatheters inmiddels verouderd. Het ontwerp van sommige van deze katheters is meer dan 20 jaar oud waardoor ze de modernste sensor technologie ontberen. Ze hebben gebrek aan multifunctionaliteit en vaak vereist hun de productie handmatige montage.

Hoofdstuk 1 verteld over klinische behoeften en introduceert nieuwe technologische denkbeelden, die de functionaliteit en klinische waarde van de huidige intracardiale katheters moeten gaan verbeteren. De katheters moeten zó ontworpen worden dat ze efficiënt, eenvoudig, en daardoor ook betaalbaar zijn.

De hoofdstukken van dit proefschrift zijn in twee groepen georganiseerd, in de eerste wordt onderzoek gedaan aan uitgebreidende technologie voor ultrageluidbronnen en in de tweede wordt een vernieuwende optische vezellink-oplossing voor beeldvorming met intracardiale katheters gepresenteerd en onderzocht. DEEL I richt zich op de ontwikkeling van een nieuwe intracardiale katheter, die geavanceerde functionaliteit heeft, waarmee de arts, kijkend naar een ultrageluidbeeld, kan kiezen tussen hoge indringdiepte enerzijds of detailopname met hoge resolutie anderzijds. Deze behoudige ultrageluidvisualisatie wordt mogelijk gemaakt door het in frequentie afstemmen van een capacitieve-microgevormde ultrageluidomzetter (CMUT) die in een collapse mode werkzaam is.

Hoofdstuk 2 introduceert een nieuw electro-mechanisch model van een collapse-mode CMUT inclusief frequentieafstemming. We vergelijken ons model met twee veel gebruikte (state-of-the-art) modellen en beoordelen de validiteit van ons model met experimenten, namelijk door optische en akoestische metingen van een gefabriceerde CMUT prototype. Hieruit komen we tot de conclusie dat het nieuwe model een snelle parameteranalyse verschaft, waardoor het een krachtig gereedschap voor verder CMUT pre-design lijkt te zijn.

Het toepassen van frequentie verstembbaarheid van de CMUT voor het maken van ultrageluidafbeeldingen wordt in **Hoofdstuk 3** experimenteel onderzocht. Er wordt laten zien dat de collapse-mode CMUT efficiënt kan werken op meerdere frequenties, mits de excitatie puls en bias spanning

geoptimaliseerd zijn. De nuttigheid van het verstemmen van de frequentie is gedemonstreerd door het vergelijken van beelden die op meerdere frequenties met een enkelvoudig CMUT-element opgenomen werden, terwijl deze over een fantoom bewoog.

In **Hoofdstuk 4** wordt een elektronisch-gescande, vooruitkijkende, onbuigzame sonde, gebaseerd op de CMUT technologie gepresenteerd. De akoestische prestatie van deze sonde is gekarakteriseerd met een pulse-echo techniek, waarin kortdurende pulsen worden gestuurd en van een platte reflector worden terug gespiegeld en vervolgens ontvangen en gekarakteriseerd op amplitude, frequentie en uniformiteit. De afbeeldingskwaliteit van de sonde is daarna op fantomen beoordeeld op resolutie en indringdiepte, waardoor de optimale instellingen voor drie verschillende afbeeldingmodes konden worden vastgesteld.

In **Hoofdstuk 5**, wordt de onbuigzame sonde verbeterd tot een buigzame, vooruitkijkende intracardiale katheterprototype en beiden worden in een hart getoetst. Beelden van een aortaklep zijn zowel met de onbuigzame als de buigzame katheter in respectievelijk een *ex vivo* passief hartplatform en een *in vivo* varkensdiermodel gemaakt. Daarbij werd de katheter in de opgaande aorta geplaatst en zijn er beelden gemaakt van de aortaklep in de drie afbeeldingmodes. Hieruit is het duidelijk geworden dat de combinatie van het vooruitziende ontwerp, het frequentieverstemmen en de flexibele schacht van de katheter het mogelijk maken om intracardiale structuren van gevarieerde afmetingen op verschillende afstanden relatief tot de kathetertip te kunnen visualiseren. Daardoor voorziet zo'n katheter de dokter van een overzichtelijk ultrageluidbeeld maar, naar keuze, ook van detailopname met hoge resolutie.

DEEL II is gewijd aan nieuwe optische technologie voor het overbrengen van signalen en data in katheters. Een vernieuwend idee voor een geheel optische vezellink wordt in **Hoofdstuk 6** geïntroduceerd. Het sleutelinzicht is dat een blauw licht uitstralende diode (LED) ook als een fotonvoltaïsche omzetter gebruikt kan worden. Onder verlichting van violet licht is de LED in staat een groot deel van de lichtenergie om te zetten naar elektriciteit en kan daarbij ook blauw licht terug uitzenden. Zo'n functionaliteit maakt een LED een uniek miniatuur element voor simultane vermogensoverdracht en communicatie in katheters. Een drukgevoelige katheterprototype is gebouwd om dit idee van signaaluitzending en vermogenlevering met een enkele optische fiber, gelijmd aan een LED, te demonstreren.

Het potentieel van de optischevezel link oplossing voor de overdracht vermogen en signaal is verder onderzocht in **Hoofdstuk 7** bij gebruik voor ultrageluidafbeelding. Een "bench-top" opstelling, die tot de afmeting van een katheter verkleind kan worden, is gebruikt om aan te tonen dat elektrische draden voor transmissie van de ultrageluid signalen vervangen kunnen worden door optische vezels. De ultrageluidomzetter wordt met elektriciteit gevoed,

die verkregen is met behulp van twee LEDs door middel van conversie uit fotonen. De in elektrischiteit omgezette ultrageluidsignalen worden door een miniatuur laser, die gewoonlijk in Ethernet communicatie wordt gebruikt, naar de buitenwereld gestuurd. De beelden die via de optische vezellink zijn ontvangen, zijn vergeleken met beelden, die over gewone elektrische draden zijn ontvangen. Omdat er geen opvallende verschillen bij deze vergelijking zijn opgemerkt, kan de conclusie worden getrokken dat de optische oplossing geschikt is voor intracardiale echocardiografie. Deze nieuwe technologie voorziet slankere katheters met een hoger niveau van integratie en een meer eenvoudige assemblage, waardoor deze slimme wegwerlinstrumenten binnen het economische bereik van patiënten worden gebracht.

Zodra de innovatie van het frequentieverstemmen en de volle optische vezellink technologie, die allebei in dit proefschrift zijn gepresenteerd, zullen zijn gerijpt, bestaat wellicht de mogelijkheid dat ze het **ABC** van de toekomstige intracardiale ultrageluidafbeelding zullen vormen.

Publications

Journal Papers

Martin Pekař, Nenad Mihajlović, Gijs van Soest, and Nico de Jong, Frequency Tuning of Collapse-Mode Capacitive Micromachined Ultrasonic Transducer, *Ultrasonics*, 74, pp. 144-152 (2017).

Martin Pekař, Jeannet van Rens, and Martin B. van der Mark, Electrifying Catheters with Light, *Optics Express* (Spotlight) 25, no. 8, pp. 8534 – 8549 (2017).

Martin Pekař, Alexander F. Kolen, Harm Belt, Frank van Heesch, Nenad Mihajlović, Imo E. Hoefler, Tamas Szili-Török, Hendrik J. Vos, Johan G. Bosch, Gijs van Soest, and Antonius F. W. van der Steen, Preclinical Testing of Frequency-Tunable Capacitive Micromachined Ultrasonic Transducer Probe Prototypes, *Ultrasound in Medicine & Biology*, 43, no. 9, pp. 2079 – 2085 (2017).

Martin Pekař, Nenad Mihajlović, Harm Belt, Alexander F. Kolen, Jeannet van Rens, Frank Budzelaar, Bas Jacobs, Johan G. Bosch, Hendrik J. Vos, Debbie Rem-Bronneberg, Gijs van Soest, and Antonius F. W. van der Steen, Imaging Performance of Frequency-Tunable Collapse-Mode Capacitive Micromachined Ultrasonic Transducer Array, *Ultrasonics* **in review**.

Martin Pekař, Stephan H. M. van Nispen, Rob H. B. Fey, Sergei Shulepov, Nenad Mihajlović, and Henk Nijmeijer, A Fluid-Coupled Transmitting CMUT Operated in Collapse Mode: Semi-Analytic Modelling and Experiments, *Sensors and Actuators A: Physical* **in review**.

Patents

Martin Pekař and Martin B. van der Mark, Ultrasound system and method, *World Intellectual Property Organization*, WO2016083273 (A1) (2016).

Martin Pekař, An ultrasound system with frequency tunable collapsed mode CMUT, *World Intellectual Property Organization*, Application number 16199348.0 (2016).

Martin Pekař and Wendy Dittmer, An ultrasound system with a tissue type analyzer, *World Intellectual Property Organization*, Application number 16195916.8 (2016).

Conference Proceedings

Martin Pekař, Nenad Mihajlović, Harm Belt, Alexander F. Kolen, Bas Jacobs, Johan G. Bosch, Hendrik Vos, Gijs van Soest, Nico de Jong, and Debbie Rem-Bronneberg, Frequency-Agility of Collapse-Mode 1-D CMUT Array, *Proceedings of IEEE International Ultrasonics Symposium (IUS)*, 978-1-4673-9897-8 (2016).

Martin B. van der Mark, Anneke van Dusschoten, and **Martin Pekař**, All-optical power and data transfer in catheters using an efficient LED, *Proceedings of SPIE Photonics West, BiOS*, 9317-13 (2015).

Oral (O) and Poster (P) Presentations

Martin Pekař, Jeannet van Rens, and Martin B. van der Mark, Ultrasound imaging using all-optical power and signal transfer in catheters (O), *SPIE Photonics West, BiOS*, 10054-31 (2017).

Martin Pekař, Martin B. van der Mark, and Jeannet van Rens, Optical Power and Data for Catheter-Based Imaging (P), *Optics in Cardiology* (2017).

Martin Pekař, Alexander F. Kolen, Harm Belt, Nenad Mihajlović, Frank Budzelaar, Bas Jacobs, Jeannet van Rens, Johan G. Bosch, Hendrik Vos, Antonius F. W. van der Steen, Debbie Rem-Bronneberg, Frank van Heesch, Stephan H. M. van Nispen, and Sergei Shulepov, Innovative Technology for Intracardiac Imaging Catheters (O), *Autumn Meeting of Dutch Society of Medical Ultrasound* (2016).

Martin Pekař, Nenad Mihajlović, Harm Belt, Alexander F. Kolen, Bas Jacobs, Johan G. Bosch, Hendrik Vos, Gijs van Soest, Nico de Jong, and Debbie Rem-Bronneberg, Ultrasound Imaging with Frequency-Agile CMUT (O), *10th International Conference on Ultrasonic Biomedical Microscanning* (2016).

Martin Pekař, Wendy Dittmer, and Nenad Mihajlović, Multi-frequency imaging with collapse-mode CMUT (O), *IEEE International Ultrasonics Symposium (IUS)* (2015).

Martin Pekař, Wendy Dittmer, and Nenad Mihajlović, Multi-frequency imaging with CMUT (O), *Artimino conference* (2015).

Martin Pekař, Anneke van Dusschoten, and Martin B. van der Mark, Integrated Pressure Sensor Powered and Read-out via a Single Optical Fiber (O), *Design of Medical Devices Conference*, 37 (2014).

Acknowledgements – Dankwoord – Poděkování

Here we are, I was truly looking forward to writing these final words. The last four years were undoubtedly the most intensive period in my life. New country, language, colleges, friends, marathon, triathlon, wedding, child, and yes, of course, the little push in human knowledge called PhD. None and especially the last one would ever be possible without the help of bunch of great people, to whom I devote the following lines. With you *ging het van een leien dakje*. As long as you are around, I can keep smiling at this world.

Martin, het was mij een eer om van zo'n echte en wilde onderzoeker als jij te kunnen leren en samen op de *Electrifying catheters* te kunnen samenwerken. Je was eerlijk tegen mijn toen je tijdens ons interview zei: „Whatever we agree on now, will change later anyhow.“ Je zorgde voor mijn inburgering in Nederland en sprak uitsluitend Nederlands met mij vanaf de eerste werkdag. Je hebt me geleerd hoe ik mijn eerste octrooi moet schrijven en hoe krachtig het is om dingen echt te maken. Dank je wel daarvoor.

Gijs, bedankt voor jouw academische begeleiding en jouw pogingen om me solide en duidelijke publicaties te kunnen leren schrijven. Ik heb daarover veel van je geleerd en ik denk dat het je gelukt is. Hopelijk, „kan je me niet meer horen als je mijn wetenschappelijke paper leest“.

Nenad, you are for sure the most frequent co-author on my papers. It was a real pleasure to work with you. I appreciate your knowledge and acquaintance with building full-chain ultrasound imaging systems, your eye for detail and the never ending shower of questions that you used to check on the validity of my experiments or models. I still remember the day we obtained the first ultrasound image with the earliest CMUT prototype. The image still hangs on the wall in our lab. *хва́ла ти нуно за ва́шу помо́ћ*.

Alex, zonder jou zou ik nooit naar Philips zijn gekomen. Dank je wel voor jouw begeleiding tijdens mijn afstudeerproject en daarna voor jouw onschatbare hulp met de laatste en de aller beste preklinische publicatie. Hoewel ik altijd alleen jouw rug kon zien, was het spannend om met jou aan de loopevenementen deel te nemen.

Harm, jouw elegante manier om software te beheersen is uniek en bijzonder doeltreffend. Dank je wel voor al die algoritmen die je gemaakt hebt en die ik heb kunnen gebruiken. Zonder jouw hulp zou dit proefschrift nooit in vier jaar klaar zijn.

Jeannet, ik ken geen andere persoon die zo'n breed verstand van elektronica en akoestiek heeft. Jouw vragen zijn altijd treffend, hoewel ze vaak nieuwe experimenten vereisen. Jouw hulp met de interpretatie van de meetresultaten en het ontcijferen van een experimentele opstelling waren onontbeerlijk voor dit proefschrift.

Frank B, jouw praktische kennis van electronica heeft veel ruis van dit proefschrift verwijderd en verbindingen naar het ultrageluidstelsel mogelijk gemaakt. Hartstikke bedankt daarvoor!

Anneke, bedankt voor jouw hulp met de optische link en ook voor het aantal vragen die ik je niet kon beantwoorden, maar die me naar de juiste richting hebben gewezen.

Peter D, ik zie je als een vader van de CMUT die me gedurende de hele doctoraatperiode heeft begeleid. Dank je wel voor het ontwerpen van zo'n geweldige omzetter.

Alfons, zonder jou zou ik geen acoustische golven hebben kunnen meten. Dank je wel voor al die CMUTs die je gemaakt hebt en voor de opwindende discussies over de MEMS-fabricatie.

Debbie en Wendy, jullie zijn de meest roofdierachtige projectleiders die ik ken. Het was me plezier om voor jullie projecten te werken en de kunst van planning en risico vermijndering te kunnen leren van jullie.

Prof. van der Steen en René, dank jullie allebei voor het opstellen van de samenwerking en voor „having me in your teams“.

I gratefully acknowledge the funding provided by the European Union („OILTEBIA“, grant no. 317526) and the project coordination by prof. Lamela and his team.

Dear OILTEBIA fellows, thank you for the time we spent together and for your contributions to the European research.

Nico, super bedankt voor jouw hulp met mijn eerste publicatie. Het was een hele bevalling.

Rik en Hans, ik ben dankbaar voor jullie hulp in het laatste en ook het meest intensieve jaar van mijn doctoraat.

Imo en dr. Szili-Török, dank jullie wel voor de hulp met de pre-klinische studie.

Stephan, Rob en prof. Nijmeijer, het werken met jullie was een voorbeeld

van een vlotte en professionele samenwerking. Hartstikke bedankt voor jullie bijdragen aan het CMUT model.

Chris en Marco, jullie hulp met de hydrofoon opstelling en de digitale holografische microscoop vond ik heel nuttig. Dank jullie wel.

Bas, Wim en Henk, jullie hebben gouden handen. Dank jullie wel voor de mechanische ontwerpen die jullie voor me hebben gemaakt.

Jos en Jim, ik ben dankbaar voor jullie hulp met elektronica. Het is fijn om jullie in de buurt te hebben.

John, Walter en Henk, dank jullie wel voor de hulp met LabVIEW software.

Veerle en Jan vanuit de bibliotheek, dank jullie allebei voor de ondersteuning en hulp met het zoeken van publicaties en schaarse ultrageluidtekstboeken.

Ferry, Harold, Mischa en Frank vH, mijn beste kantoorgenoten. Het was prettig om met jullie het kantoor te delen. Jullie waren altijd zo behulpzaam. Dank Ferry voor het fornuis om te kunnen koken, Harold voor de gladde fietsbanden voor mijn mountainbike om de triatlon te kunnen halen, Mischa voor zijn hulp met de moeilijke wetenschappelijke vragen. Frank vH voor de leuke mountainbike-route tips en hulp met de omslag van dit proefschrift.

Jovana, Deep, Sophines, Reza, and Min, you are my dearest friends from Rotterdam. I'm grateful that I've have met you and that we had so much fun and beer together at various places of the world. Deep, special thanks to you for your help in searching for the lost iPhone and counting the tattoos...

Shivani, Zoi, Ronald, Angel and other PPCians, thank you for making my PhD at Philips more enjoyable. It was fun to organize the PhD events together! You are the reason I would wish for PhD to take longer.

Christian, thank you for all the practical tips, baby stuff and enthusiasm for the Czech beer. I did enjoy the precious evenings we spent together above the golden fluid.

Wilma, zonder jou zou ik al lang in het administratieve oerwoud verloren zijn. Super bedankt voor jouw permanente spoedhulp, alle kindertips, cadeautjes en de gezelligheid waarvoor je in onze groep zorgt.

Sharon, dank je wel voor jouw hulp met de promotieadministratie en het invullen van allerei soort formulieren.

Michel, je bent de goede vent (en baas) die ik altijd kan vertrouwen. Zonder jou zou mijn toekomstige carrière bij Philips onzeker zijn. Hartelijk bedankt voor jouw ondersteuning, vertrouwen en zorgen voor mijn ontwikkeling.

Vážená Jano, vždy jsem se moc těšil na Vaše lekce nizozemštiny a ve snaze Vás nezklamat jsem doháněl úkoly, byť již bylo za pět minut dvanáct (o půlnoci). Jsem Vám vděčný za svoje znalosti nizozemského jazyka, nad jejichž dobrou úrovní se ne jeden Holanďan podiví. Díky Vám se v Nizozemí cítím téměř jako doma.

Drazí rodiče, děkuji vám za dobré vychování a volnost, kterou jste mně dali jakožto i za podporu v jakýchkoliv rozhodnutích. Mamínko, děkuji Ti za Tvé rady do života a nekončící nadšení ze svých synů. Brácho, díky za to, že jsi to doma během posledních pár let všechno obstaral. Také bych chtěl poděkovat celé své rodině a kamarádům za jejich zájem a milé návštěvy v Nizozemí, kterými mě vždy potěší. Rovněž děkuji Iren a Hynkovi za jejich rodinnou výpomoc v Eindhovenu.

Milá Irenko, jsi krásná, šikovná, sympatická a vůbec nejbáječnější maminka našeho syna Jáchymka. Mockrát Ti děkuji za Tvoji bezmeznou podporu, porozumění a lásku.

Jáchymku, až dospěješ a budeš číst tyto řádky v době, kdy papír bude dobrý tak akorát na zátok, věřím, že budeš na svého tátu pyšný stejně tak, jako je on teď na Tebe. Ty jsi náš šikovný a roztomilý klučik, pro kterého s maminkou žijeme!

Martin Pekař
Eindhoven, 2017

Curriculum Vitae



Martin Pekař was born on 20th March, 1987 in Prague, the Czech Republic. He was raised and educated in the Krkonoše mountains up to the North of Prague. He received his Bachelor and Master degree in Biomedical and Clinical technology from the Czech Technical University in Prague, the Czech Republic, in 2009 and 2011, respectively. He obtained a second Master degree in Biomedical Engineering from the same university in 2013. Martin has been awarded several scholarships that allowed him to follow two years of his university studies abroad, such as in Finland, the USA, and the Netherlands. From 2013 till 2017, he was Marie Curie Fellow at Philips Research in Eindhoven, the Netherlands and pursued in parallel towards the PhD degree from Erasmus Medical Center, Thorax Center Department of Biomedical Engineering in Rotterdam, the Netherlands. Apart from the Czech mother tongue can Martin speak fluent English and Dutch.

Currently, he is working as Scientist at Philips Research in Eindhoven. His research interests include capacitive micromachined ultrasonic transducers, ultrasound imaging, optical fiber-link solution and other innovations for minimally-invasive medical devices.

PhD Portfolio

International Conferences	Date	ECTS
Optics in Cardiology (O), Rotterdam, the Netherlands	2017	1.2
SPIE Photonics West BiOS (O), San Francisco, USA	2017	3.4
IEEE International Ultrasonics Symposium (P), Tours,	2016	1.9
International Conference on Ultrasonic Biomedical Microscanning (O), Kralendijk, Bonaire, the Netherlands	2016	3.1
IEEE International Ultrasonics Symposium (O), Taipei, Taiwan	2015	3.1
Artimino conference, Helsinborg (O), Sweden	2015	3.1
SPIE Photonics West BiOS (O), San Francisco, USA	2015	0.6
Design of Medical Devices (O), Delft, the Netherlands	2014	1.9

Courses	Date	ECTS
Effective Technical Presentations (on-line), San Francisco, USA	2017	0.2
Principles and Applications of Optical Coherence Tomography, SPIE Photonics West BiOS, San Francisco, USA	2017	0.2
Light-Emitting Diodes, SPIE Photonics West BiOS, San Francisco, USA	2017	0.2
Acoustical Imaging, IEEE IUS, Taipei, Taiwan	2015	0.2
Elasticity Imaging, IEEE IUS, Taipei, Taiwan	2015	0.2
Advanced Ultrasound Imaging, Danish Technical University, Copenhagen, Denmark	2015	2.5
Intellectual Property & Standards, Philips, Eindhoven, the Netherlands	2015	0.3
Micromachined Ultrasonics Transducers, Danish Technical University, Copenhagen, Denmark	2014	3.5
Verasonics course, Philips, Eindhoven, the Netherlands	2014	0.6
Medical Ultrasound Transducers, IEEE IUS, Prague, the Czech Republic	2013	0.2

Continued on next page

(O) and (P) stand for oral and poster presentation, respectively.

Continued from previous page

Courses	Date	ECTS
Photoacoustics, IEEE IUS, Prague, the Czech Republic	2013	0.2
Dutch language course, Institute for Dutch Language and Culture, Prague, the Czech Republic	2013 – 2017	6.0

Research Symposia	Date	ECTS
3 rd Industrial Involvement Workshop (P), OILTEBIA, Eindhoven, the Netherlands	2016	2.6
3 rd Summer School, OILTEBIA (P), Lyon, France	2016	2.1
3 rd Laboratory Training Platform, OILTEBIA, Munich, Germany	2016	1.0
1 st Industrial Involvement Workshop, OILTEBIA (P), Tours, France	2015	1.6
2 nd Laboratory Training Platform, OILTEBIA, Milan, Italy	2014	1.5
1 st Summer School, Laboratory Training Platform, and Complementary Course Training, OILTEBIA (O,P), Madrid, Spain	2014	3.1
Dutch Society of Medical Ultrasound – Autumn meeting (O), Nijmegen, the Netherlands	2016	0.2
COEUR Cardiovascular Imaging and Diagnostics, Erasmus MC, Rotterdam, the Netherlands	2015	1.0
Philips PhD Reflect Symposium, Eindhoven, the Netherlands	2016	0.3
Philips PhD Reflect Symposium, Eindhoven, the Netherlands	2014	0.3
Philips PhD Reflect Symposium, Eindhoven, the Netherlands	2013	0.3

Supervising activities	Date	ECTS
Supervising master student from Eindhoven Technical University (11 months)	2016	4.0
Supervising bachelor student visiting from Massachusetts Institute of Technology (3 months)	2013	1.0

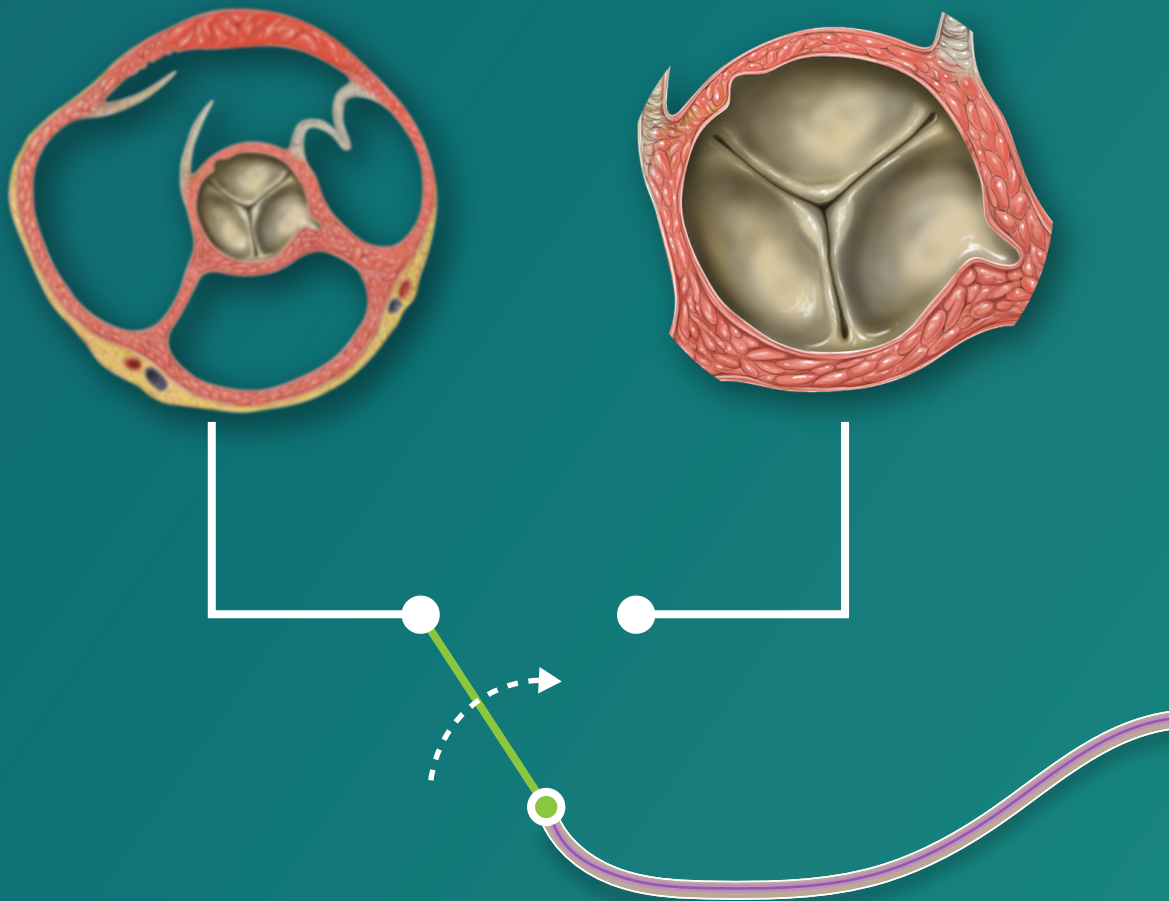
Total ECTS: 51.6

(O) and (P) stand for oral and poster presentation, respectively.

Innovative concepts presented in this thesis might be the **ABCs** of future intracardiac ultrasound imaging.

Martin Pekař

Philips Research in Eindhoven, the Netherlands, 2017



Cover image illustrates a future intracardiac echo catheter placed in the heart. Agile frequency operation of the catheter offers the versatility of choice between high penetration or high resolution imaging of the heart valve. Bright violet light electrifies the ultrasound imaging sensor at the tip of the catheter.

